A Navigator–Based Rigid Body Motion Correction for Magnetic Resonance Imaging

Von der Fakultät für Mathematik, Informatik und Naturwissenschaften
der RWTH Aachen University zur Erlangung des akademischen Grades
eines Doktors der Naturwissenschaften genehmigte Dissertation

vorgelegt von

Diplom-Physiker
Marcus Görge Ullisch
aus Højer, Dänemark

Berichter:
Universitätsprofessor Dr. Nadim Jon Shah
Universitätsprofessor Dr. Achim Stahl

Tag der mündlichen Prüfung: 24. Januar 2012

Diese Dissertation ist auf den Internetseiten der Hochschulbibliothek
online verfügbar.

To my parents

CONTENTS

List of Figures vii

List of Tables xiii

Zusammenfassung xv

Abstract xvii

Acknowledgements xix

1 Introduction 1

1.1 Motion Artefacts in MRI 1

1.2 Existing Methods for Motion Correction 1

1.2.1 Aim of this Work 6

2 Basics of Magnetic Resonance Imaging 9

2.1 The Origin of the MR Signal 9

2.1.1 Spin Polarisation 9

2.1.2 Precession 10

2.1.3 Spin Excitation 11

2.1.4 Magnetisation Relaxation 13

2.1.5 Signal Equation 14

2.1.6 T_2^* Decay 15

2.2 Spatial Encoding 17

2.2.1 Slice Selection 17

2.2.2 Frequency Encoding 19

2.2.3 Phase Encoding 21

2.3 Sequences 22

2.3.1 Gradient Echo 22

2.3.2 Spin Echo 25

2.3.3 MP–RAGE — An Advanced Sequence for Neuro–imaging 25

2.4 MRI Hardware 27

2.4.1 The MRI Scanner — an Overview 28

2.4.2 The Magnet 30

2.4.3 The Gradient System 30

2.4.4 The Radio Frequency System 32

2.5 Physiological Limits to the MRI Experiment 33

2.5.1 Specific Absorption Rate 33

2.5.2 Nerve Stimulation 34

3 Theory of Navigator–Based Motion Correction 35

3.1 k–Space 35

3.1.1 Analytical Description 36

3.1.2 Pictorial Description 37

3.2 Effect of Rigid Body Motion on k–space 39

3.2.1 Translations in k–Space 39

3.2.2 Rotations in k-Space 39

3.3 Currently Available Navigated Motion Correction Techniques for MRI 40
3.3.1 Line Navigators for Breath–Motion Triggering 40
3.3.2 Three–Dimensional Navigators for Rigid Body Motion Correction 42
3.4 The Lissajous Navigator 46
3.4.1 Conventional 2D Lissajous Figures 47
3.4.2 Lissajous Trajectory on the Sphere 47

4 Data Processing Algorithms 53
4.1 Rotation Estimation 53
4.1.1 Gridding on the Spherical Surface 55
4.2 T_2^* Correction Algorithm 55
4.3 Translation Estimation 60

5 Quantitative Motion Estimation through Simulations 63
5.1 *J*ülich *E*xtensible *MRI S*imulator — JEMRIS 64
5.2 Comparison of the Spherical Navigator and the Lissajous Navigator 64
5.2.1 Simulations & Analysis 65
5.2.2 Accuracy of Rotation Estimation 66
5.2.3 Accuracy of Translation Estimation 66
5.3 Influence of Susceptibility, Signal Decay and Chemical Shift on the Rotation Estimation 69
5.4 Influence of Noise on the Accuracy of Rotation Estimation 73

5.5 *A*dvanced *Li*ssajous Navi*ga*tor with T_2^* Co*r*rection (ALIGAT2R) . . . 75
5.5.1 Simulations & Analysis . . . 78
5.5.2 Results . . . 79
5.5.3 Discussion . . . 88

6 Measurement and Optimisation of the Fidelity of the Navigator Trajectory 91

6.1 Trajectory Measurement . . . 91
6.1.1 Method . . . 92
6.1.2 Measurements . . . 93
6.1.3 Results . . . 93
6.2 Trajectory Correction . . . 95
6.2.1 Method . . . 96
6.2.2 Results . . . 101

7 Experimental Comparison of the Lissajous Navigator and the Spherical Navigator 109

7.1 Navigator Sequence . . . 109
7.2 Virtual Rotation . . . 110
7.3 Two–Chamber Phantom . . . 111
7.4 Sequence and Navigator Parameters . . . 114
7.5 Measurements . . . 115
7.5.1 Radius Optimisation Measurements . . . 115
7.5.2 Trajectory Optimisation . . . 115
7.5.3 Navigator Comparison Measurements . . . 115
7.6 Analysis . . . 116

7.7 Results 116
7.8 Discussion 122
7.9 Conclusions 127

8 Summary and Prospects 129
8.1 Summary 129
8.2 Prospects 131

Index 134

References 139

List of Figures

1.1 Structural MR image without motion 2
1.2 Structural MR image with motion 3

2.1 Precession of spins in the static field 11
2.2 Net magnetisation during RF excitation 12
2.3 Free induction decay (FID) 16
2.4 Slice selection 18
2.5 Spatial localisation through frequency encoding . . . 20
2.6 Gradient echo sequence diagram 24
2.7 Spin echo sequence diagram 26
2.8 3D MP–RAGE sequence diagram 27
2.9 Simplified schematic of MRI scanner hardware 29
2.10 Schematic of the gradient coils 31

3.1 Pictorial description of k–space 38
3.2 Influence of rotation on the k–space magnitude . . . 41
3.3 Spherical navigator k–space trajectory 43
3.4 Spherical navigator gradients and slew rates 45
3.5 Conventional Lissajous figure 48
3.6 Lissajous navigator k-space trajectory 49

3.7 Gradient comparison of Lissajous navigator and spherical navigator 51
3.8 Slew rate comparison of Lissajous navigator and spherical navigator 52

4.1 Rotation estimation algorithm schematic 54
4.2 Influence of T_2^* decay on the navigator 56
4.3 Crossing point definition for T_2^*–Correction 58

5.1 Absolute error of rotation estimates on axis of rotation 67
5.2 Off–rotation axis errors, for rotations around x 68
5.3 Off–rotation axis errors, for rotations around y 68
5.4 Off–rotation axis errors, for rotations around z 69
5.5 Accuracy of translation estimation for the spherical and Lissajous navigators at a k–space radius of $0.03\frac{1}{mm}$ 70
5.6 Accuracy of translation estimation for the spherical and Lissajous navigators at a k–space radius of $0.07\frac{1}{mm}$ 71
5.7 Absolute error of the rotation estimates on the axis of rotation with noise. 76
5.8 Off–rotation axis errors, for rotations around x with noise. 77
5.9 Off–rotation axis errors, for rotations around y with noise. 77
5.10 Off–rotation axis errors, for rotations around z with noise 78
5.11 Ideal navigator without T_2^*–decay and chemical shift. 80
5.12 Uncorrected navigator with relaxation artefacts. . . . 81
5.13 T_2^*–decay corrected navigator. 82

5.14 Difference between reference navigator and rotated navigator interpolated back to reference position, uncorrected. 83
5.15 Difference between reference navigator and rotated navigator interpolated back to reference position, decay corrected. 84
5.16 Absolute error of rotation estimation with T_2^*–correction on axis of rotation (decay, chemical shift). 84
5.17 Absolute error of rotation estimation with T_2^*–correction off-rotation axes for rotations around x (decay, chemical shift). 85
5.18 Absolute error of rotation estimation with T_2^*–correction off-rotation axes for rotations around y (decay, chemical shift). 85
5.19 Absolute error of rotation estimation with T_2^*–correction off-rotation axes for rotations around z (decay, chemical shift). 86
5.20 Absolute error of rotation estimation with T_2^*–correction on axis of rotation (with susceptibility). 86
5.21 Absolute error of rotation estimation with T_2^*–correction off-rotation axes for rotations around x (with susceptibility). 87
5.22 Absolute error of rotation estimation with T_2^*–correction off-rotation axes for rotations around y (with susceptibility). 87

5.23 Absolute error of rotation estimation with T_2^*–correction off-rotation axes for rotations around z (with susceptibility). 88

6.1 Ideal and measured navigator k–space trajectory . . . 94
6.2 Measured k–space trajectory radius 95
6.3 System manufacturer gradient correction schemes . . 97
6.4 Predistorted navigator k–space trajectory from amplifier output 98
6.5 Iterative gradient correction algorithm 100
6.6 Measured gradient delays by trajectory measurement 102
6.7 Measured gradient delays by echo shift. 103
6.8 Uncorrected and corrected navigator k–space trajectory 105
6.9 Ideal, uncorrected, and corrected navigator k–space trajectory, zoomed view 106
6.10 Navigator k–space radius corrected 106
6.11 Navigator k–space radius corrected, zoomed view . . 107

7.1 Navigator–FLASH sequence diagram 110
7.2 Virtual rotation parameters 112
7.3 Photograph of the two–chamber phantom 113
7.4 MRI FLASH image of the two–chamber phantom . . 114
7.5 Spherical navigator magnitude signal 117
7.6 Lissajous navigator magnitude signal 118
7.7 Plot of Lissajous navigator magnitude signal (optimised trajectory) 119
7.8 Rotation estimation results 120
7.9 Absolute error of rotation estimates on rotation–axis 121

7.10 Off–rotation axis errors, for rotations around x 122

7.11 Off–rotation axis errors, for rotations around y 123

7.12 Off–rotation axis errors, for rotations around z 123

List of Tables

5.1 Influence of susceptibility, decay and chemical shift (fat), on the accuracy of the rotation estimation of the navigator. 74
5.2 Influence of signal–to–noise ratio on the rotation estimation. 75

ZUSAMMENFASSUNG

Im Rahmen der vorliegenden Arbeit wurde eine neuartige dreidimensionale Navigator k-Raum Trajektorie zur Bewegungsdetektion starrer Körper für die Magnetresonanztomographie (MRT) entwickelt: der *Lissajousnavigator*. Weiterhin wurde ein quantitativer Vergleich der Genauigkeit des Lissajousnavigators und des sphärischen Navigators [1] durchgeführt.

Bedingt durch die Slewrate Limitierung der MRT-Hardware kann der sphärische Navigator nicht die gesamte Kugeloberfläche abtasten. Durch die Nutzung einer auf die Kugeloberfläche projizierten, zweidimensionalen Lissajousfigur kann der Lissajousnavigator diese Limitierung überwinden. Die lückenlose Abtastung der Kugeloberfläche führt zu einer höheren Genauigkeit der Rotationsmessung und zu einer höheren Isotropie des systematischen Fehlers der Rotationsmessungen. Mit beiden Navigatortrajektorien wurden Simulationen und Messungen an Phantomen durchgeführt. Unter identischen Messbedingungen und mit identischer Auswertung ist der mittlere absolute Fehler der Rotationsmessung des Lissajousnavigators 38% niedriger (0.3°) als der des sphärischen Navigators (0.5°). Im Vergleich zum sphärischen Navigator wurde der maximale Fehler des Lissajousnavigators um 48% reduziert.

Folglich erreicht der Lissajousnavigator ohne offensichtliche Nachteile eine höhere Genauigkeit bei der Rotationsmessung sowie eine höhere Isotropie des Fehlers als der sphärische Navigator. Demzufolge bietet der Lissajousnavigator zwei entscheidende Vorteile, insbesondere für die hochauflösende anatomische Bildgebung.

ABSTRACT

A novel three–dimensional navigator k–space trajectory for rigid body motion detection for Magnetic Resonance Imaging (MRI) — the Lissajous navigator — was developed and quantitatively compared to the existing spherical navigator trajectory [1].

The spherical navigator cannot sample the complete spherical surface due to slew rate limitations of the scanner hardware. By utilizing a two dimensional Lissajous figure which is projected onto the spherical surface, the Lissajous navigator overcomes this limitation. The complete sampling of the sphere consequently leads to rotation estimates with higher and more isotropic accuracy. Simulations and phantom measurements were performed for both navigators. Both simulations and measurements show a significantly higher overall accuracy of the Lissajous navigator and a higher isotropy of the rotation estimates. Measured under identical conditions with identical postprocessing, the measured mean absolute error of the rotation estimates for the Lissajous navigator was 38% lower (0.3°) than for the spherical navigator (0.5°). The maximum error of the Lissajous navigator was reduced by 48% relative to the spherical navigator.

The Lissajous navigator delivers higher accuracy of rotation estimation and a higher degree of isotropy than the spherical navigator with no evident drawbacks; these are two decisive advantages, especially for high–resolution anatomical imaging.

ACKNOWLEDGEMENTS

I would like to thank my supervisors Prof. Nadim Jon Shah and Dr Tony Stöcker for their support and guidance throughout this PhD project, always encouraging my scientific curiousity and sharing their rich knowledge of the field. For this I am truly grateful. Furthermore I would like to thank Prof. Mark Elliott for supervising my stay at the Center for Magnetic Resonance and Optical Imaging at University of Pennsylvania and the DFG for supporting me with a stipend in the international research training group IRTG1328 at RWTH Aachen University. Also my thank goes to my colleagues at the Medical Imaging Physics Group at the Institute of Neuroscience and Medicine – 4 at Forschungszentrum Jülich for their help, fruitful discussions and proofreading of my thesis, especially Eberhard Pracht, Daniel Pflugfelder, Kaveh Vahedipour, Martina Reske, Jörg Felder, Daniel Brenner, Petra Engels, Irene Neuner, Ezequiel Farrher and Johannes Lindemeyer. Their good will and generosity is much appreciated. Last but not least I would like to thank both, my sister Eva and my brother Christoph, for advice and proofreading, and my parents for more than I can put into words.

1 INTRODUCTION

1.1 Motion Artefacts in MRI

Subject motion causes severe artefacts in Magnetic Resonance Imaging (MRI). In particular, 3D sequences with long acquisition times can be severely affected by subject motion. Image blurring, not unlike that known from photography, contrast loss and ghosting artefacts are common motion artefacts observed in MRI. Figures 1.1 and 1.2 show a structural scan acquired with a standard protocol used in many studies. In Figure 1.1, no motion occurred during the scan, whilst in Figure 1.2 motion did occur. The motion artefacts in Figure 1.2 render the image unusable for diagnostic and research purposes.

1.2 Existing Methods for Motion Correction

Since motion artefacts are such a prevalent problem in MRI, a number of strategies for motion correction have been developed. The existing methods for motion correction can be divided into two groups: 1) retrospective motion correction, where the processing is performed

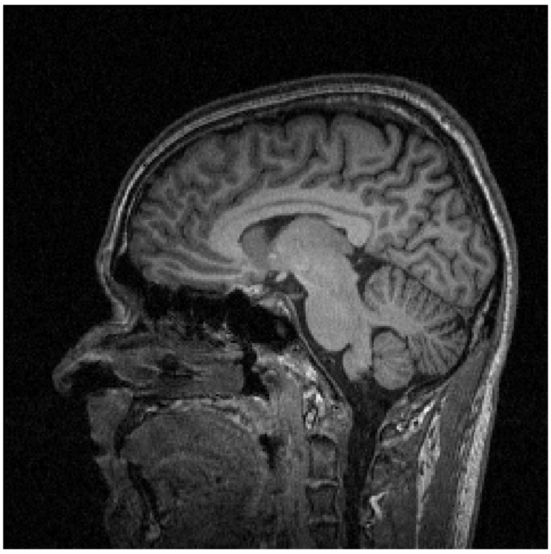

Figure 1.1: Standard MP–RAGE acquisition without motion. The total acquisition time was 9:38 minutes and the spatial resolution was $1mm$ isotropic.

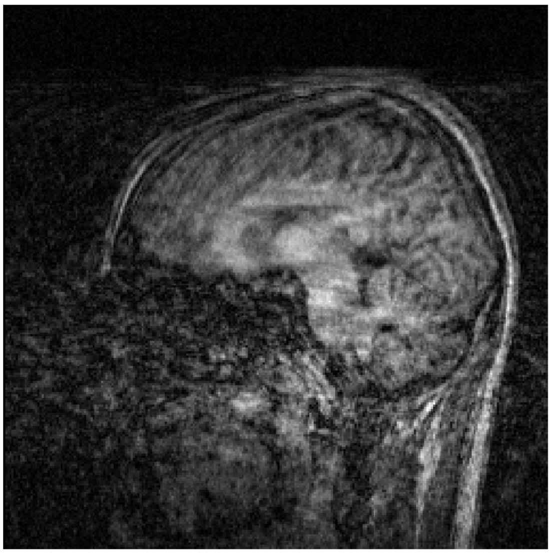

Figure 1.2: Standard MP-RAGE acquisition with motion. The total acquisition time was 9:38 minutes and the spatial resolution was $1mm$ isotropic.

after the data acquisition has been completed, and 2) prospective motion correction, where the data are processed in real–time and the acquisition process is adapted to the motion parameters on the fly.

Retrospective motion correction is widely used in the field of functional MRI. Inter–scan corrections between successively acquired three–dimensional volumes are performed in the image domain, either by a least squares grey–scale matching or more elaborate measures such as mutual information [2], which are methods included into the software packages SPM [3], AIR [4, 5] and FSL [6]. A problem more demanding than inter–scan correction, and the topic of this thesis, is the correction of *intra–scan* motion. That is, the correction of motion occurring during the acquisition of a single volume. One approach for retrospective motion correction for intra–scan motion is the Propeller technique [7]. Propeller motion correction is performed in a reciprocal space referred to as the k–space[1]. During acquisition, blades consisting of the inner k–space lines of a Cartesian acquisition are acquired. Each blade is rotated by some amount around the centre of k–space leading to an overlapping sampling area between the blades in the central k–space region. The data from the overlapping areas are used for retrospective motion correction of in–plane translation and rotation. Whilst Propeller has been shown to reduce motion artefacts and improve image quality [8], it utilises a two–dimensional acquisition and is thus limited to in–plane motions.

One of the first prospective motion correction methods for neuro MRI was PACE [9], which was developed for the correction of inter–scan motion. An image co–registration similar to the one implemented in SPM [3] is performed on-line during acquisition of a time–series of images. The position for the next volume acquisition of the time–series is then adjusted in real–time to the calculated head position.

---

[1] See Section 3.1 for details on k–space.

Prospective intra–scan correction has also been performed with external tracking systems [10, 11, 12]. This approach allows a high update frequency of motion parameters without leading to an increase in scan–time. However, the mouthpiece necessary for external tracking reduces subject compliance, especially during long measurements.

A different concept for prospective motion correction not relying on external hardware for motion tracking is that of three–dimensional navigator echoes. Three–dimensional navigator echoes are essentially short MR acquisitions optimised for the detection and estimation of motion. They can be applied in any MRI scanner without the need for additional hardware and can be included in a variety of sequences for intra–scan motion correction. However, additional scan time is required for the navigator acquisitions. Two such navigators discussed in more detail in this work are the spherical navigator [1] and the cloverleaf navigator [13]. In particular, the concept of the cloverleaf navigator is to apply rapid navigators with short acquisition time, whose individual motion estimates are relatively noisy. Acceptable motion correction results are claimed to be achieved by repeating the navigator acquisition frequently during the sequence [13]. The spherical navigator is the navigator with the highest published accuracy today. It covers the surface of a sphere in k–space with a 3D helical spiral starting from the equator. However, its k–space trajectory imposes a significant drawback on the navigator. Near the poles of the sphere, the slew rate of the gradient waveform increases rapidly beyond the scanner limits. As a consequence, the spherical navigator cannot sample the complete spherical surface, but leaves the poles unsampled. The incomplete sampling of the sphere can have a profound influence on the rotation estimation as rotation estimation relies on the registration of magnitude patterns. Errors can occur when features rotate out of the sampled area. Thus, for rotations perpendicular to the windings of the spiral (cross thread), a reduced accuracy compared to rotations along the windings has been reported [1].

1.2.1 Aim of this Work

The use of a navigator for prospective motion correction for high–resolution images sets high requirements for the design of both the navigator trajectory and the data–processing scheme. For prospective use, the motion parameters have to be calculated rapidly to feed back information to the measurement process in real–time and perform the gradient and frequency corrections necessary for acquisition update. Thus, data processing for prospective motion correction is a performance critical application. Moreover, recent work [14] indicates that motion tracking with a high accuracy is needed for successful motion correction. Thus, not only is the performance of the data processing critical, but an exact navigator is also needed. Increased accuracy of motion estimation likely leads to an increase in navigator acquisition time, which increases the scan–time overhead for the motion correction and complicates inclusion thereof into different sequences.

The aim of this work is to set the cornerstone for prospective navigator–based motion correction by developing a three–dimensional navigator which allows the extraction of exact motion parameters in a minimum acquisition time. This is to be done, by addressing the aforementioned fundamental limitations of the spherical navigator. Thus, an alternative sampling scheme for the spherical surface is to be developed. The novel k–space trajectory has to be able to sample the complete spherical surface whilst staying within the slew rate limits imposed by the hardware. The working hypothesis of this thesis states, that whole–sphere coverage will lead to a higher accuracy and higher isotropy of the rotation estimates, which is desirable for neuro–imaging applications.

2 BASICS OF MAGNETIC RESONANCE IMAGING

2.1 The Origin of the MR Signal

The basis for all magnetic resonance images is the Nuclear Magnetic Resonance (NMR) effect. In this chapter the physical principles which lead to the generation of a basic NMR signal (the free induction decay) will be discussed along with the factors influencing the shape of the signal.

2.1.1 Spin Polarisation

A static magnetic field has an influence on particles with a magnetic moment. Magnetic moments are randomly oriented when no field is present and they occupy a single energy state. When a magnetic field is present, the single state splits into two states with a slight difference in energy given by

$$\Delta E = \gamma \hbar B_0, \tag{2.1}$$

where γ is the gyromagnetic ratio, $\hbar$ is Planck's constant and B_0 is the field strength of the static magnetic field.

Occupation of the two energy states satisfies Boltzmann's statistics. Thus, for a 1.5 Tesla system the spin population difference is approximately $5 \cdot 10^{-6}$. While this is very low, and is the reason MRI is referred to as a low sensitivity modality, it still means that in 1 mm^3 of brain tissue an excess of approximately 10^{14} spins exists in the lower energy state. This difference leads to distortion of the distribution of magnetic moments, resulting in a net magnetisation along the direction of the magnetic field which is used to generate the nuclear magnetic resonance (NMR) signal.[1] By convention we will assume the static magnetic field to be oriented along the positive z–axis.

2.1.2 Precession

The static magnetic field leads not only to spin polarisation but also to spin precession around the axis of the magnetic field in analogy to a spinning top precessing around the axis of the gravitational force. The frequency of the precession w_0 — the Larmor frequency — is given by the Larmor equation

$$\omega_0 = \gamma B_0. \tag{2.2}$$

It is dependent on the gyromagnetic ratio, γ, of the nucleus and is proportional to the field strength, B_0.

---

[1] Increasing spin polarisation and thus increasing signal with larger B_0 is one reason for the trend to high and ultra–high field magnets.

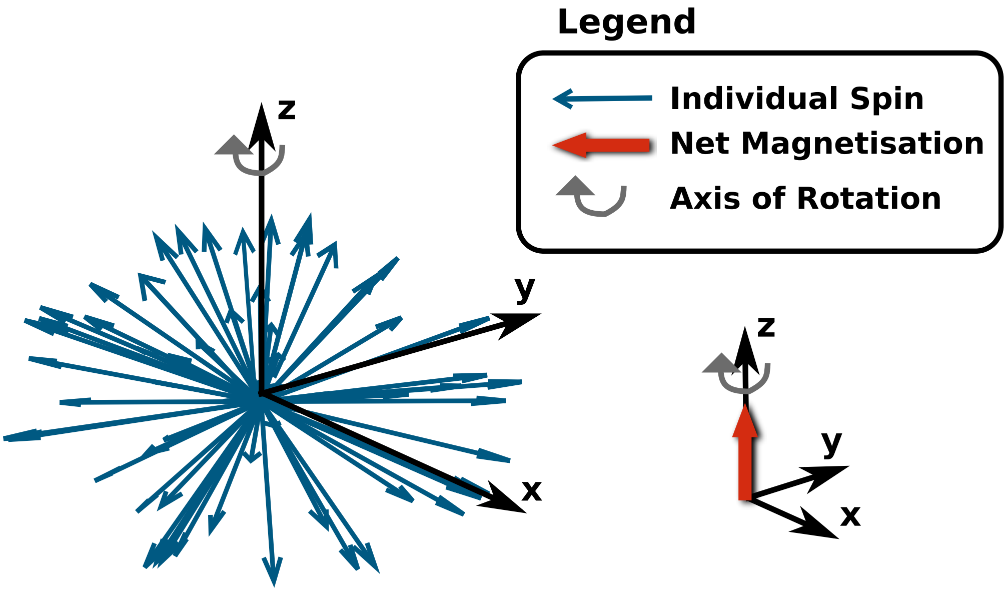

Figure 2.1: Precession of the spins in the static magnetic field. The net magnetisation is oriented along the z–axis as the transverse components of the spins are uniformly distributed and cancel out. Figure adapted from [15].

The phases of the individual precessing spins are uniformly distributed such that, the transverse components of the magnetic moments cancel and there is no net magnetisation in the transverse xy–plane but only along the z–direction. Since only magnetisation in the transverse plane can be detect by the receiver coil, no NMR signal is present at this stage. See Figure 2.1 for a pictorial description.

2.1.3 Spin Excitation

The polarised and precessing spin system can be perturbed by transferring energy to the system, by exposing the spins to a radio frequency (RF) field. Due to their quantum mechanical nature spins

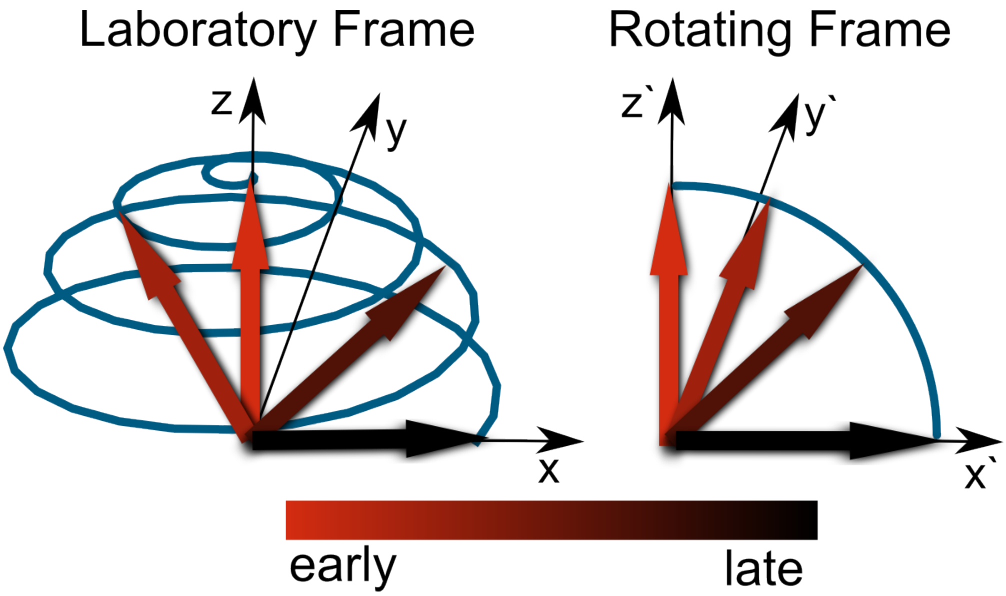

Figure 2.2: Net magnetisation evolution during RF excitation. The magnetisation is rotated away from the z–axis into the transverse plane. On the right this is shown in a frame rotating around the z–axis at the Larmor frequency ω_0. On the left the time evolution of the net magnetisation is shown in the laboratory frame. Figure adapted from [16].

can only absorb energy when the frequency of the external RF field (also referred to as B_1 field) has frequency components at the Larmor frequency of the spins.

An applied RF field at Larmor frequency tips the net magnetisation from the longitudinal z–direction into the transverse xy–plane. Thus, due to the precession there now is a rotating magnetic moment in the xy–plane. This rotating magnetic moment induces a signal in the coil around the object. This is the raw NMR signal detected during an MRI experiment. Figure 2.2 visualises the effect of the RF excitation in the laboratory frame and in the rotating frame of reference. The rotating frame is a coordinate system rotating around the axis of the magnetic field (z–axis) at the Larmor frequency ω_0.

2.1.4 Magnetisation Relaxation

Once the equilibrium state of the magnetisation has been perturbed by the radio frequency pulse and rotated into the xy–plane, it returns back to its equilibrium state. The longitudinal magnetisation along the z–direction returns to its initial state by exchanging energy with the surrounding tissue. The transverse magnetisation in the xy–plane is irreversibly reduced by spin–spin interactions. The behaviour of the macroscopic magnetisation (excitation, precession and relaxation) is described by the phenomenological Bloch equation [17, 18]:

$$\frac{d\vec{M}}{dt} = \gamma \vec{M} \times \vec{B} - \frac{M_x \vec{e}_x + M_y \vec{e}_y}{T_2} - \frac{(M_z - M_0)\vec{e}_z}{T_1} \tag{2.3}$$

where $\vec{e}_i$ are the unit vectors along the three principal axes, $M_{x,y,z}$ are the magnetisation values along the respective axes, $\vec{B}$ is the magnetic field vector, $\vec{M}$ is the magnetisation vector, M_0 is the equilibrium value of the longitudinal magnetisation, T_1 is the tissue dependent longitudinal relaxation time, and T_2 is the tissue dependent transverse relaxation time. The tissue dependence of the relaxation times combined with the timing of the MRI sequence generates the contrast between different tissues.

T_1 Decay

T_1–relaxation is described by the third term in equation (2.3). Solving the Bloch equation for the longitudinal magnetisation component M_z in a static field $\vec{B} = B_0\vec{e}_z$ directly after a 90° radio frequency pulse

($M_z(0) = 0$) yields the following solution:

$$M_z(t) = M_0 \cdot (1 - e^{-\frac{t}{T_1}}). \tag{2.4}$$

After flipping the net magnetisation away from its equilibrium state along the z–direction into the xy–plane, the magnetisation returns back to its equilibrium state along the z–direction by exchanging energy with the surrounding tissue. This process of longitudinal relaxation is also known as the spin–lattice interaction[2].

T_2 Decay

Under the same conditions the solution for the transverse magnetisation in its complex notation $M_+ = M_x + iM_y$ is given by:

$$M_x(t) + iM_y(t) = M_+(t) = M_+(0)e^{i\omega_0 t}e^{-\frac{t}{T_2}}. \tag{2.5}$$

Transient and random local field fluctuations on an atomic level lead to a loss in phase coherence between the spins. This spin–spin interaction decreases the transverse magnetisation in the xy–plane over time. The characteristic time constant of the transverse magnetisation decay is T_2. For all tissues T_2 is shorter than T_1.

2.1.5 Signal Equation

The Bloch equation (2.3) describes the magnetisation behaviour as a function of time and position, but it does not yet describe the signal

---

[2] The term spin–lattice relaxation has historical reasons as NMR experiments were used to gain information on solid state materials, where the surrounding material of the excited spin is a crystal lattice.

$S(t)$ which is induced in the coil during an experiment. To obtain the measured signal in the coil one has to integrate the transverse magnetisation M_+ over the whole volume. Symbolically this relationship is described by the signal equation

$$S(t) = c \int_{Volume} M_+(\vec{r}, t) d^3 r. \tag{2.6}$$

2.1.6 T_2^* Decay

In most real imaging scenarios the transverse magnetisation returns to the equilibrium state faster than the T_2 values of the tissues suggest. The additional shortening is due to inhomogeneities of the static magnetic field which lead to an additional loss of phase coherence between the spins. This additional signal loss is assumed to be an additional exponential decay with the decay constant $T_2^{'}$ [3]. The effective relaxation time, T_2^*, combines the effects of inhomogeneity–induced phase coherence loss ($T_2^{'}$) and spin–spin interactions (T_2) to give $\frac{1}{T_2^*} = \frac{1}{T_2} + \frac{1}{T_2^{'}}$. Thus, by definition $T_2^* \leq T_2$. The envelope of the detected transverse magnetisation experiment is given by

$$M_+(t) = M_+(0) \cdot e^{-\frac{t}{T_2^*}}. \tag{2.7}$$

Figure 2.3 shows the time evolution of the NMR signal, the so–called free induction decay (FID), received after RF excitation in the absence of imaging field gradients.

---

[3] The assumption that field inhomogeneities lead to an exponential decay is not satisfied for all experiments.

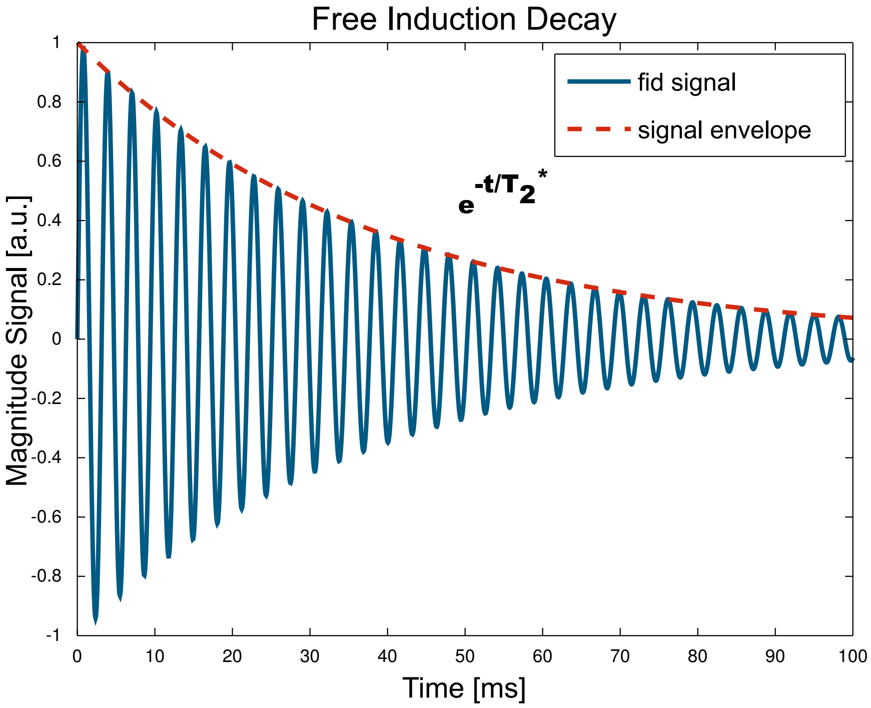

Figure 2.3: Free induction decay: the received NMR signal after RF excitation and in the absence of imaging field gradients. The observed NMR signal oscillates at the Larmor frequency ω_0. The envelope of the signal is an exponential decay with the decay constant $-\frac{t}{T_2^*}$.

2.2 Spatial Encoding

In the previous sections we described the response of spins to an external magnetic field and the resulting NMR signal. The described raw signal — the free induction decay — does not yield any information about the location of the spins. For the generation of an image one needs information on spin location. This information can be gained by using time–varying gradient fields. The gradient fields used in imaging are generally spatially linear varying magnetic fields which are superimposed on the static magnetic field. In an MRI scanner these fields are generated by electrical gradient coils driven by powerful amplifiers which enable a rapid switching of the gradients. Compared to the magnetic field which is on the order of 1.5-3 Tesla for clinical scanners and up to 9.4 Tesla for state–of–the–art research instruments the magnetic field gradients have relatively low maximum field strengths usually on the order of 80 mT with gradient strengths of 40-80 $\frac{mT}{m}$ for whole body scanners.

There are three main concepts for spatial encoding of NMR signals; slice selection, frequency encoding and phase encoding.

2.2.1 Slice Selection

Slice selection is used to only excite spins in a single slice of the imaged object.[4]

A magnetic field gradient along one direction is turned on. Let us assume the gradient G is applied along the z–direction. This leads

---

[4] Slice selection is a special case of selective excitation. With tailored RF pulses the selective excitation of more complex shapes is possible.

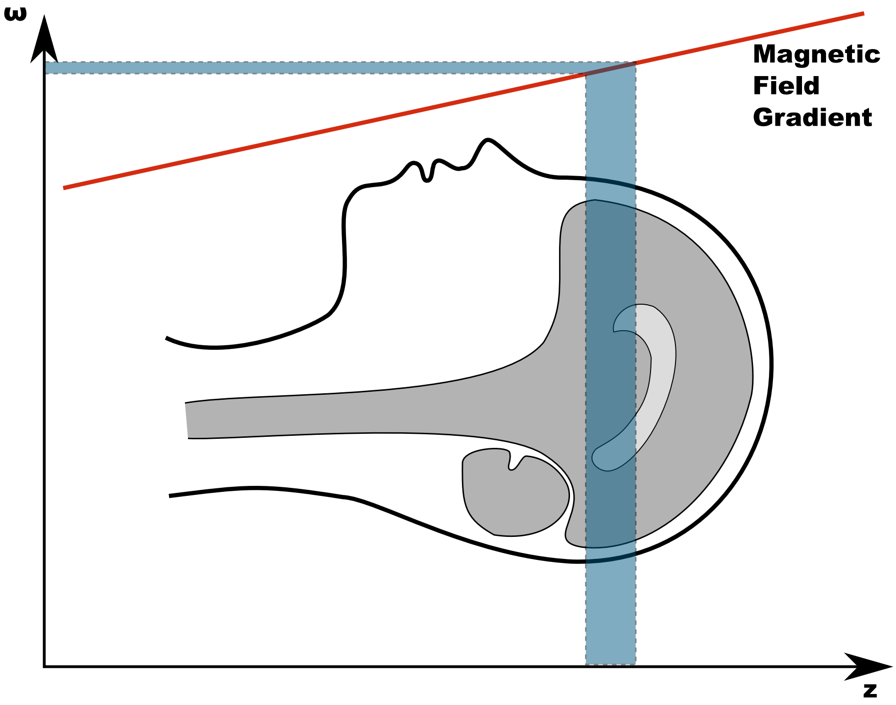

Figure 2.4: Slice selection: a magnetic field gradient here applied along the z–direction leads to a varying resonance frequency along this direction. An RF pulse with a narrow frequency band then selectively excites only the spins in a slice perpendicular to this direction. Figure adapted from [19, p. 106]

to a linear variation in Larmor frequency along this direction.

$$\omega(z) = \gamma \cdot (B_0 + G \cdot z) \tag{2.8}$$

Now a narrow bandwidth RF pulse with frequency ω is played out to excite the spins while the gradient is applied. Only the spins in a given location along z satisfy the Larmor equation. These are the only spins absorbing energy and contributing to the measured signal. See Figure 2.4 for graphical representation.

Since all signals after the slice encoding procedure originate from a single two–dimensional slice of the object, sequences using slice encoding are referred to as two–dimensional sequences. Sequences which excite the entire image volume with each excitation pulse and instead apply phase encoding (Section 2.2.3) in two dimensions are referred to as three–dimensional sequences. Generally, three–dimensional sequences have higher signal–to–noise ratio than their two–dimensional counterparts.

2.2.2 Frequency Encoding

Once the spins (either from a slice or from the whole volume) are excited, the raw MR signal can be read out in the presence of a gradient along a direction (perpendicular to the slice direction in two–dimensional imaging). The gradient applied at the time of the signal readout is a frequency encoding gradient or a readout gradient. It leads to an instantaneous change in the precession frequency of the spins along the direction of the gradient. There now is a linear correspondence between precession frequency and location along the gradient direction. Combined signals measured from all spins can be Fourier transformed to obtain the frequency spectrum of the signal (details in Section 3.1).

Let us examine the following two experiments outlined in Figure 2.5. Two spins are located at separate positions z_1 and z_2 along the z–axis. In experiment a) a 90° RF pulse is applied which tips the spins into the xy–plane. Then the combined signal is acquired. Experiment b) is identical to experiment a), except now a linear field gradient is applied along the z direction during signal acquisition. Fourier transforming the signal from experiment a) will give us a frequency spectrum with only one peak, corresponding to the signal

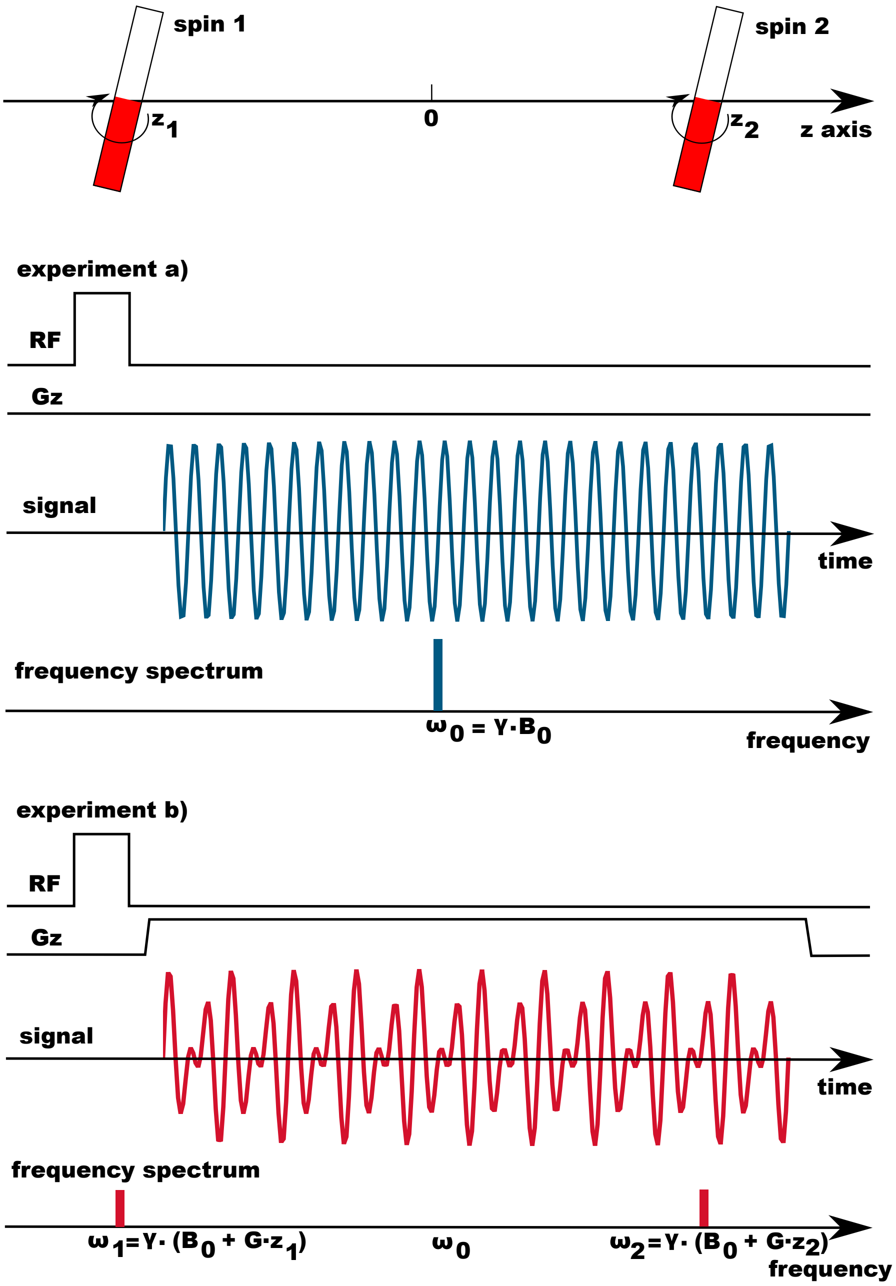
spin 1
spin 2
z1
0
z2
z axis
experiment a)
RF
Gz
signal
time
frequency spectrum
ω0 = γ·B0
frequency
experiment b)
RF
Gz
signal
time
frequency spectrum
ω1=γ· (B0 + G·z1)
ω0
ω2=γ· (B0 + G·z2)
frequency

Figure 2.5: Spatial localisation through frequency encoding: on the top the spatial setup with two spins at discrete locations along the z direction is shown. In experiment $a)$ (middle) an RF pulse is applied and the signal is read out in the absence of gradients. Only a single peak is visible in the frequency spectrum at the resonance frequency ω_0 of the static magnetic field. In experiment $b)$ (bottom) a gradient along the z direction is applied after the RF pulse during signal acquisition. Now, two peaks half the amplitude of the peak in experiment $a)$ are visible at frequencies ω_1 and ω_2. Using the Larmor equation (Eq. 2.8) the position of the spins along the z direction can be calculated from their resonance frequencies.

of both spins. No information on the location of the spins can be extracted. However, in experiment b), the frequency spectrum features two peaks at the frequencies ω_1 and ω_2 — one for each spin — which are half the height of the peak in experiment a). By using the Larmor equation (Eq. 2.8) the exact location of these spins can be obtained from their resonance frequencies.

2.2.3 Phase Encoding

Phase encoding is used to encode the MR signal in one (2D imaging) or two (3D imaging) directions. For phase encoding a gradient (orthogonal to the slice and frequency encoding direction) is applied between the excitation pulse and the signal readout. The gradient moment varies linearly along the phase encoding direction, which leads to a linear phase shift of the spins along the phase encoding direction. This constitutes a pseudo frequency encoding along the phase encoding direction.

Frequency and phase encoding are theoretically equivalent methods of spatial localisation. The difference between the two localisation methods is that the frequency encoding gradient is applied during the readout whilst the phase encoding gradient is applied *before* the signal readout. Additionally, and maybe the most important difference in practice is, that phase encoding has to be repeated once for every datum point acquired in the phase encoding direction whereas during frequency encoding all data points in readout direction can be acquired with a single encoding step. Thus, phase encoding in conventional gradient echo and spin echo methods is the encoding technique with the highest influence on the acquisition time. To reduce acquisition time it is beneficial to minimise the amount of phase encoding steps needed.

2.3 Sequences

indexsequence MRI is unique in the field of medical imaging methods as it has the ability to produce images with a large variety of different contrasts, each of which carries unique information. The physical basis for the different contrast is the tissue dependent transverse and longitudinal relaxation times T_1 and T_2. The multitude of images are achieved by changing the, the way and the timing in which the polarized spins are flipped and the signal is read out — the *MRI sequence*. Together with the tissue dependent relaxation mechanisms alluded to above, many different contrasts can be optimized for the diagnostic question at hand. In the following sections, the basic MRI sequences relevant to the work in this thesis are introduced. The most important parameters for contrast variation in the sequences described in this section are the echo time, TE, the repetition time, TR, and the flip angle, α.

2.3.1 Gradient Echo

The most basic sequence is the gradient–recalled echo (GRE or GE) [20]. An RF–pulse — often referred to as α–pulse — tips the net magnetisation into the xy–plane in the two–dimensional case during the presence of a slice selection gradient followed by a slice refocusing lobe. After excitation, a phase encoding gradient is applied in a direction orthogonal to the slice selection gradient. After a delay which assures the echo is refocused at the desired echo time (TE)[5] the readout gradient is applied along a direction orthogonal to the slice selection and the phase encoding gradient. The readout gradient consists of two parts: a dephasing part (the negative lobe in Figure 2.6) and the actual readout part, during which the signal is acquired. An elegant way to describe and visualize sequences is a *sequence diagram*. A sequence diagram is a schematic representation of a sequence, where the abscissa is the time axis of a sequence diagram. Along the ordinate, multiple axes are arranged: one for each event type of the sequence (RF pulses, gradients, readout, signal). The sequence diagram of a gradient echo sequence is shown in Figure 2.6. After the echo readout as shown in Figure 2.6, residual magnetisation can be removed from the imaging process by applying additional gradients or modifying the phase of the subsequent RF pulses. This process is known as spoiling. GRE sequences are differentiated depending on the spoiling applied after the readout. The Fast Low Angle Shot (FLASH) sequence [20] is a spoiled gradient echo, whereas steady state free precession (SSFP) sequences refocus the available magnetisation in the transverse plane. This leads to higher signal–to–noise but may lead to a reduced T_1 contrast [21].

---

[5] The echo time (TE) is the time between the excitation and the refocusing of the echo.

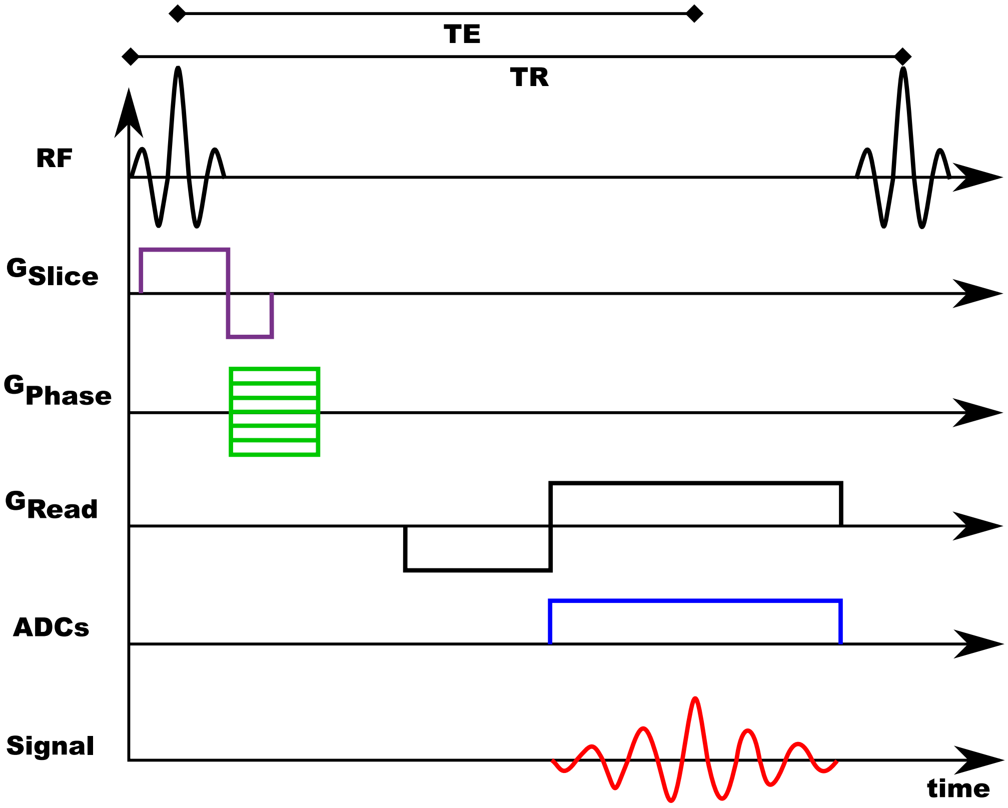
TE
TR
RF
G_{Slice}
G_{Phase}
G_{Read}
ADCs
Signal
time

Figure 2.6: Sequence diagram of a gradient recalled echo sequence: an RF pulse flips the magnetisation into the transverse plane in the presence of a slice–encoding gradient. A gradient along the phase encoding direction is applied. After a delay required for the proper echo time (TE) a readout gradient is applied and the signal is digitised.

2.3.2 Spin Echo

Another basic imaging technique is the spin echo sequence which is based upon Erwin Hahn's pioneering article "Spin Echoes"[22]. A sequence diagram of a two–dimensional spin echo sequence is shown in Figure 2.7. A 90° pulse tips the net magnetisation into the xy–plane with coherent phase. After the initial excitation, the spins lose their phase coherence as described in section 2.1.6 due to T_2^* decay. Now a phase encoding gradient is applied. After half of the desired echo time has passed a 180° pulse is applied which flips the spins over in the xy–plane. Finally the readout gradient is applied perpendicular to the slice encoding and phase encoding direction. The 180° pulse leads to a rephasing of spins which were dephased due to static field inhomogeneities (T_2^* effects). Thus, the signal, S, is proportional to $e^{-\frac{t}{T_2}}$.

2.3.3 MP–RAGE — An Advanced Sequence for Neuro–imaging

For neuro–imaging, more advanced sequences are available which yield a superior T_1–weighted contrast between grey and white brain matter and thus depict a better map of the anatomy. One such sequence heavily used in neuroscience is the three–dimensional Magnetisation Prepared Rapid Acquisition Gradient Echo (MP–RAGE) proposed in [23] and optimised for structural brain imaging in [24]. The sequence utilises a 180° inversion pulse followed by a waiting period for optimal contrast generation which is followed by a gra-

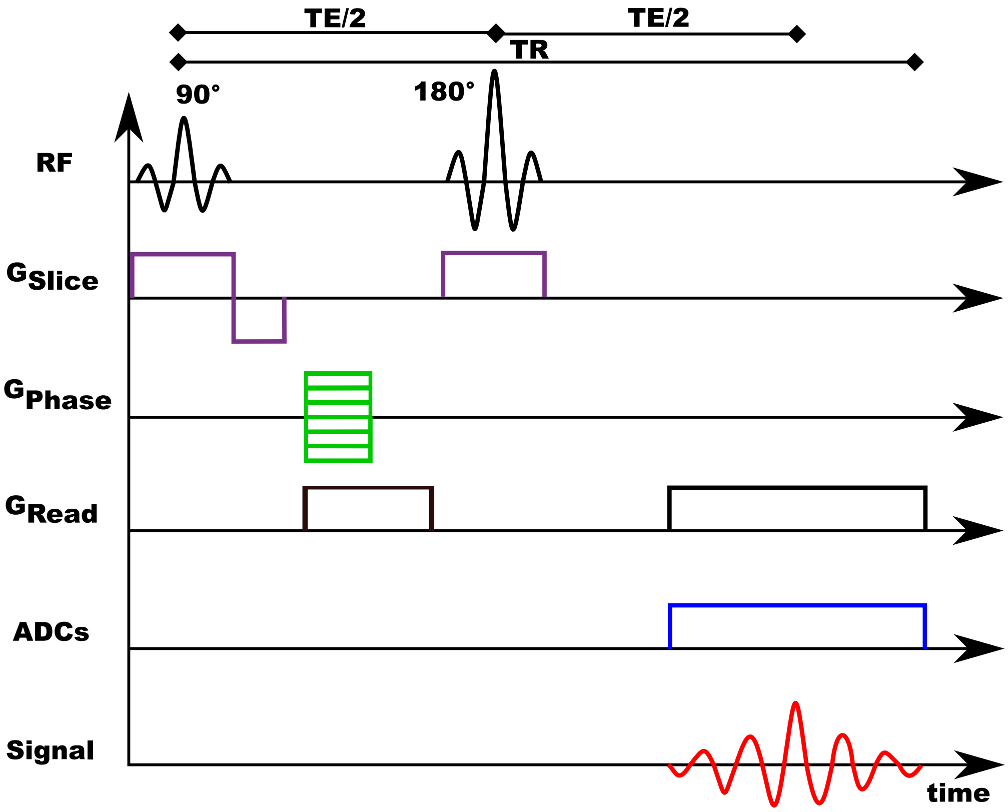
TE/2
TE/2
TR
90°
180°
RF
G_{Slice}
G_{Phase}
G_{Read}
ADCs
Signal
time

Figure 2.7: Sequence diagram of a spin echo sequence: a $90°$ RF pulse flips the magnetisation into the transverse plane. After half of the desired echo time (TE) a $180°$ pulse is applied which flips the magnetisation over in the transverse plane. This leads to restored phase coherence of the spins at $\frac{TE}{2}$ after the $180°$ inversion pulse.

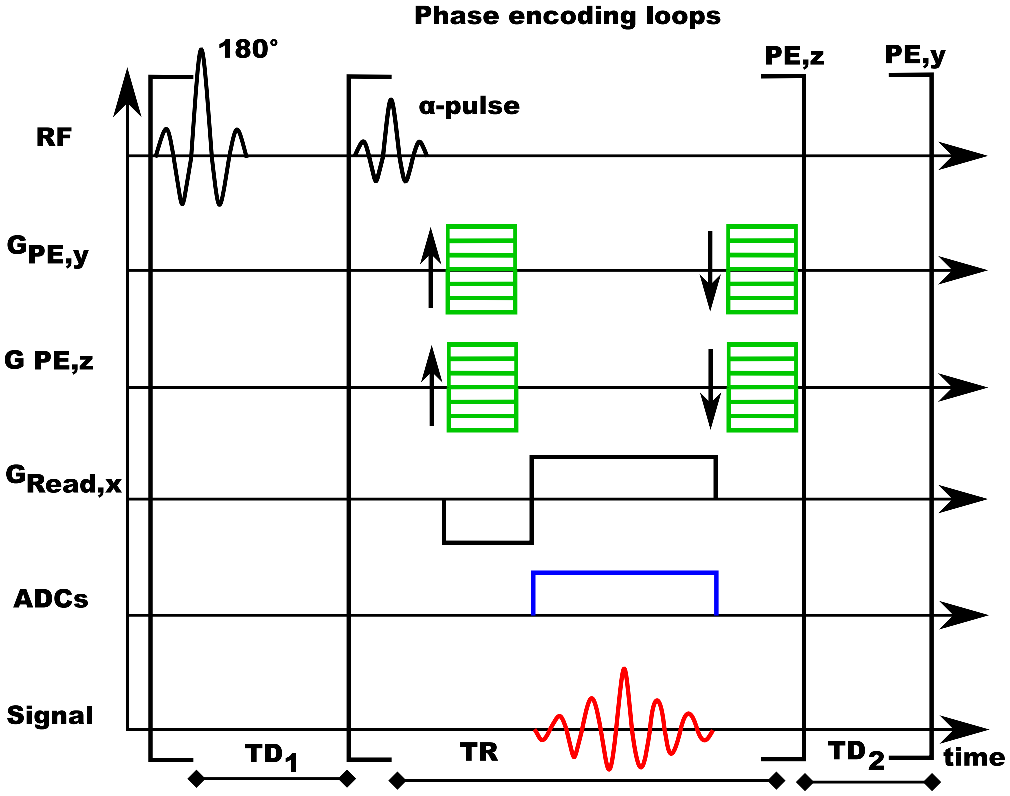
Phase encoding loops
180°
PE,z
PE,y
α-pulse
RF
G PE,y
G PE,z
G Read,x
ADCs
Signal
TD1
TR
TD2
time

Figure 2.8: Sequence diagram of a 3D MP–RAGE sequence: the magnetisation is prepared in the outer phase encode loop with a 180° inversion pulse. After an inversion delay time TD_1 a GRE type readout is applied for readout in the inner phase encode loop, which is followed by a recovery time TD_2 for contrast generation.

dient echo readout of a full phase encoding cycle of one of the two phase encoding directions. After the readout another wait period is necessary to achieve optimal contrast. A sequence diagram of an MP–RAGE sequence is shown in Figure 2.8.

2.4 MRI Hardware

A complex set of hardware is necessary for the successful generation of an MR image. In this section a brief description of the hardware used in state–of–the–art MRI machines is given based on the description in [25].

2.4.1 The MRI Scanner — an Overview

Figure 2.9 depicts a simplified schematic of a modern, horizontal–bore MRI scanner. The magnet and patient table are located inside a room protected from radio frequency noise by a radio frequency shield. Inside the magnet, the gradient coils are positioned, which in turn enclose the radio frequency coil. Connections from the hardware room are fed through filters to avoid breaking the RF screening. A set of computers is responsible for running the MRI experiment, analysing the data, and displaying the user interface. However, for simplicity only a single computer is depicted in Figure 2.9. On the console, the operator specifies and starts the measurements and evaluates the images. Then RF pulse shapes are calculated and sent to the RF amplifier which drives the RF coil. The currents for the gradient waveforms are calculated and converted to analogue signals by the digital–to–analogue converter (DAC) and sent to the gradient amplifiers which feed the gradient coils. Signals from the net magnetisation in the xy–plane are received through the RF receiver, digitised by the analogue–to–digital converter (ADC), and send back to the computer. Finally, an image is reconstructed and displayed on the console.

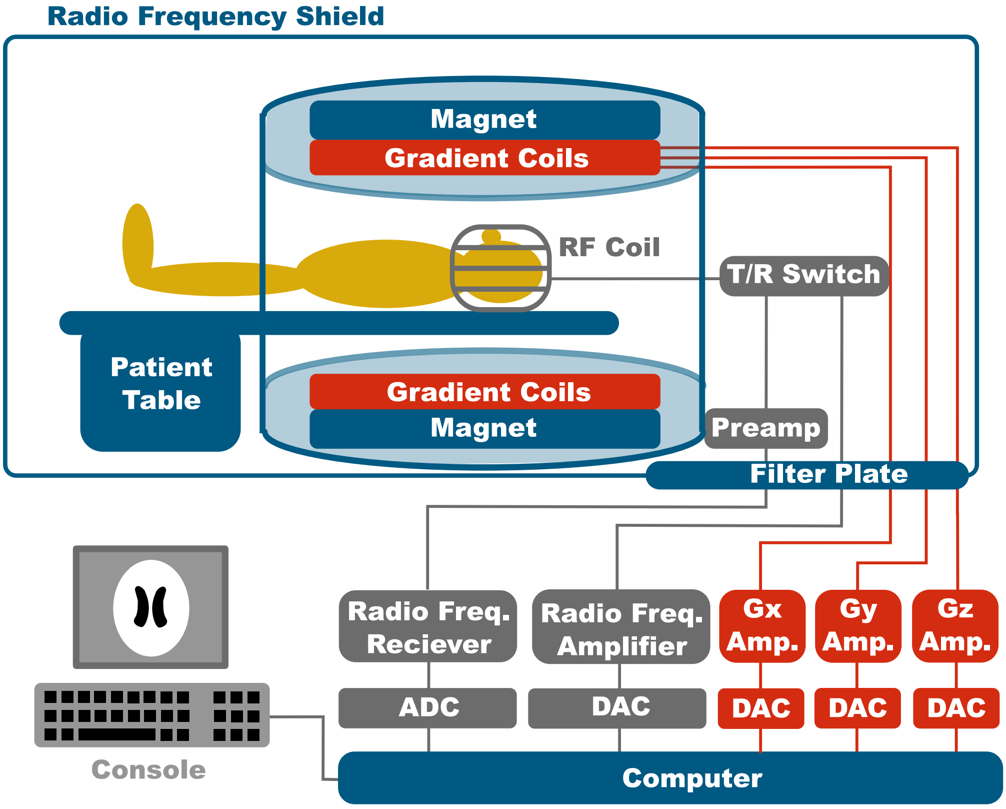
Radio Frequency Shield
Magnet
Gradient Coils
RF Coil
T/R Switch
Patient Table
Gradient Coils
Magnet
Preamp
Filter Plate
Radio Freq. Reciever
Radio Freq. Amplifier
Gx Amp.
Gy Amp.
Gz Amp.
ADC
DAC
DAC
DAC
DAC
Console
Computer

Figure 2.9: Simplified schematic of the hardware of a MRI scanner adapted from [25]. For details see text.

2.4.2 The Magnet

The static field magnet of an MRI scanner usually consists of a solenoid coil of superconducting wire submerged in liquid helium. The resistance in the superconductor drops to zero when it is cooled below its critical temperature. Thus, a current once injected into the superconductor will flow continually without the need for a feeding electrical source. However, energy is still needed to keep the superconductor below its critical temperature.

2.4.3 The Gradient System

The strong static magnetic field is superimposed by a much smaller magnetic gradient field which is produced by room temperature gradient coils. The gradient coil system consists of three sets of coils, one for each physical axis (x, y, z). In a simplified view, the gradient system of the most common imaging magnet type, the horizontal bore magnet, consists of a Maxwell pair for generation of a gradient field in z–direction and a Golay set for gradients along x– and y–directions[6]. A schematic of this configuration is shown in Figure 2.10. The gradient coils are driven by powerful, amplifiers with rapid rise times. In the scanner used in this work, the gradient amplifiers generate a maximum current of $625A$ and a maximum voltage of $2000V$ with a rise time of $200\mu s$.

---

[6] The actual gradient coil geometry in a state–of–the–art scanner is much more complex. Gradient coils have a non–trivial geometry and are designed by sophisticated methods, one of which is the numerical distribution of current [26] on a cylindrical surface to achieve optimal performance. The interested reader is directed towards [27] for a review of gradient coil design methods.

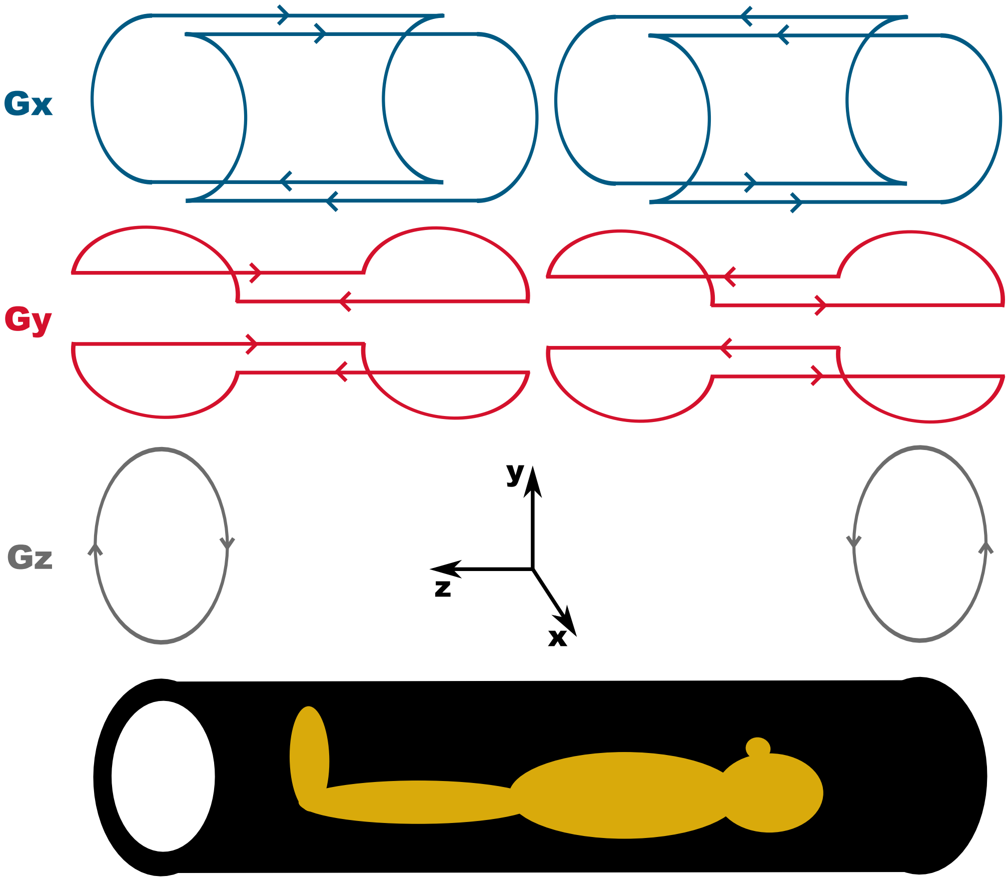

Figure 2.10: Schematic of the gradient coils. A Maxwell pair for the z–axis and a Golay set for gradients along the x– and y–axis.

Slew rate Limitations of the Gradient System

Even though the gradient systems have seen tremendous improvements over the last decade, the scanner hardware imposes limits on the MRI experiments. One such limit imposed by the gradient system is the slew rate limit. The slew rate is the rate at which the gradient field is changed with respect to time. It is measured in $\frac{mT}{m \cdot s}$. The slew rate limit of the scanner used in this work was $200 \frac{mT}{m \cdot s}$.

Gradient Fidelity

The fast switching of the currents in the gradient coils introduces eddy currents in conducting material nearby, which reduces gradient fidelity and changes the static field by introducing a time–varying component. The effects of eddy currents can be reduced by gradient pre–emphasis which is performed by many MRI hardware/software manufacturers. Additionally, a multitude of other factors can influence the gradient fidelity such as varying amplifier gain factors and temperature fluctuation. In later chapters it will be shown that correction of gradient infidelities can improve motion correction results.

2.4.4 The Radio Frequency System

For transmission, the required RF waveform is generated by the computer and converted to an analogue signal by a digital–to–analogue converter, amplified by the radio frequency amplifier and sent to the RF coil through a transmit/receive switch. The generated B_1 field is a magnetic field perpendicular to the static B_0 field. The B_1 field rotates the net magnetisation away from the z–direction into the xy–plane. During reception, the RF coil picks up the signal because of the rotating magnetisation in the xy–plane. The signal passes the transmit/receive switch to the receiver and is digitised by an analogue–to–digital converter.

2.5 Physiological Limits to the MRI Experiment

In the previous section, the MRI scanner hardware was briefly introduced and some limitations arising from the gradient hardware were covered. However, hardware constraints are not the only limitations imposed on an MRI experiment. The rapid switching of electromagnetic fields can have physiological effects. The most important ones are the absorption of energy and the consequential heating of living tissue by the RF field and peripheral nerve stimulation by rapid gradient switching. Both of which are covered in this section.

2.5.1 Specific Absorption Rate

The radio frequency field used to flip the spins in order to generate an MR signal that can be used for image generation deposits energy in the body. The specific absorption rate (SAR) was defined as a measure of how much power is deposited per mass of tissue. The unit of the SAR is $\frac{W}{kg}$. To reduce physiological reactions and to avoid RF burns, MRI scanners adhere strict SAR controls. The International Electrotechnical Commission (IEC) has set the current limits for the SAR in MRI to 8 $\frac{W}{Kg}$ of tissue for any 5 minutes or 0.4 $\frac{W}{Kg}$ for the whole body averaged over 15 minutes [28]. Due to the shorter wavelength of the RF pulses at high magnetic field strengths, SAR and SAR hotspots increase. Thus, it is important especially at high field strengths to design MRI acquisitions such that they use minimal RF energy.

2.5.2 Nerve Stimulation

According to Faraday's law of induction the application of time varying gradient fields during an MRI scan induces an internal electric current in the imaged person. In [29] it was estimated that a magnetic field change of 1 $\frac{T}{s}$ leads to a current density of nearly 1 $\frac{\mu A}{cm^2}$. If the gradients are switched rapidly during an MRI examination, the induced electromagnetic force can become larger than the nerve stimulation threshold. This is usually noted as a mild tingling sensation [30]. The greatest occurrence of nerve stimulation is reported by gradient switching along the anterior—posterior direction when the patient is in the supine position [30]. The IEC has set a $\frac{dB}{dt}$ limit of 20 $\frac{T}{s}$ for a gradient switching greater or equal than 120 μs [28]. However, the standard also supports a controlled operating mode with higher limits ranging from 20 to 600 $\frac{T}{s}$ depending on the switching time. This first level operation mode has to be activated explicitly by the physician.

3 THEORY OF NAVIGATOR–BASED MOTION CORRECTION

3.1 k–Space

When working with raw MRI data, the concept of k–space is a very useful auxiliary construct that tremendously eases the description of MR experiments. k–space is a frequency space reciprocal to the spatial coordinates. It was first introduced into MRI in 1983 independently by Ljunggren [31] and Twieg [32]. The raw (spatial frequency) data acquired during the MRI scan can be ordered according to the spatial frequencies they represent. The resulting space is the so–called k–space, named after the wave vector, $\vec{k}$, according to which the signals are sorted. In the context of this thesis the k–space formalism is of the utmost importance, since the three–dimensional navigator developed here is, in essence, a highly optimized k–space sampling pattern. Thus the k–space formalism will be introduced analytically and pictorially.

3.1.1 Analytical Description

Analytically, image space and k–space are linked by the Fourier transform [33]. The Fourier transform decomposes a function, f, into a set of periodic functions. The continuous Fourier transform, $F(k)$, of a one–dimensional function $f(x)$ is given by:

$$F(k) = \int_{-\infty}^{\infty} f(x) e^{-i2\pi xk} dx. \tag{3.1}$$

It is reversible in the sense that $f(x)$ can be regained by the inverse Fourier transform which is defined as:

$$f(x) = \int_{-\infty}^{\infty} F(k) e^{i2\pi xk} dk. \tag{3.2}$$

In the continuous case, the function is decomposed into an infinite set of periodic functions. However, more relevant for medical imaging is the discrete Fourier transform of a function, $f(x)$, sampled N times with equidistant spacing; this is given by:

$$F_k = \sum_{n=0}^{N-1} f(x_n) e^{-\frac{i2\pi}{N} nk}, \tag{3.3}$$

where x_n denotes the nth sample point and $k = 0, ..., N-1$. Its inverse is given by

$$f_x = \frac{1}{N} \sum_{k=0}^{N-1} F_k e^{\frac{i2\pi}{N} nk} \tag{3.4}$$

for $n = 0, ..., N-1$.

Rewriting the integral in the signal equation (Eq. 2.6) as a function of the physical axes for a two–dimensional imaging experiment leads to:

$$s(t) = \int_x \int_y M_{xy} e^{-i2\pi k_x(t)x} e^{-i2\pi k_y(t)y} dx dy, \tag{3.5}$$

with

$$k_i = \frac{\gamma}{2\pi} \int_0^t G_i(\tau) d\tau, \tag{3.6}$$

whereby in (Eq. 3.6), γ is the gyromagnetic ratio of the resonating nucleus and i denotes one of the imaging directions x or y.

Comparing Equations 3.1 and 3.5 it becomes apparent, that the measured raw signal $s(t)$ at time t always equals a value of the Fourier transform of the transverse magnetisation distribution M_{xy} at a spatial frequency k_{xy}. Thus, the process of MRI can be seen as a problem of measuring the signal $s(t)$ in such a way that an image can be reconstructed by employing the Fourier transform[34].

This shows the immense importance of the discrete Fourier transform for imaging in general and MRI in particular. The direct calculation of the discrete Fourier transform from the definition in Eq. 3.3 requires $\mathcal{O}(N^2)$ operations[35]. A family of algorithms, the Fast Fourier Transform (FFT) algorithms [35, 36, 37], are available for efficient numerical calculation requiring only $\mathcal{O}(NlogN)$ operations[35]. Because of its speed and robustness, the majority of clinical MRI applications utilise the Fast Fourier transform for image reconstruction.

3.1.2 Pictorial Description

The analytical description of k–space given above can be easily visualized; as mentioned above, spatial frequencies are ordered in k–space according to their wave vector $\vec{k}$ (see Figure 3.1). Each k–value represents a spatial frequency of an periodic plane wave. The mag-

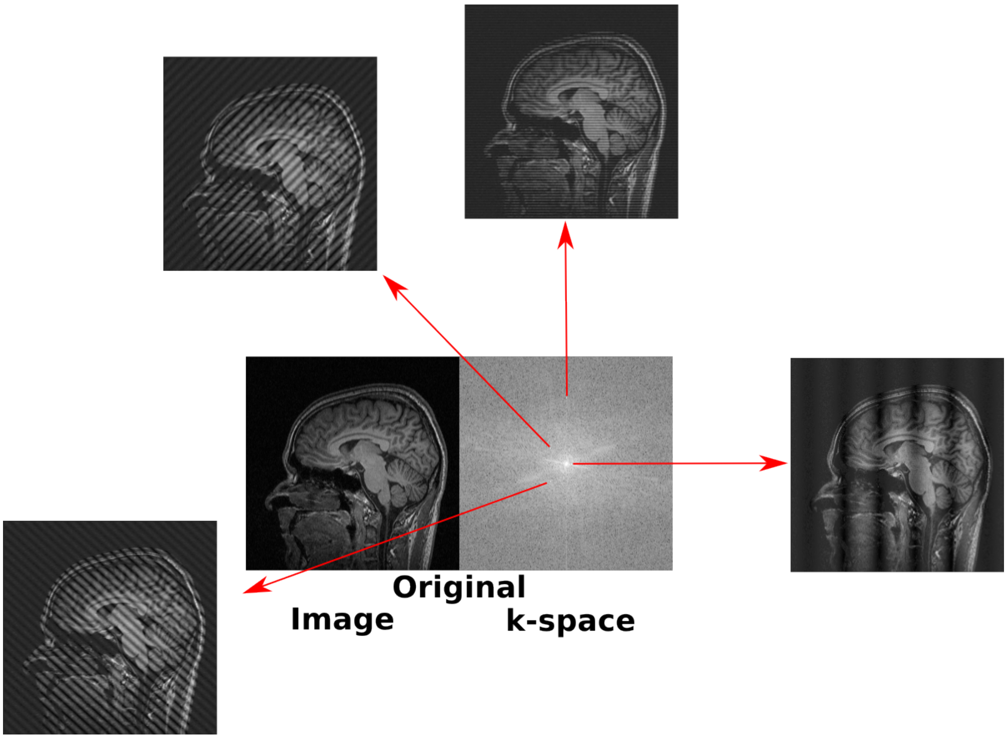

Figure 3.1: Pictorial description of k–space adapted from [19, p. 117] and [38]. Spatial frequencies are ordered in k–space according to their frequency and direction. The weighting factor of a single frequency in the original k-space has been increased to create the surrounding images. The further away from the centre, the higher the frequency of the corresponding stripe pattern.

nitude value at any given position of k–space is a weighting factor. This weighting factor quantifies the contribution of the spatial wave with the given k–vector to the final image. The final image is then composed by a weighted sum of all the spatial waves belonging to each frequency in k–space.

3.2 Effect of Rigid Body Motion on k–space

Rigid body motion has a well–defined influence on the raw k–space data. The effects described in this section are the basis for all rigid body motion estimation and correction techniques operating in the inverse space. An important property of k–space is the fact that the effects of translation and rotation of an object can be separated. Translations only affect the phase and rotations only affect the magnitude of the raw signal.

3.2.1 Translations in k–Space

The effect of rigid body translation on the phase of the signal is given by the Fourier shift theorem [33]. The Fourier shift theorem states that if a function $f(x)$ has the Fourier transform $F(k)$, then the shifted function $f(x-a)$ has the Fourier transform $F(k)e^{-iak}$.

3.2.2 Rotations in k-Space

A rotation in object space is a rotation of the magnitude data in k–space around the central point in k–space. The phase signal is not affected by rotations (apart from signal–to–noise changes due to the rotated magnitude). In Figure 3.2 a slice of the MNI brain phantom [39] is shown along with the image of the same slice rotated by 35°. The k–space magnitudes of both images are shown on a logarithmic scale. It is apparent, that the magnitude features have been rotated the same angle as has the image.

3.3 Currently Available Navigated Motion Correction Techniques for MRI

The severe limitations imposed by motion on MRI have given rise to the development of a multitude of motion correction techniques. This section gives an overview over the most important concepts and briefly discusses their virtues and drawbacks.

3.3.1 Line Navigators for Breath–Motion Triggering

Historically, one of the first navigator techniques used for motion correction or rather motion discrimination is the pencil beam navigator [40],[41] employed for the measurement of motion induced by breathing for thorax and abdominal imaging. Here, the navigator is not used to track rigid body motion, but rather deformation or displacement of the internal organs. A line navigator acquisition is spliced into the imaging sequence which tracks the movement of the diaphragm. Thus, the data can be either retrospectively ordered into a k–space which is acquired at the same position in the breathing cycle or the acquisition of the data can be triggered by the diaphragm being in a certain position range.

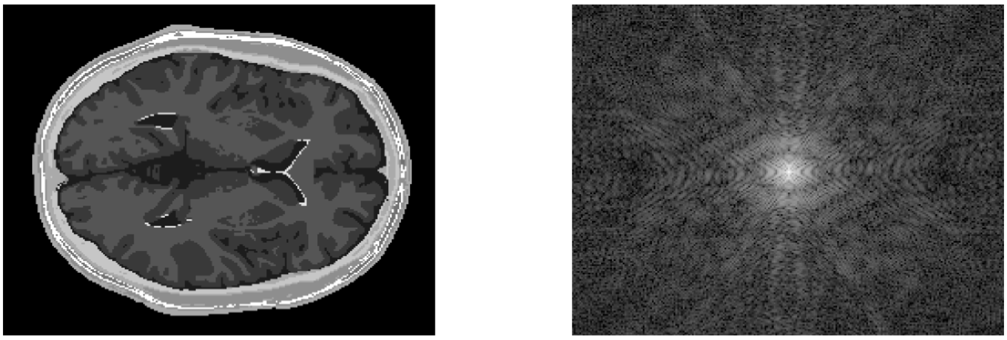

unrotated image

k-space magnitude
unrotated image

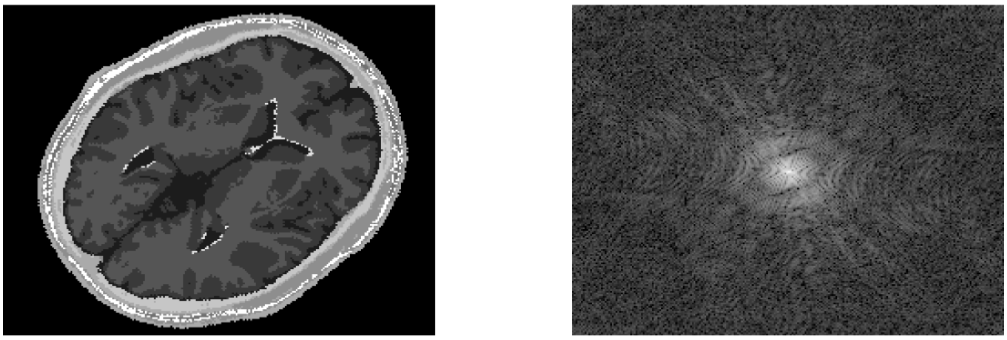

rotated image

k-space magnitude
rotated image

Figure 3.2: The upper row shows a slice from the MNI brain phantom [39] on the left and the magnitude of the corresponding k–space on the right. The lower row shows the same slice rotated by 35°on the left and the magnitude values of the corresponding k–space on the right. The magnitude values are rotated by the same amount as the brain slice in the image.

3.3.2 Three–Dimensional Navigators for Rigid Body Motion Correction

The well–defined influence of rigid body motion on the raw MR signal described in section 3.2 prompted the development of advanced navigators for rigid–body head motion. The development was initialised with the orbital navigator [42] for in–plane rotation correction, which was later extended to three dimensions with the spherical navigator [1] covered in the next section. Another approach related to the spherical navigator is the cloverleaf navigator [13] which was developed in 2006.

Spherical Navigator

The spherical navigator covers 85% of the spherical surface in k–space with a double spiral trajectory. The acquisition begins at the equator and moves in a spiral fashion towards a single pole with a constant sampling density spiral given by:

$$\begin{aligned} k_x(n) &= cos(\sqrt{N\pi} sin^{-1} k_z(n)) \cdot \sqrt{1-k_z(n)^2} && (3.7)\\ k_y(n) &= sin(\sqrt{N\pi} sin^{-1} k_z(n)) \cdot \sqrt{1-k_z(n)^2} && (3.8)\\ k_z(n) &= \frac{2n-N-1}{N}, && (3.9) \end{aligned}$$

where N is the total number of sampling points in the navigator and n ranges from 1 to N. A plot of the spherical navigator trajectory is shown in Figure 3.3. The rationale behind covering a spherical shell in k–space is the suitability for rotation estimation. Points far away from the axis of rotation give a better rotation estimate than points

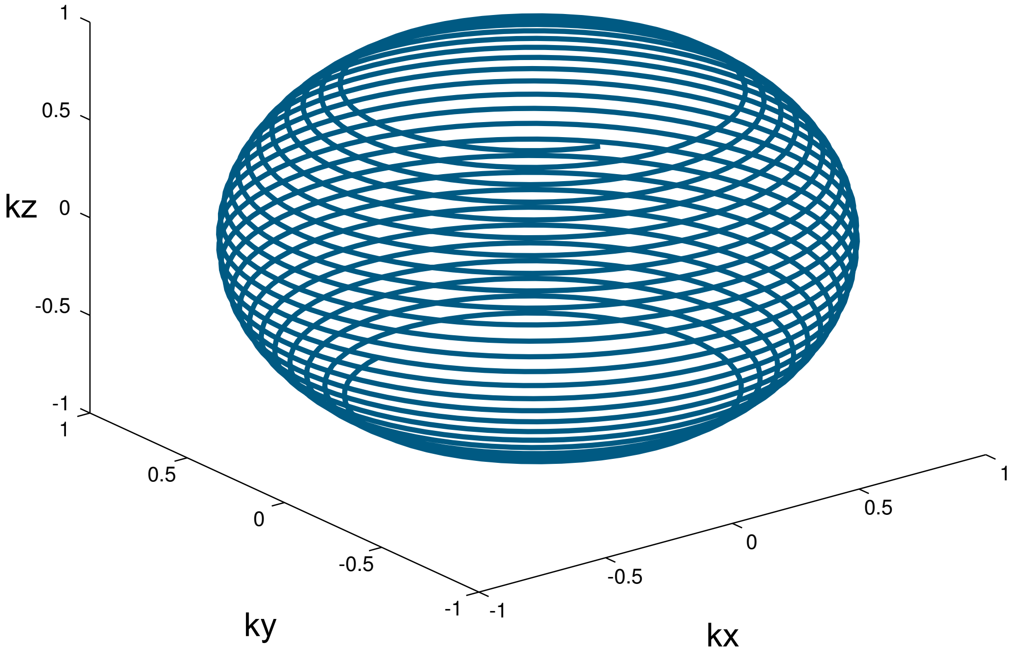

Figure 3.3: The k–space trajectory of the spherical navigator as proposed in [1]. Eighty–five percent of the spherical surface is covered in a two–shot acquisition. The trajectory moves in a spiral fashion from the equator outwards towards a pole cap. With a separate excitation pulse the second hemisphere is sampled.

close to the axis. When sampling a spherical surface, no matter around which axis the object was rotated, there are always sampling points far away from this axis of rotation.

The spherical navigator was proposed as a two shot method, where each hemisphere requires its own RF excitation pulse [1]. Due to an excessive gradient slew rate increase near the poles of the sphere, the spherical navigator cannot sample the complete spherical surface. Thus, to stay within the hardware limits of the scanner, the poles are left unsampled. Figure 3.4 shows the gradients and slew rates for the spherical navigator with a 15% cut–off at the poles and for a trajectory covering the whole surface[1]. The spherical navigator was originally proposed with a pole cut–off of 15% and a total acquisition time of 27ms [1].

Non–uniform accuracy of rotation estimation was reported for the spherical navigator. Cross thread rotations, this are rotations perpendicular to the windings of the sampling scheme, are measured with lower accuracy than rotations along the direction of sampling [1]. Thus, for the spherical navigator there is one preferential axis with higher accuracy.

Cloverleaf Navigator

The cloverleaf navigator [13] follows a different approach. Its *k*–space trajectory consists of three quarter arcs centred on the *k*–space centre and each one oriented perpendicular to one of the principal axes. The quarter arcs are connected by line navigators which go along

---

[1] For clarity the slew rates in Figure 3.4 are plotted for the trajectory going from one pole cap to the other and not from the equator outwards.

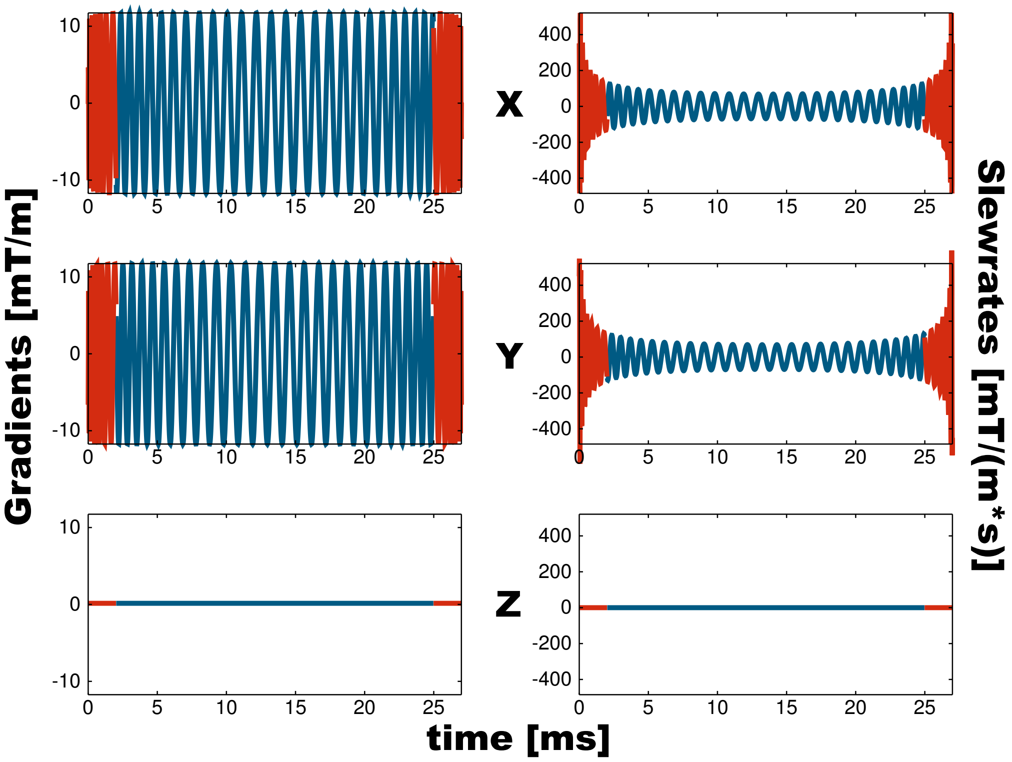

Figure 3.4: The gradients and slew rates for the spherical navigator. The blue line denotes the portion of the trajectory used in [1]. Plotted in red are the gradients and slew rates necessary for whole sphere coverage with the spherical navigator.

the principal axes (one for each line navigator). The data from the quarter–arc acquisitions are used for rotation estimation, whilst the data from the line acquisitions are used for translation estimation along the three principal axes. The total acquisition time of the cloverleaf navigator on a Siemens Magnetom Trio is 4.2 ms [13]. This rapid acquisition is an advantage of the cloverleaf navigator, as it can be included in sequences with a short repetition time (TR) such as FLASH [20]. No value for the precision of the cloverleaf navigator measured relative to a gold standard has been reported. However, it was noted that the individual measurements are relatively noisy [13].

3.4 The Lissajous Navigator

A dependable motion correction is essential for MRI in general and especially so for high–resolution imaging. The available navigator approaches for rigid body motion correction suffer from limitations. The spherical navigator exhibits an anisotropic accuracy of the rotation estimate. The cloverleaf navigator is fast, but its motion parameters are noisy. Thus, it is not well suited for high–resolution imaging. This prompted us to develop a novel, improved navigator for rigid–body motion correction utilising a Lissajous type trajectory, which is presented in this section.

3.4.1 Conventional 2D Lissajous Figures

Conventional Lissajous figures in two dimensions are given by the following equations:

$$x = A \cdot sin(\alpha \cdot t) \tag{3.10}$$

$$y = B \cdot sin(\beta \cdot t + \Phi), \tag{3.11}$$

where x and y denote the displacement along the two orthogonal coordinate axes, A and B are the amplitude scaling factors of the sinusoidal motions along x and y, and α, β are the frequencies of the sinusoidal motion and Φ is the relative phase between the waves. The resulting trajectory is highly dependent on the frequencies α and β and is closed when their ratio is a rational number. Figure 3.5 shows an example of a conventional two–dimensional Lissajous figure. Because of their capabilities to traverse k–space rapidly and within the slew rate constraints given by the scanner hardware, Lissajous trajectories have previously been applied to non–Cartesian magnetic resonance imaging [43],[44],[45].

3.4.2 Lissajous Trajectory on the Sphere

The moderate slew rate requirements and the alternating direction of k–space traversal resulting from the sinusoids prompted the investigation of an alternative navigator trajectory utilising a Lissajous–type trajectory for rigid–body motion correction. The k–space tra-

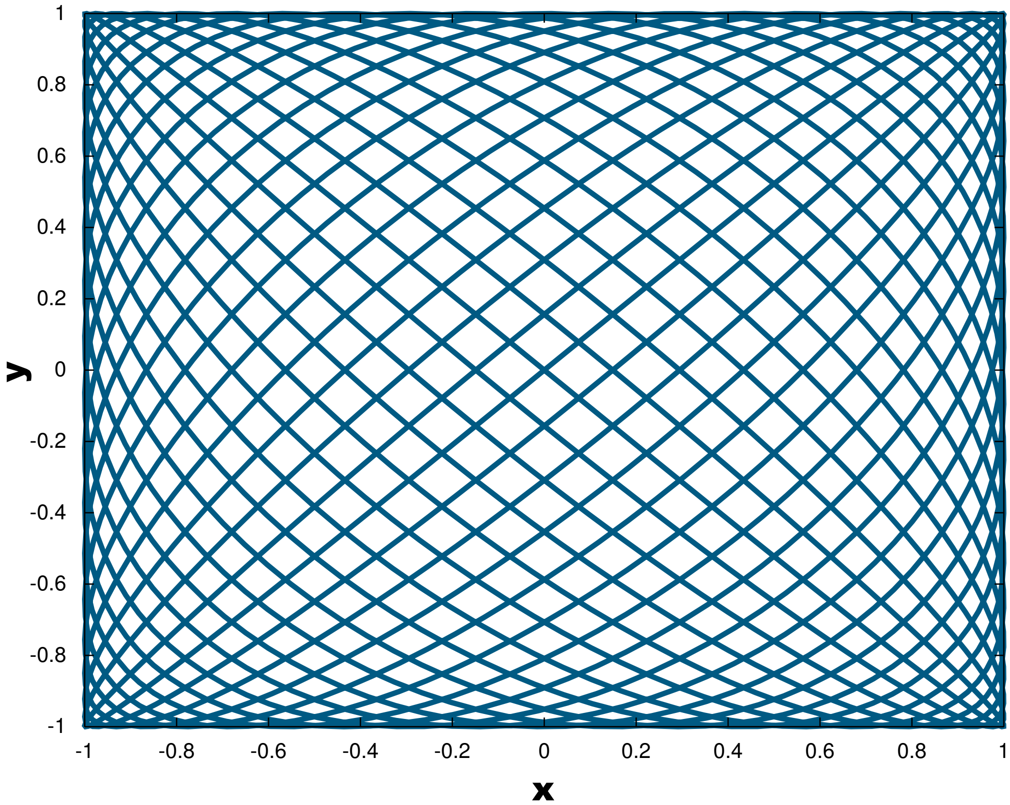

Figure 3.5: A conventional two–dimensional Lissajous figure with the parameters $A = B = 1$, $\alpha = 20$, $\beta = 21$ and $\phi = 0$.

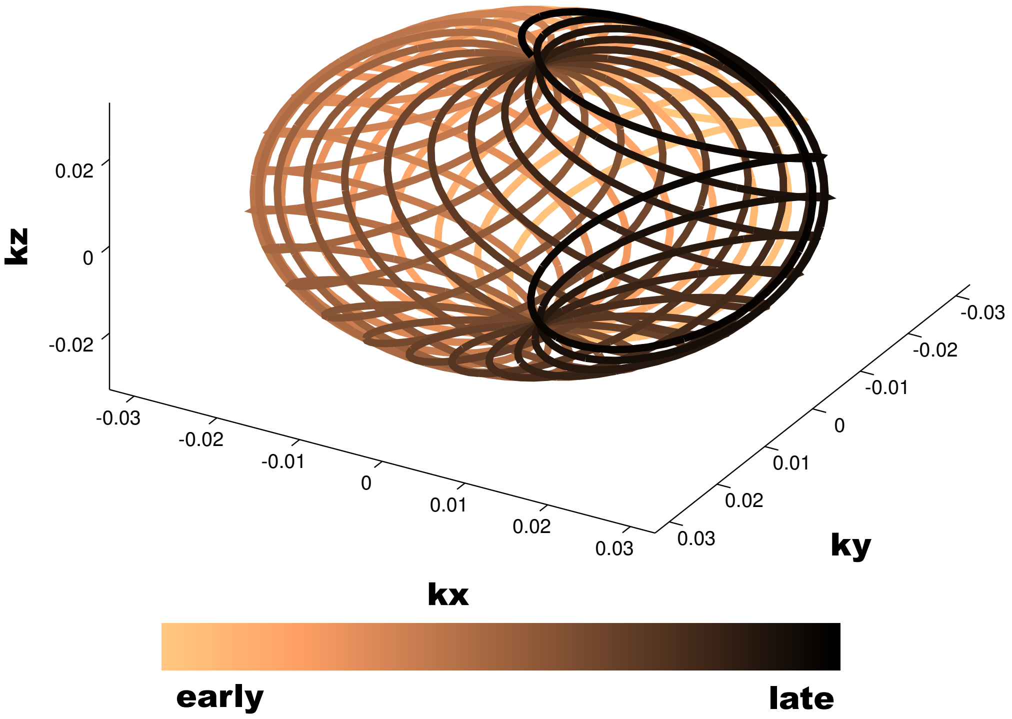

Figure 3.6: Plot of the Lissajous navigator trajectory. Yellow are early time points black are late sample points. The trajectory is a series of "figures of eights" projected onto the spherical surface, which rotate around the k_z–axis. Navigator parameters are $n_\Theta = 20$, $n_\Phi = 21$, $k_r = 0.03$.

jectory of the Lissajous navigator is given by the following formulae:

$$k_x = k_r \cdot sin(n_\Theta t) \cdot cos(n_\Phi t) \tag{3.12}$$

$$k_y = k_r \cdot sin(n_\Theta t) \cdot sin(n_\Phi t) \tag{3.13}$$

$$k_z = k_r \cdot cos(n_\Theta t), \tag{3.14}$$

where t ranges from $0 - 2\pi$ and n_Θ and n_Φ are rationale numbers and k_r is the k–space radius of the navigator. Figure 3.6 depicts the k–space trajectory and gradients of the Lissajous navigator for $n_\Theta = 20$,$n_\Phi = 21$ and $k_r = 0.03$. This trajectory has significant advantages for the application to navigated motion correction for

MRI. Its consistently moderate slewrate requirements increase rotation estimation accuracy and homogeneity as we shall see in later chapters.

Reduced Slew Rate Requirements

The Lissajous navigator trajectory has the advantage that the maximum slew rate is reached repeatedly during each sinusoidal period in the navigator. The spherical navigator on the other hand reaches its maximum slew rate towards the end of the acquisition, near the pole of the spherical shell, whilst at the equator the slew rate is much lower. A result of this non–optimal trait of the spherical navigator is that sampling of the whole sphere is not achievable within the hardware limits of the system. The Lissajous navigators repeating slew rate requirements over the whole acquisition, on the other hand, allow the sampling of the complete sphere while staying within the hardware limits of current scanners. Figure 3.7 shows the gradients and Figure 3.8 shows slew rates calculated for the Lissajous navigator in blue and for the spherical anvigator, with whole sphere coverage, in dashed red.

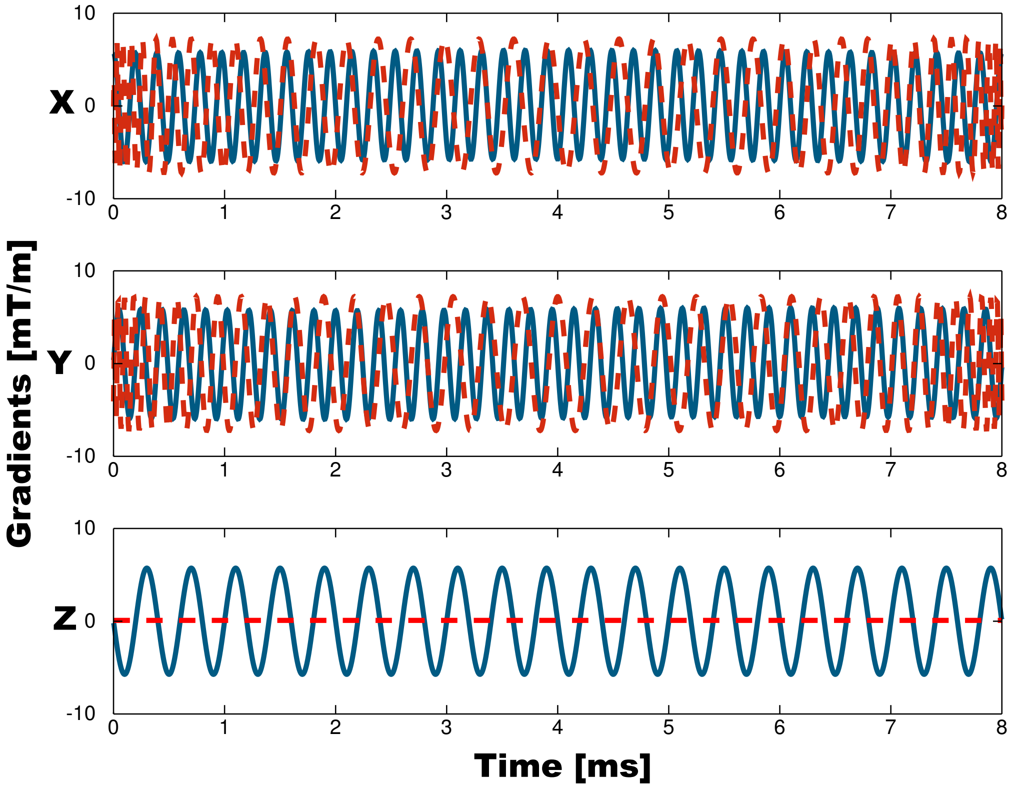

Figure 3.7: Gradients for the Lissajous navigator (blue solid line) and the spherical navigator (dashed red line) for whole sphere coverage. Both navigators are matched for k–space radius and acquisition time.

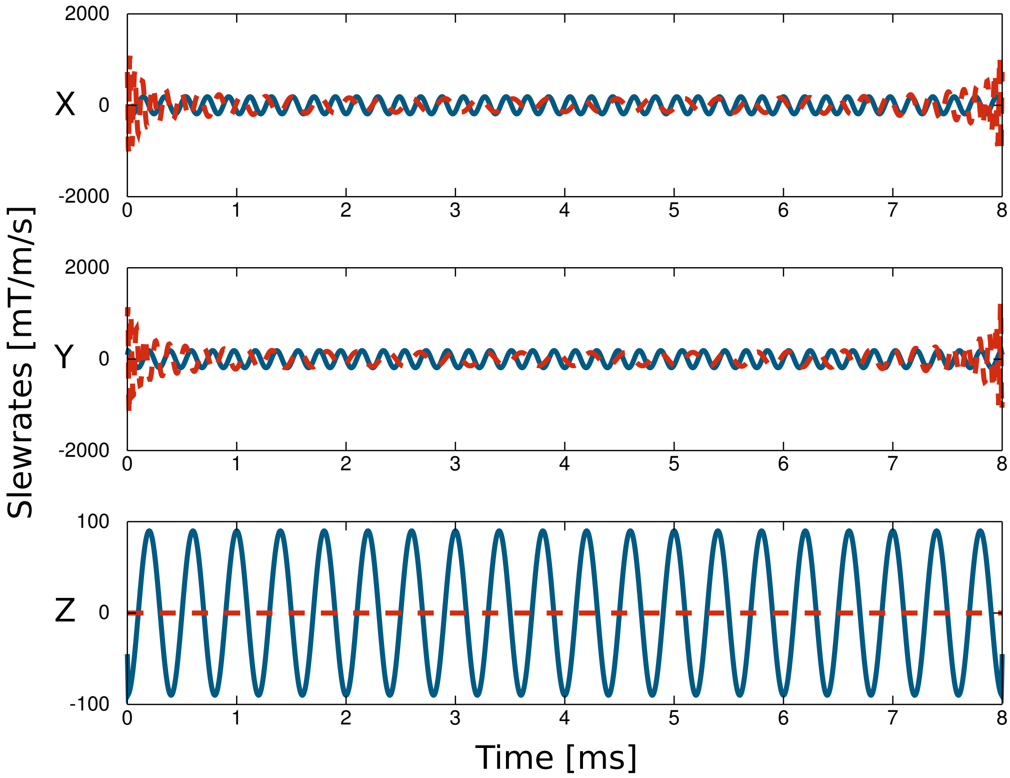

Figure 3.8: Slew rates for the Lissajous navigator (blue solid line) and the spherical navigator (dashed red line) for whole sphere coverage. Both navigators are matched for k–space radius and acquisition time.

4 DATA PROCESSING ALGORITHMS

This chapter describes the data processing algorithms used to analyse the simulated and measured navigator signals presented in this thesis.

4.1 Rotation Estimation

Rotations occurring between successive navigator acquisitions were estimated from the magnitude signal of the navigator by means of pattern matching on the spherical surface. All navigators of a scan or simulation were evaluated against a reference navigator. Usually the first simulated or measured navigator was chosen as a reference. Trial rotations were then applied to a subsequent navigator by interpolation. The sum of the squared differences for the magnitude signal for all sample points was minimised using a Nelder–Mead Simplex optimisation routine [46]. Rotations were represented using the three Euler angles (α, β, γ) in the notation described in the aeronautical norm DIN9300 [47]. Figure 4.1 shows a flow chart of the rotation estimation routine. All computations were performed directly on the

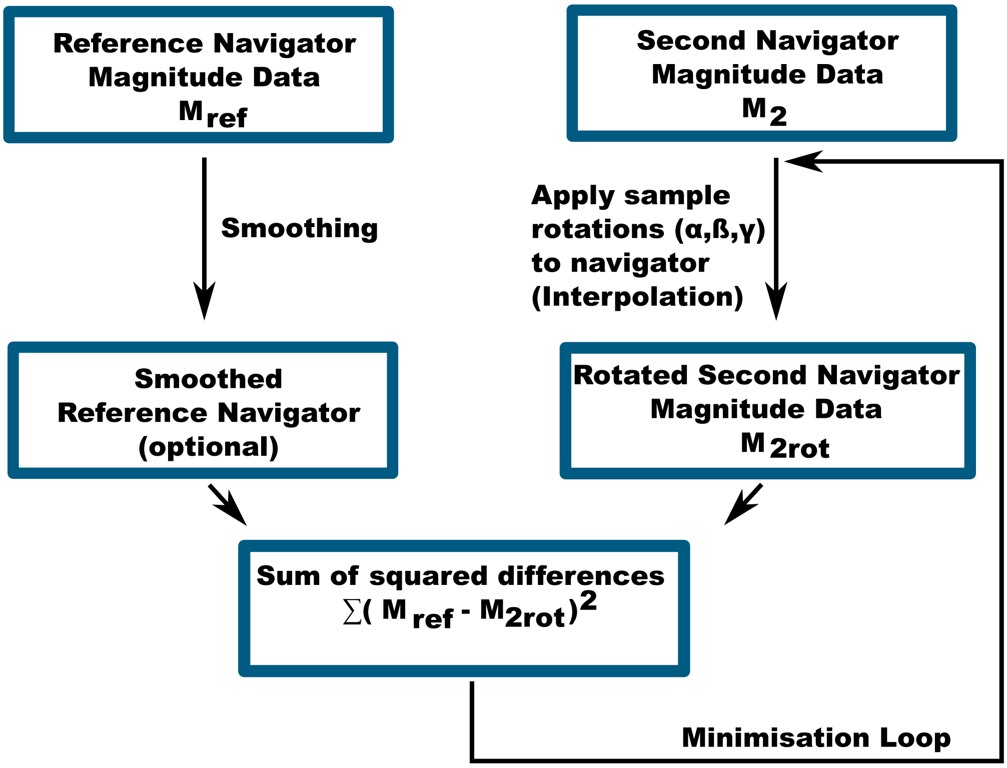
Reference Navigator Magnitude Data
M ref
Second Navigator Magnitude Data
M 2
Smoothing
Apply sample rotations (α,ß,γ) to navigator (Interpolation)
Smoothed Reference Navigator (optional)
Rotated Second Navigator Magnitude Data
M 2rot
Sum of squared differences
∑(M ref - M2rot)2
Minimisation Loop

Figure 4.1: Rotations are estimated by pattern-matching on the spherical surface. The magnitude data of the navigator is matched to a reference navigator by applying sample rotations to the data. The sum of squared differences is minimised using a Nelder-Mead Simplex optimisation routine [46]. For noise reduction a smoothing can also be applied to the reference navigator.

sampling grid of the reference navigator, rather than on an equally spaced latitude–longitude grid as in Reference [1], as performing the operations on the reference navigator grid showed higher accuracy. All computations were implemented using Matlab (The Mathworks Inc.).

4.1.1 Gridding on the Spherical Surface

To achieve a noise reduction in the navigator data, the required interpolation for the rotation estimation was performed using a gridding on the spherical surface with a Gaussian kernel. By utilising the spherical distance measurement the two–dimensional interpolation problem can be reduced to a one–dimensional problem. Following Bronsteins's spherical coordinate definition [48], with $0 \leq r < \infty$, $0 \leq \theta \leq \pi$, and $-\pi < \phi \leq \pi$ the shortest distance, d, between two points, p_1 and p_2, in radian is given by:

$$d = acos\{cos(\theta_{p1}) \cdot cos(\theta_{p2}) + sin(\theta_{p1}) \cdot cos(\phi_{p1} - \phi_{p2})\}. \tag{4.1}$$

Thus, gridding to the sampling points of the reference navigator can be achieved by carrying out the calculation in Eq. 4.2. The magnitude signal M_{interp} at point p_{interp} can be calculated from its n neighbouring points by calculating

$$M_{interp} = \frac{\sum_{i=1}^{n} \frac{1}{\sigma\sqrt{2\pi}} \cdot e^{-\frac{1}{2}(\frac{d_i}{\sigma})^2} \cdot M_i}{\sum_{i=1}^{n} \frac{1}{\sigma\sqrt{2\pi}} \cdot e^{-\frac{1}{2}(\frac{d_i}{\sigma})^2}}, \tag{4.2}$$

where d_i is the distance between p_{interp} and p_i, M_i is the signal at point p_i, and σ is the width of the Gaussian in radians.

4.2 T_2^* Correction Algorithm

Rapid T_2^* relaxation can lead to significant signal decay during the navigator acquisition. Thus, in case of motion between two navigator echoes, the signals cannot be exactly matched due to a different

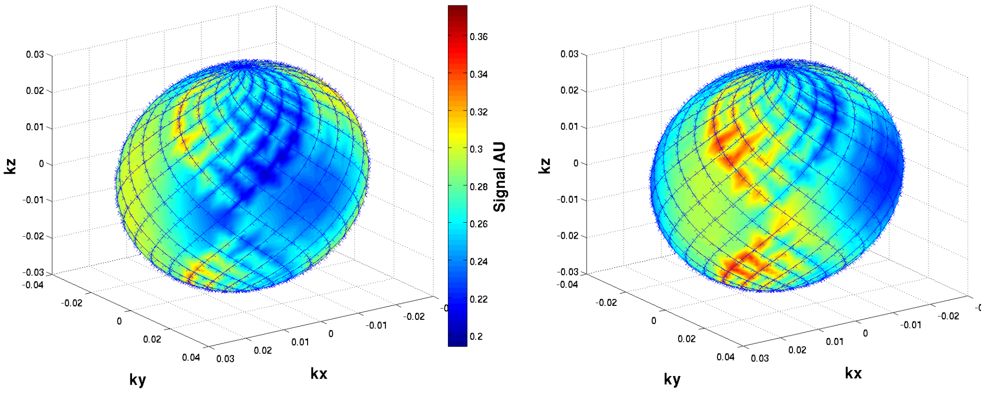

Figure 4.2: Influence of T_2^* decay on the navigator under the influence of motion. On the left, the magnitude of a simulated Lissajous navigator with decay constants appropriate for 1.5 Tesla. The same navigator acquisition rotated 35°around the z–axis. When rotation is present, the T_2^*–decay affects different features in the two navigators. This can cause errors in the pattern–matching algorithm since the two navigators are no longer identical objects.

temporal order of k–space feature acquisition. In Figure 4.2 the simulated magnitude signal of two Lissajous navigators is shown where one navigator is rotated by 35°. It is apparent from the figure that decay during the navigator acquisition modulates the measured magnitude pattern. When motion occurs between two navigator acquisitions, the decay affects different features of the magnitude pattern. This leads to a discrepancy between the navigator signals, which in turn can affect the rotation estimation. To reduce this source of error, a novel decay correction scheme was developed to enable correction of the decay. The crossing points in the Lissajous trajectory were utilised to calculate the decay during the acquisition and to correct its influence on the navigator signal without the necessity for additional data acquisition.

The algorithm performs the following steps:

1. The trajectory crossing points are identified.

   For every sampling point in the trajectory its closest neighbours are found. A plane pl_1 is defined which is the plane spanned by the current point, the next sampling point in time and the origin. Now a plane pl_2 is generated which is spanned by one of the close neighbours, and either its preceding or following point in time, as well as the origin. The intersection points of the two planes pl_1 and pl_2 are calculated. If one of the two intersection points is located inside of the square spanned by the four points on the spherical surface, a valid crossing point has been found. This procedure is repeated for each of the close neighbours of a sampling point and for all sampling points in the navigator.

   This step has to be performed only once for each navigator *trajectory*, not for every navigator measured.

2. Linear interpolation of the magnitude signals M_{t1} and M_{t2} directly onto the crossing point p_{cross}.

   At each crossing point, p_{cross}, the magnitude values (M_{t1}, M_{t2}) at two time–points (t_1, t_2) are calculated from the adjacent points p^a_{t1}, p^b_{t1}, p^c_{t2}, p^d_{t2} (see Figure 4.3 for definition of points).

3. Estimate the decay constant at the crossing point via a two–point exponential fit.

   Using the interpolated magnitude signals M_{t1}, and M_{t2} at the crossing point at acquisition times t_1 and t_2 an exponential model is used to fit a single exponential decay constant c:

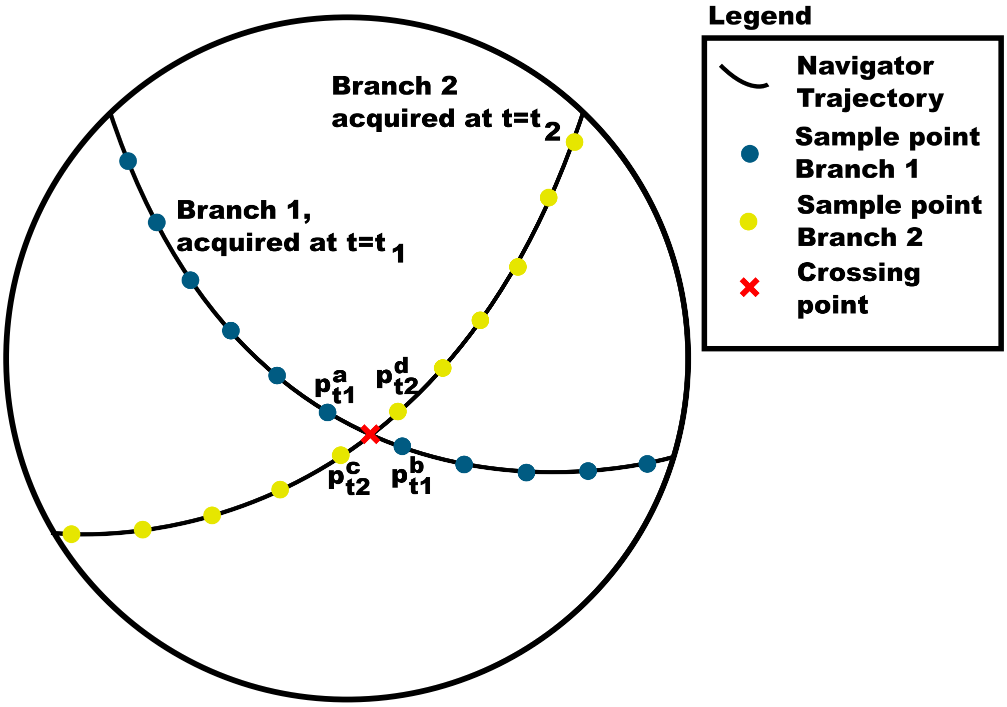
Legend
Navigator Trajectory
Sample point Branch 1
Sample point Branch 2
Crossing point
Branch 2 acquired at t=t2
Branch 1, acquired at t=t1
p a t1
p d t2
p c t2
p b t1

Figure 4.3: Crossing points in the Lissajous navigator. The magnitude values at the crossing point (red x) at times, t_1 and t_2, are calculated from the adjacent sampling points from Branch 1 (p^a_{t1}, p^b_{t1}) measured at time t_1 and Branch 2 (p^c_{t2}, p^d_{t2}) measured at time t_2 by linear interpolation.

$$M_{t1} = M_{t0} \cdot e^{c \cdot t_1} \tag{4.3}$$

$$M_{t2} = M_{t0} \cdot e^{c \cdot t_2} \rightarrow \tag{4.4}$$

$$c = \frac{ln(\frac{M_{t2}}{M_{t1}})}{t_2 - t_1} \tag{4.5}$$

where M_{t0} is the magnitude value at the crossing point p_{cross} immediately after the RF pulse ($t = t_0$).

4. Finally, the influence of the decay during the signal acquisition can be corrected by a global decay correction. The mean, c_{mean}, of all correction factors c in the navigator is calculated. All navigator magnitude values M_t^{uncorr} are then corrected for decay using this mean decay constant according to

$$M_t^{corr} = M_t^{uncorr} \cdot \frac{1}{e^{(c_{mean} \cdot t)}}, \tag{4.6}$$

where t is the acquisition time of the magnitude value which is being corrected, M_t^{uncorr} is the uncorrected magnitude sampled at time t after the RF pulse and M_t^{corr} is the corrected magnitude value.

It should be noted here that the correction model is of an empirical nature rather than being theoretically derived from the signal equation. The rationale for the correction is the assumption that in k–space the T_2^*–decay can be described with sufficient accuracy as a constant value.

The application of this algorithm is not limited to the Lissajous trajectory. All calculation steps can be performed on arbitrary sampling trajectories on the spherical surface. The only prerequisite is a trajectory which crosses itself.

4.3 Translation Estimation

Translation was estimated using the phase of the measured navigator signals on the spherical surface, with the algorithm outlined in [1] and described in the following paragraphs. The phase change $\Delta\phi$ caused by the translation $\Delta x, \Delta y, \Delta z$ at a k–space position (k_x, k_y, k_z) is given by:

$$\Delta\phi = 2\pi(\Delta x \cdot k_x + \Delta y \cdot k_y + \Delta z \cdot k_z). \tag{4.7}$$

For the n distributed sampling points of a navigator, this gives an overdetermined system of n equations with three unknowns. This system can be solved with a weighted least squares inversion. In matrix formulation the system can be written as

$$\mathbf{kx} = \mathbf{\Delta\Phi}, \tag{4.8}$$

where $\mathbf{k}$ is a nx3 matrix with the rows containing the k–space positions of the navigator sampling points (k_x,k_y,k_z), $\mathbf{\Delta\Phi}$ is an nx1 vector containing the phase differences $\Delta\Phi$ for each sampling point, and $\mathbf{x}$ is a 3x1 column vector consisting of the unknown translations Δx, Δy, Δz.

To introduce a weighting by the magnitude value of the sampling point, the system can be expanded to

$$(\mathbf{k^T W k})\mathbf{x} = \mathbf{k^T W \Delta\Phi}, \tag{4.9}$$

where **W** is a diagonal weighting matrix with the diagonal elements being the multiplied magnitude values of the reference navigator and the comparison navigator. Using

$$\mathbf{Q} = (\mathbf{k}^{\mathbf{T}}\mathbf{W}\mathbf{k}) \tag{4.10}$$

we can write this as

$$\mathbf{x} = \mathbf{Q}^{-1}\mathbf{k}^{\mathbf{T}}\mathbf{W}\boldsymbol{\Delta}\boldsymbol{\Phi}. \tag{4.11}$$

This algorithm is valid as long as no phase wraps occur, which means the phase change for each sample point has to be in the interval of $[-\pi, \pi]$. This holds true if the translations are smaller than $\frac{0.5}{k_{rad}}$, where k_{rad} is the k–space radius of the navigator. For larger translations the use of a phase–unwrapping algorithm is necessary.

5 QUANTITATIVE MOTION ESTIMATION THROUGH SIMULATIONS

Simulations are an important tool for the development of motion correction procedures for MRI because they offer an environment where each parameter can be controlled separately. This allows for the comparison of different navigator trajectories under the exact same conditions where a clear gold standard, the ground truth is known. This results in quantitative comparisons that are hardly possible without the tool of simulation. However, care must be taken to bring the model of the simulations in accordance with real–world experiments. Only when the simulation environment mimics the real world sufficiently can the insights gained with simulations be transferred to real–world scenarios.

5.1 *J*ülich *E*xtensible *MRI* *S*imulator — JEMRIS

All simulations presented here were performed with the numerical MRI simulator Jemris [49, 50, 51]. This simulator calculates the numerical solution of an MRI experiment in a classical model by solving the Bloch equation (Eq. 2.3) in the rotating frame for each spin individually. In order to generate the MR signal, integration of the signal equation (Eq. 2.6) is performed by summing up the signal of all the simulated spins.

Susceptibility effects were simulated by assigning an off–resonance to each spin calculated by the method described in [52].

Rigid body rotation was taken into account by rotating the gradient coordinate system for the simulation. Rigid body translation was achieved by shifting the simulated object by the desired amount.

5.2 Comparison of the Spherical Navigator and the Lissajous Navigator

To assess the theoretical performance of the Lissajous navigator and the spherical navigator [1] in the absence of noise, simulations were performed with both navigator trajectories.

5.2.1 Simulations & Analysis

The simulated navigator–only sequence consisted of a 90° RF pulse immediately followed by an $18ms$ three–dimensional navigator readout. The navigator trajectories were matched for k–space radius, maximum slew rate, acquisition time, and number of sampling points (N=2000). The reported pole cut–off of 15% [1] was used for the spherical navigator. The corresponding Lissajous navigator was simulated with $n_\theta = 20$ and $n_\phi = 21$ for maximum slew rate matching. To ensure a fair comparison, the spherical navigator trajectory was adapted to run from pole–to–pole with a single RF pulse.

The object used in the simulations was the MNI brain phantom [39], (see also Figure 3.2), with white matter and grey matter relaxation times appropriate for a 1.5 Tesla environment.

All simulations presented in this chapter were performed using a small–scale, high–performance computing cluster with up to 64 AMD Opteron CPUs running Linux.

Rotation

Multiple simulations were undertaken with induced rotations from 0° to 20° in steps of 1° around all three principal axes. Analysis was performed with the algorithms described in Section 4.1 implemented in Matlab.

Translation

For the translation estimation, multiple simulations with translations along the principal axes from $0m$ to $20mm$ along the three principal axes were calculated. Analysis was performed using the algorithm described in Section 4.3.

5.2.2 Accuracy of Rotation Estimation

The mean accuracy of rotation estimation for the spherical navigator was estimated to 0.45° with a maximum error of 3.0° at a rotation angle of 20°. For the Lissajous navigator, a mean absolute error of 0.22° was achieved with a maximum error of 1.0° at a rotation of 14° around the y–axis. Figure 5.1 depicts the absolute rotation estimation error as a function of rotation angle for the spherical and Lissajous navigator for all three principal axes. Figures 5.2 - 5.4 depict the absolute estimation errors on the off–rotation axes. For the spherical navigator the error increases steadily with rotation for both on– and off–rotation axes. The Lissajous navigator exhibits a more complex error structure were the error increases with rotation–angle until it reaches a maximum and decreases again at larger rotations. As we will see in later chapters, this error structure is characteristic for the Lissajous navigator and will be discussed in more detail in Section 7.8.

5.2.3 Accuracy of Translation Estimation

Figures 5.5 and 5.6 show the accuracy of translation estimation as a function of translation distance for both the spherical and the Lissajous navigator at k–space radii of $0.03\frac{1}{mm}$ and $0.07\frac{1}{mm}$. At a radius of $0.03\frac{1}{mm}$ the achieved accuracy of translation estimation performs

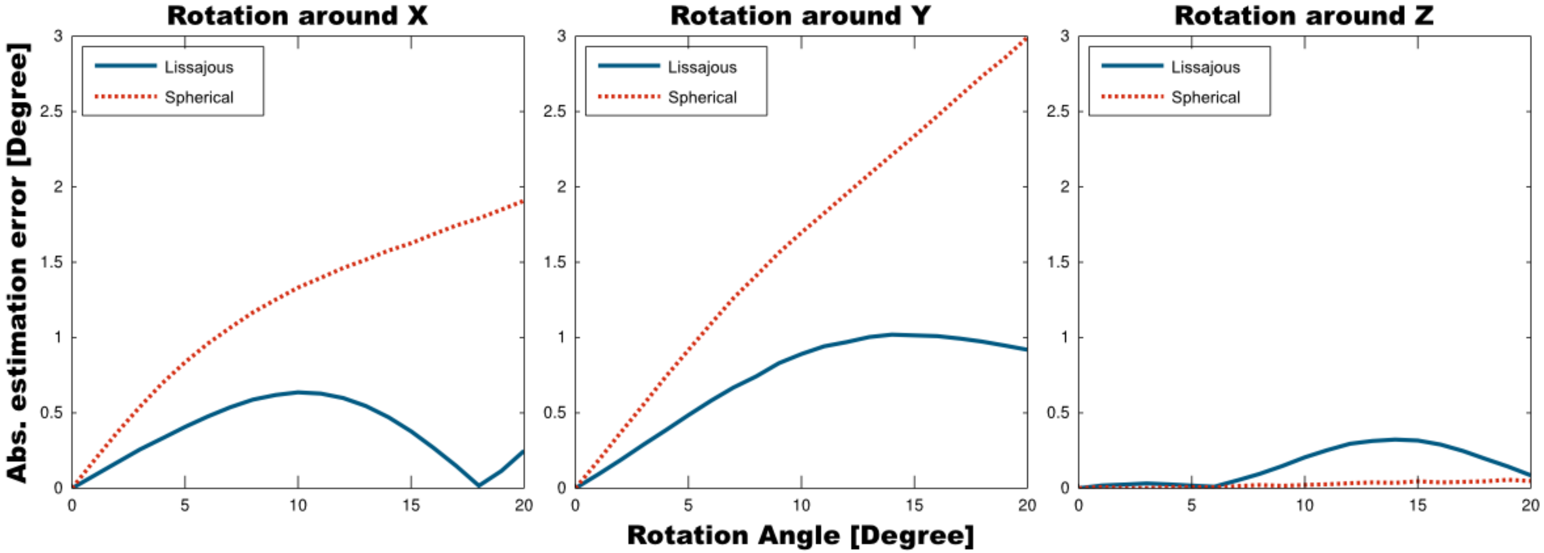

Figure 5.1: Absolute error of the rotation estimates on the axis of rotation for the spherical navigator (red, dotted), Lissajous navigator (blue, solid).

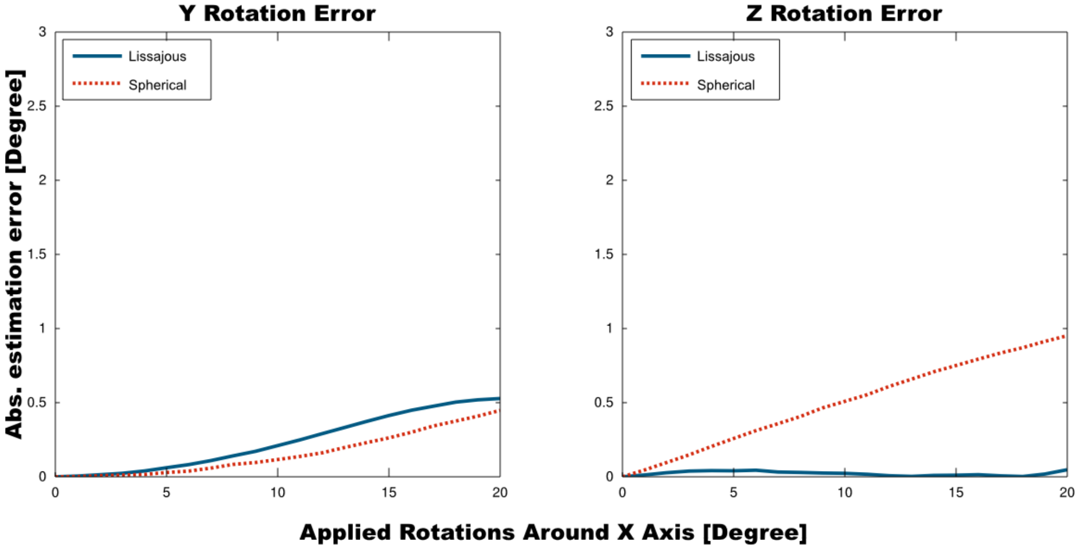

Figure 5.2: Absolute rotation estimate errors on the off–rotation axes for rotations around x.

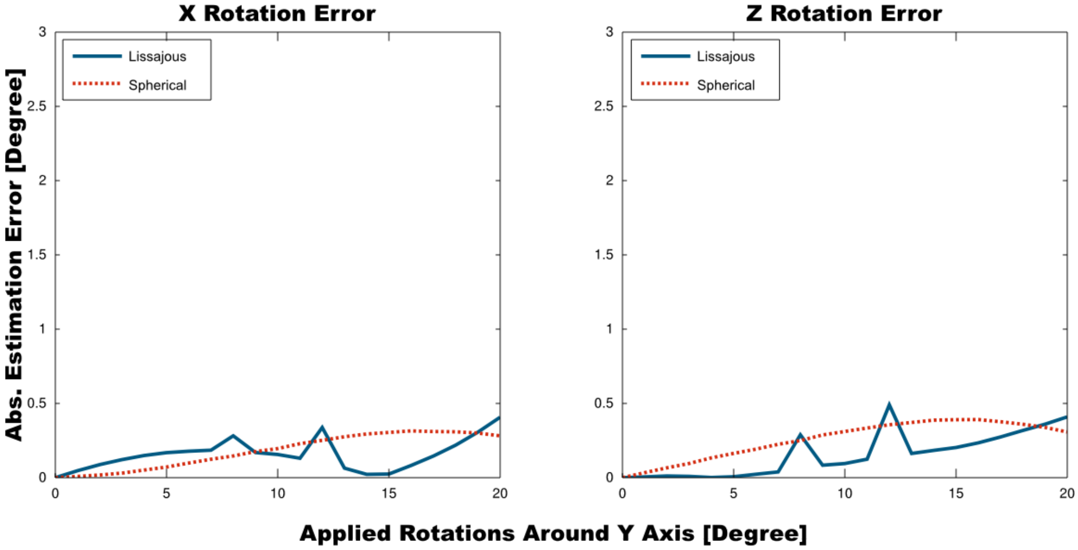

Figure 5.3: Absolute rotation estimate errors on the off–rotation axes for rotations around y.

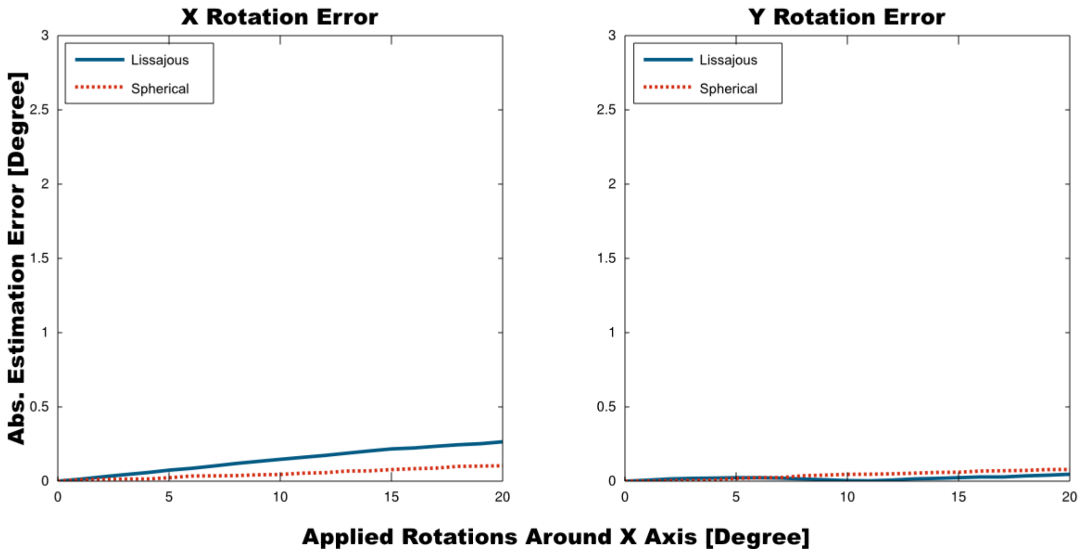

Figure 5.4: Absolute rotation estimate errors on the off–rotation axes for rotations around z.

reliably for both navigators with a mean translation estimation error of $0.0008mm$ for the spherical navigator and $0.0004mm$ for the Lissajous navigator. However, at a k–space radius of $0.07\frac{1}{mm}$ — the optimal radius for rotation estimation (see Table 5.1) — both navigators suffer from large errors in the translation estimates due to phase wrapping. The mean absolute translation errors are $6.2mm$ and $6.7mm$ for the spherical and Lissajous navigator, respectively.

5.3 Influence of Susceptibility, Signal Decay and Chemical Shift on the Rotation Estimation

In Table 5.1 the influence of susceptibility, relaxation decay and chemical shift of fat on the accuracy of rotation estimation are given

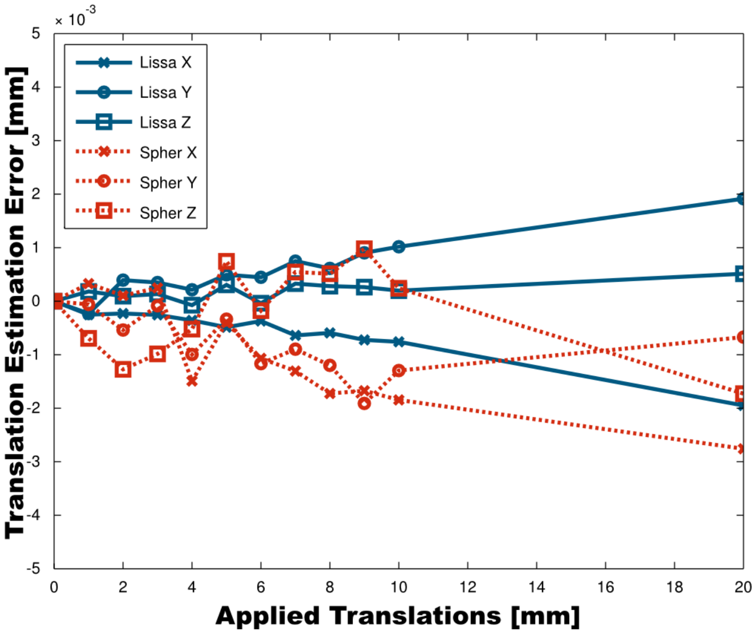

Figure 5.5: Translation estimation error as a function of translation for all three principal axes for the spherical (red, dotted) and Lissajous navigator (blue, solid) for a navigator k–space radius of $0.03\frac{1}{mm}$.

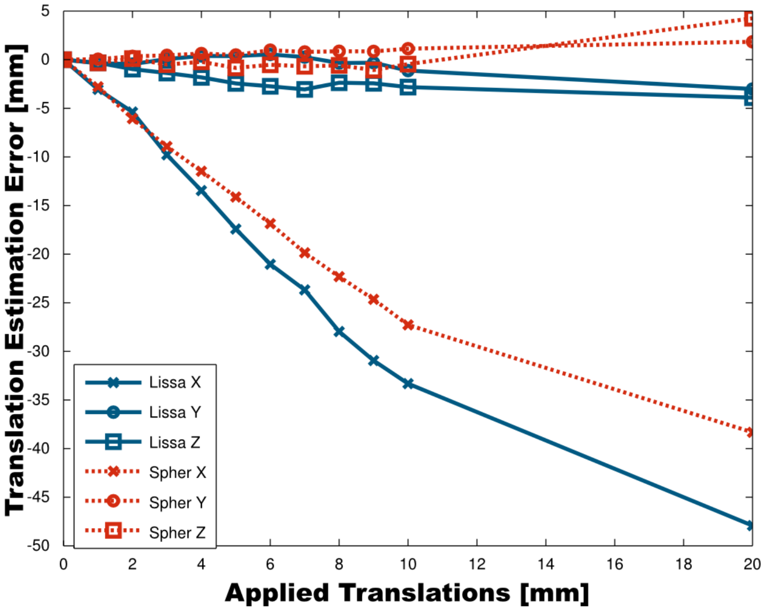

Figure 5.6: Translation estimation error as a function of translation for all three principal axes for the spherical (red, dotted) and Lissajous navigator (blue, solid) for a navigator k–space radius of $0.07\frac{1}{mm}$

as a function of the k–space radius of the navigator. *Ideal* indicates an ideal navigator where the relaxation times T_1 and T_2 were set to infinity (without relaxation) and no susceptibility–induced off–resonances were taken into account. *Susceptibility* denotes a navigator where T_1 and T_2 were set to infinity, but susceptibility induced off–resonances were included. *Decay* specifies a navigator where the relaxation times T_1 and T_2 were values appropriate for a 1.5 Tesla environment without accounting for susceptibility effects. All values in the row *Chemical Shift (CS)* were obtained with navigators simulated without relaxation and susceptibility effects but with an off–resonance associated to all spins belonging to fat. The rows *Decay + Susceptibility* and *Decay + CS + Susceptibility* are simultaneous contributions of the effects.

The optimal radius for the accuracy of the rotation estimation is found at a radius of $0.07\frac{1}{mm}$. Further, susceptibility effects have the largest influence on the accuracy of the navigator. The influence of susceptibility effects decreases with growing radius. However, even at large radii, susceptibility–induced field inhomogeneities remain the dominant effect limiting the accuracy of rotation estimation. Different tissue susceptibilities lead to inhomogeneities in the static magnetic field. Thus, these effects are apparent at all k–space radii. Signal decay, on the other hand, leads to a larger error at very small k–space radii, while the influence of the effect rapidly decreases towards larger k–space radii. One explanation for the large influence of decay on the navigator signal near the k–space centre is the nature of the decay. Specifically, signal decay occurs in all tissues and it decays with different decay constants depending on the tissue, but some amount of decay is present in each volume element. Thus, in k–space a large part of the decay is represented near the low, central spatial frequencies, where large contrast features of the image are encoded.

Some of these error sources cancel each other out. Thus, the combined error in the simulation with the highest real–world applicability — those with susceptibility effects, signal decay and chemical shift — do exhibit results better than one would expect from looking at the simulations where each of the effects has been considered separately.

5.4 Influence of Noise on the Accuracy of Rotation Estimation

In order to investigate the influence of noise on the accuracy on the rotation estimation of the Lissajous navigator, noise was added to the navigators simulated with susceptibility, decay and chemical shift with a radius of $k_{rad} = 0.07\frac{1}{mm}$. Gaussian noise was added to real and imaginary part of the navigator before rotation estimation. The signal–to–noise ratio (SNR) of the navigator was calculated as the signal magnitude in the centre of k-space at the time immediately after the RF pulse divided by the standard deviation of the Gaussian distribution. Please note this is a more rigorous definition of SNR than commonly used in imaging. In imaging, usually the mean signal level in the imaged object is used in the numerator. Approximated, this would be the equivalent of the signal magnitude in the centre of k-space at the *echo time*, not at the time immediately

Radius $[\frac{1}{mm}]$	Ideal	Susceptibility	Decay	Chemical Shift (CS)	Decay + Susceptibility	Decay + CS + Susceptibility
0.02	0.04	2.26	2.53	0.8	2.83	2.85
0.03	0.04	1.55	0.81	0.18	0.87	1.78
0.04	0.09	1.19	0.15	0.12	0.15	0.93
0.05	0.18	0.85	0.30	0.44	0.58	0.86
0.06	0.12	0.41	0.27	0.29	0.52	0.93
0.07	0.10	0.37	0.16	0.16	0.21	0.22
0.08	0.25	0.44	0.29	0.21	0.29	0.49

Table 5.1: Influence of susceptibility, decay and chemical shift (fat), on the accuracy of the rotation estimation of the navigator. All values are the mean absolute error in degree for rotations in the range of $[0°, 20°]$.

SNR	Spherical Navigator	Lissajous Navigator
100	$0.5° \pm 0.4°$	$0.2° \pm 0.4°$
200	$0.5° \pm 0.2°$	$0.2° \pm 0.2°$
300	$0.5° \pm 0.1°$	$0.2° \pm 0.1°$

Table 5.2: Mean absolute error and mean standard deviation of the errors for the spherical navigator and the Lissajous navigator for different signal-to-noise ratios. The influence of noise on the precision two navigators is similar, however the Lissajous navigator remains more accurate due to its lower systematic error.

after the excitation pulse. However, since the navigator itself does not have an echo time, this more rigorous definition seems appropriate. Simulations were carried out for an SNR of 100, 200 and 300 for rotations from 0° to 20° around all principal axes. Sixty simulations were performed per rotation angle. Both the spherical and the Lissajous navigator show identical mean standard deviations and thus similar influence for all three tested SNR (see Table 5.2). However, the Lissajous navigator retains its lower systematic error and thus outperforms the spherical navigator. Detailed error curves are shown in Figures 5.7-5.10.

5.5 *A*dvanced *Li*ssajous Navi*ga*tor with T_2^* Co*r*rection (ALIGAT2R)

As seen in Section 5.3, signal decay is one dominant factor influencing the accuracy of the navigator. To counteract this influence and regain some of the accuracy lost due to the signal decay, the T_2^*–correction algorithm described in Section 4.2 was developed and implemented.

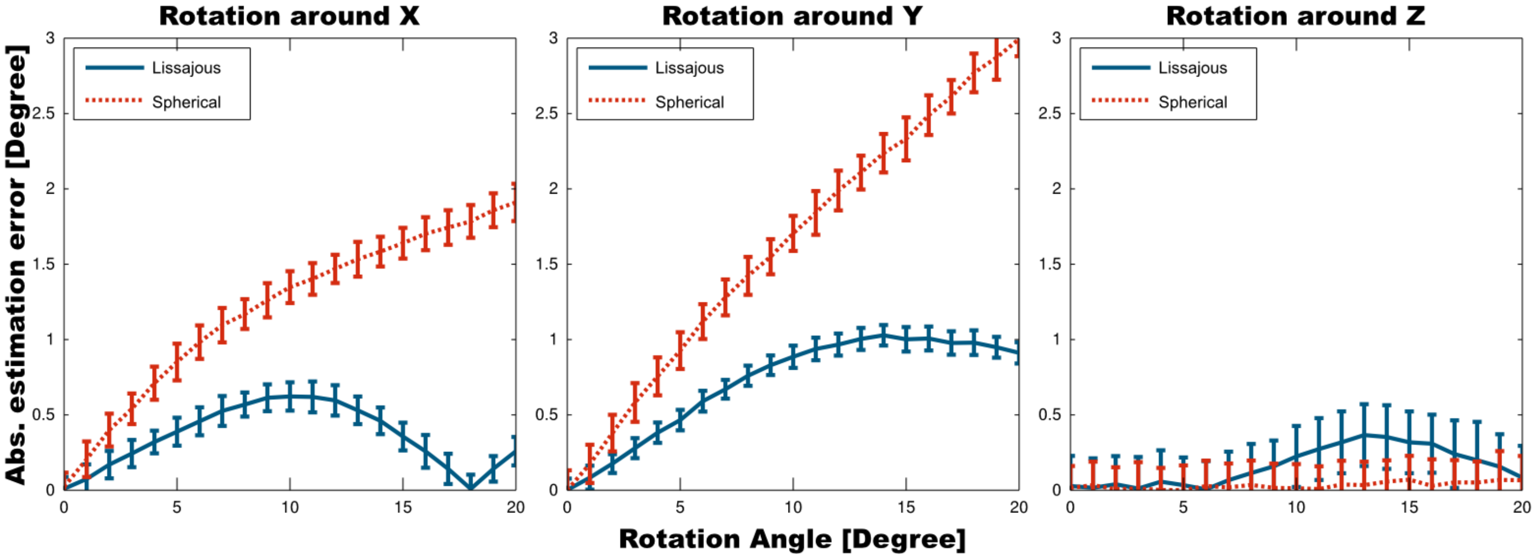

Figure 5.7: Absolute error of the rotation estimates on the axis of rotation for the spherical navigator (red, dotted), Lissajous navigator (blue, solid) with SNR = 300.

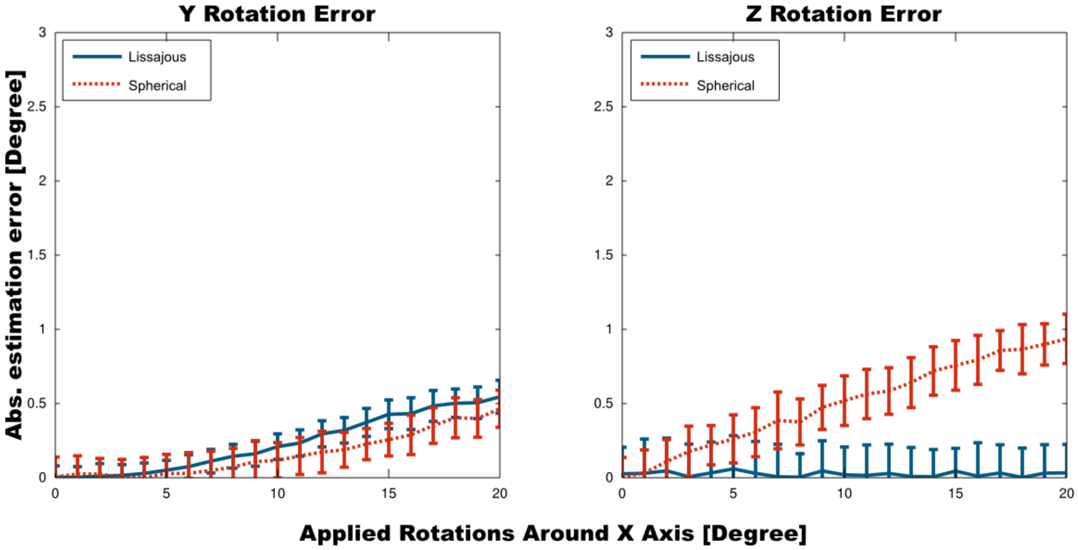

Figure 5.8: Absolute error of the rotation estimates on the off–rotation axes for rotations around x with SNR = 300.

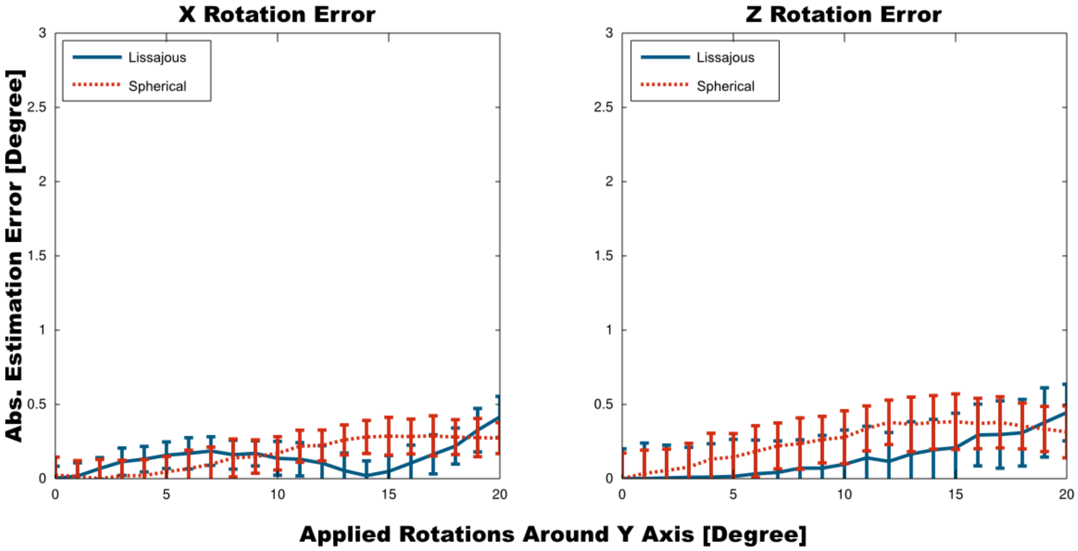

Figure 5.9: Absolute error of the rotation estimates on the off–rotation axes for rotations around y with SNR = 300.

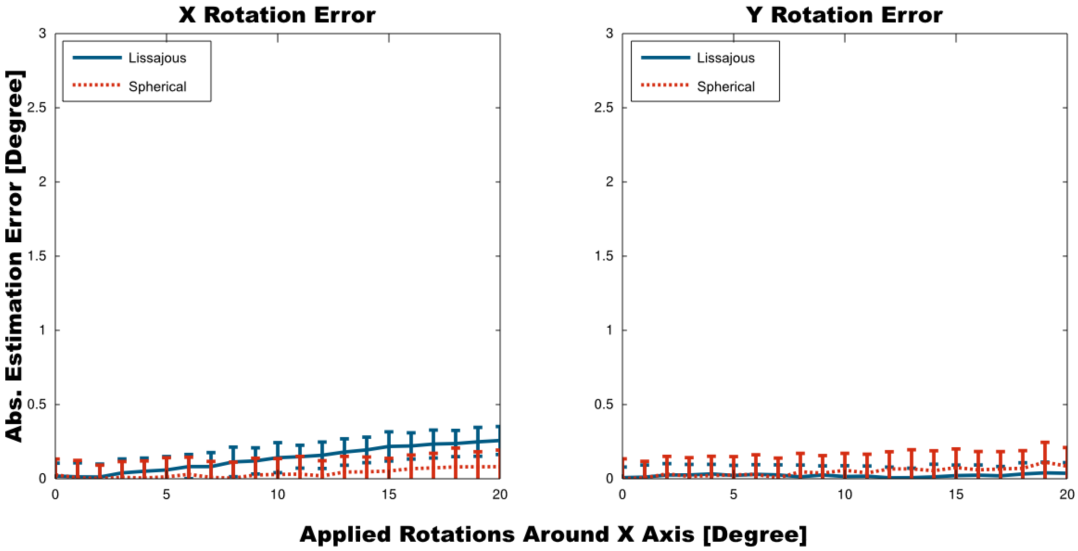

Figure 5.10: Absolute errors of the rotation estimates on the off–rotation axes for rotations around z with SNR $=$ 300.

5.5.1 Simulations & Analysis

Testing the ability of the algorithm to correct signal decay that has occurred is difficult on measured data. Measured data necessarily includes decay. Hence simulations provide a gold standard where we have control over the decay mechanisms and can perform two simulations: one with a set of relaxation times appropriate for a 1.5 Tesla system and one ideal simulation with decay times set to infinity. Thus, ideal, non-relaxed data can be obtained. With these data, the ideal navigator magnitude signal was compared to the corrected navigator magnitude signal and the performance of the correction algorithm was evaluated.

k–space Radius Optimisation

In order to find the optimal k–space radius for the T_2^*–correction algorithm, the correction procedure was performed on a single navigator at each simulated k–space radius. This navigator was then point–wise compared to an ideal navigator without the influences of decay, susceptibility and chemical shift. The radius where the sum of squared differences between the ideal navigator and the corrected navigator (normalised to the mean magnitude value of the ideal navigator) was minimal was identified and used for the subsequent rotation estimation analysis.

Rotation Estimation Evaluation

At this radius, rotation estimation experiments were performed with navigators rotated around the three principal axes from 0° to 20° in steps of 1°. Noise was added to the navigators (SNR=300) as described in the previous section and rotation estimation and decay correction was performed as described in Chapter 4. Thirty repetitions were performed for each rotation angle. The procedure was performed once, for the navigators simulated including the effects of decay and chemical shift, and once for the navigators simulated with decay, chemical shift and susceptibility effects.

5.5.2 Results

The k–space radius at which the correction algorithm performs optimally was found to be $0.03\frac{1}{mm}$. At larger k–space radii the sum of

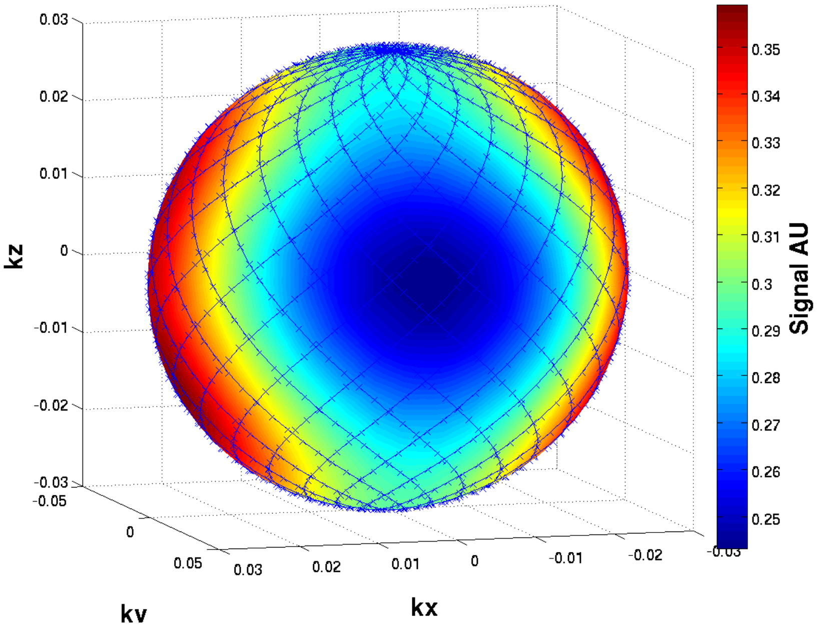

Figure 5.11: Ideal navigator without T_2^*–decay and without chemical shift.

squared differences between ideal and corrected navigator increased. This radius is, of course, object dependent, or more specifically dependent on the relaxation times and their distribution in the object. The optimal radius for the decay correction algorithm is significantly smaller than the optimal radius for rotation estimation when no decay correction algorithm is used (see Section 5.3).

In Figure 5.11 the magnitude pattern of an ideal navigator without the influence of decay at the optimal radius $0.03\frac{1}{mm}$ is plotted. The corresponding simulation with decay constants appropriate for 1.5 Tesla is plotted in Figure 5.12. Decay artefacts are clearly visible in the area where early threads are crossed by late threads. These artefacts are reduced in Figure 5.13, which shows the navigator from Figure 5.12 with additional T_2^*–decay correction. The correction al-

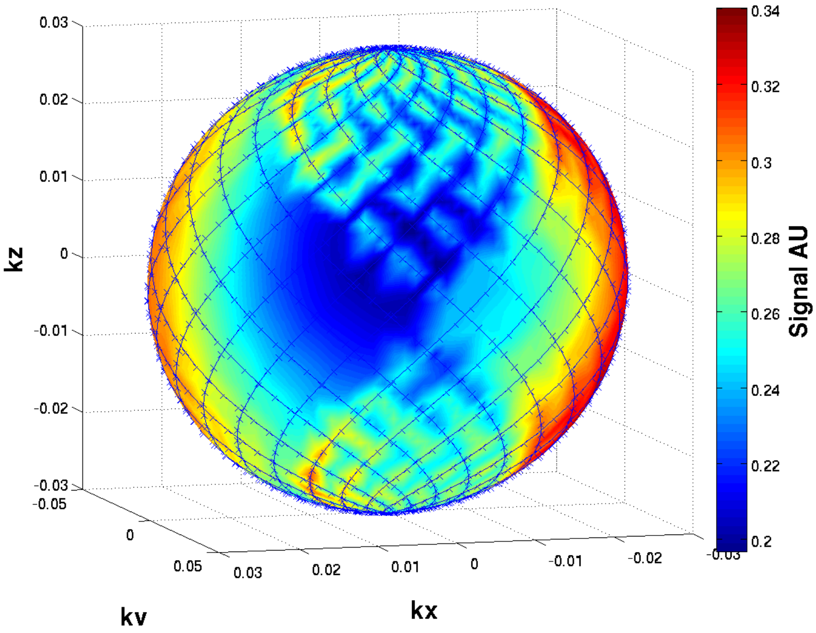

Figure 5.12: Uncorrected navigator with relaxation artefacts.

gorithm achieved a reduction of the difference between corrected and ideal navigator from 11.1% (uncorrected) to 3.6% (corrected).

A rotated comparison navigator can be transformed back to the reference navigator position by applying the inverse of the true applied rotation. The difference between this reverse transformed navigator and the reference navigator indicates how well the true rotation can be recovered. The smaller this difference is, the better the optimisation will be. Ideally, the difference would be zero at every point of the navigator. The absolute difference for a rotation of 9° around the y–axis is plotted in Figure 5.14 for the uncorrected navigator and in Figure 5.15 for the corrected case. In the corrected case, the difference is lower.

Figures 5.16-5.19 show the absolute error of the rotation around

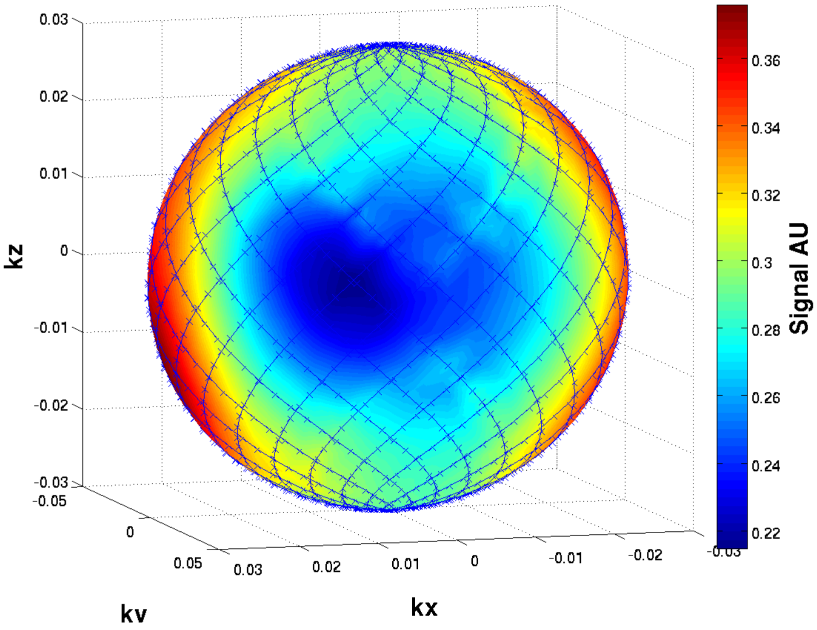

Figure 5.13: T_2^*–decay corrected navigator.

the x–, y–, and z–axes as a function of rotation angle for the navigators with decay and chemical shift effects only. On all three axes, the correction technique significantly reduces the error of the rotation estimation. For all three rotation axes combined, the mean absolute error of the rotation estimation is 0.9° for the uncorrected navigator and 0.3° for the corrected navigator.

A depiction of the absolute error of the rotation estimates for navigators including susceptibility effects, in addition to decay and chemical shift, can be found in Figures 5.20-5.23. Here, for all three rotation axes combined, the mean absolute error of the rotation estimation is 1.8° for the uncorrected navigator and 1.9° for the corrected navigator.

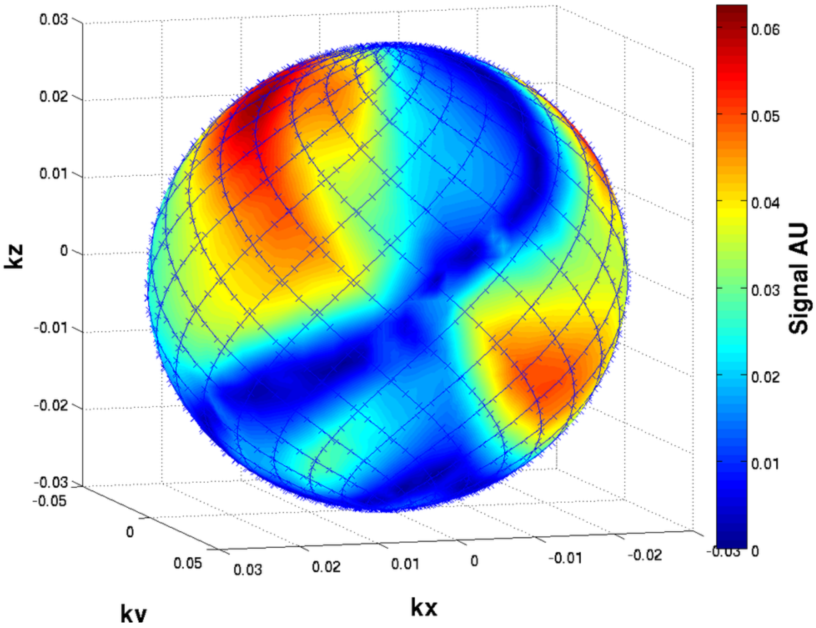

Figure 5.14: This absolute difference between the reference navigator and a rotated (9° around y–axis) navigator interpolated back to the reference position. Reference and rotated navigator are uncorrected.

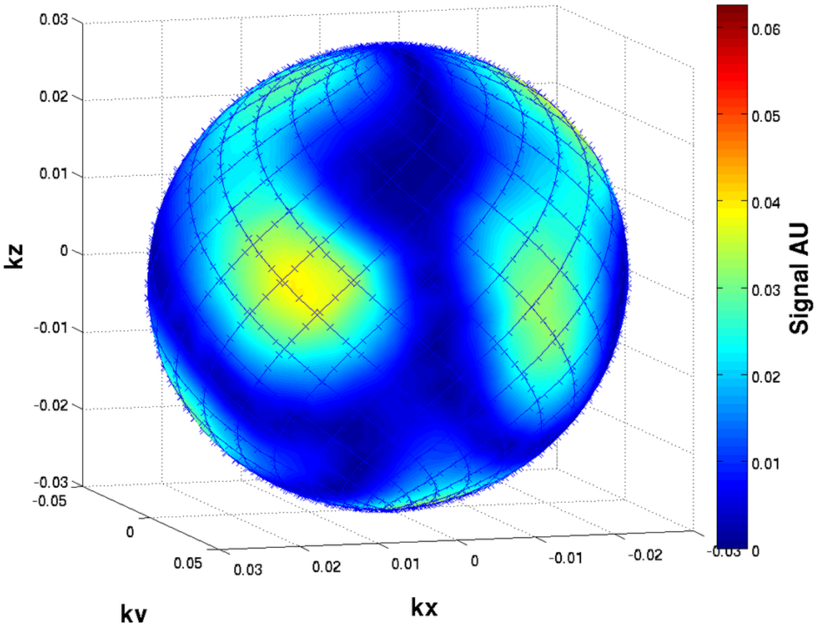

Figure 5.15: The absolute difference between the reference navigator and a rotated (9° around y–axis) navigator interpolated back to the reference position. Reference and rotated navigator are decay corrected.

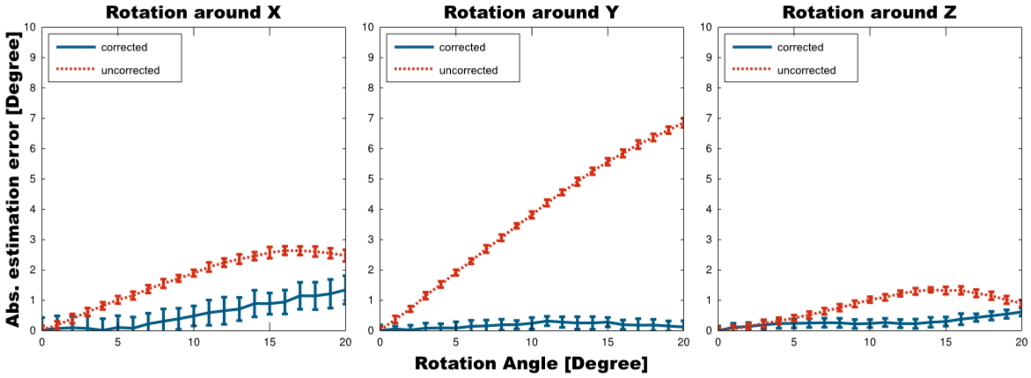

Figure 5.16: Absolute error of the rotation estimates on the axis of rotation for the uncorrected navigator (red, dotted), and the corrected navigator (blue, solid) with SNR = 300.

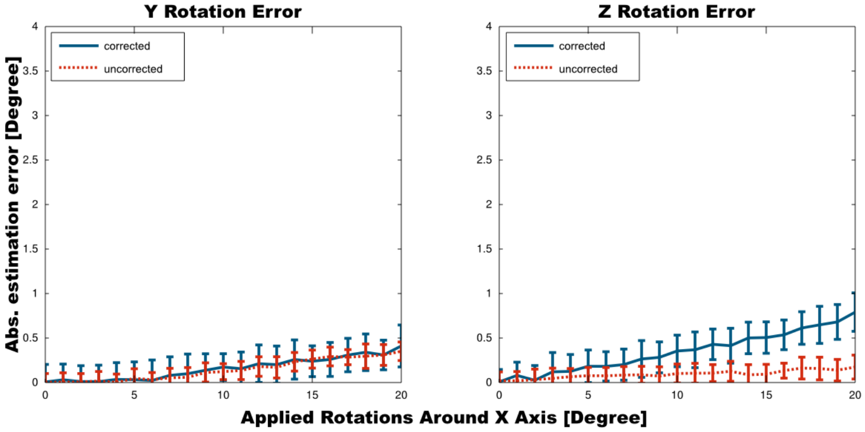

Figure 5.17: Absolute error of the rotation estimates on the off–rotation axes for rotations around x for the uncorrected navigator (red, dotted), and the corrected navigator (blue, solid) with SNR = 300.

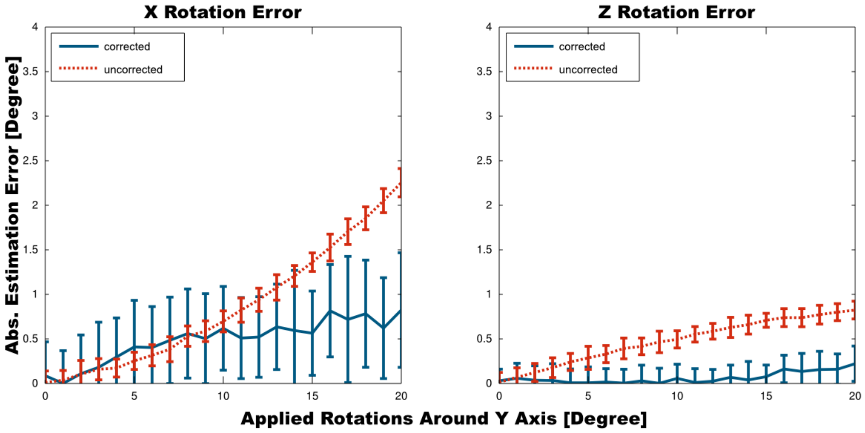

Figure 5.18: Absolute error of the rotation estimates on the off–rotation axes for rotations around y for the uncorrected navigator (red, dotted), and the corrected navigator (blue, solid) with SNR = 300.

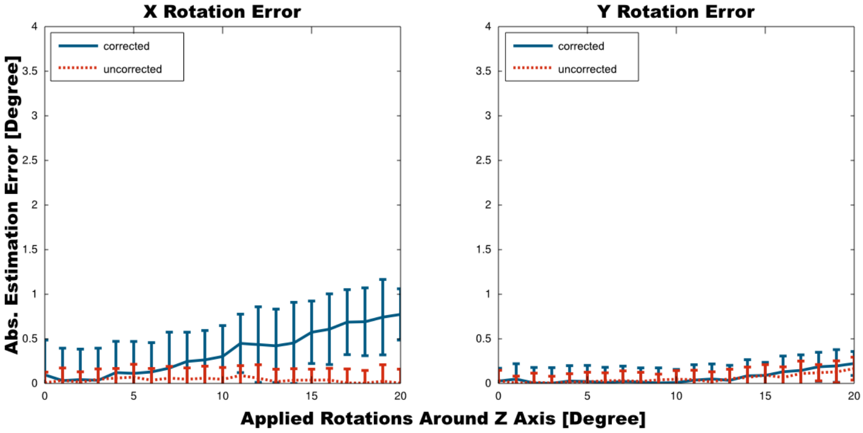

Figure 5.19: Absolute error of the rotation estimates on the off–rotation axes for rotations around z for the uncorrected navigator (red, dotted), and the corrected navigator (blue, solid) with SNR = 300.

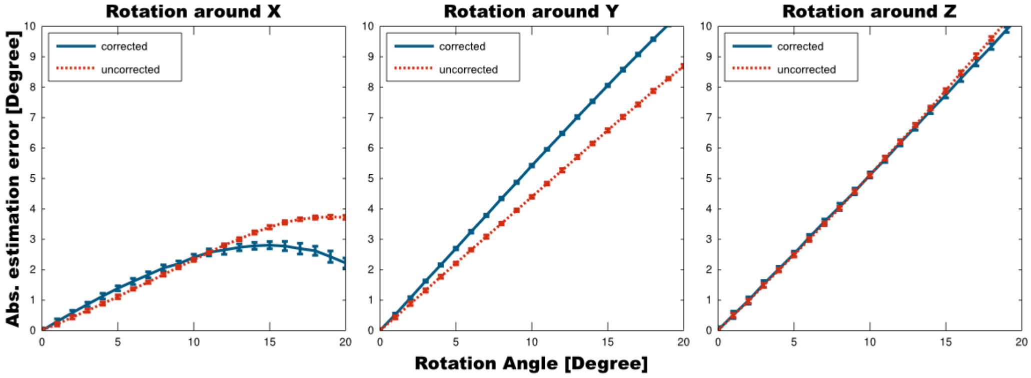

Figure 5.20: Absolute error of the rotation estimates on the axis of rotation for the uncorrected navigator (red, dotted), and the corrected navigator (blue, solid) with SNR = 300 simulated with decay, chemical shift, and susceptibility effects.

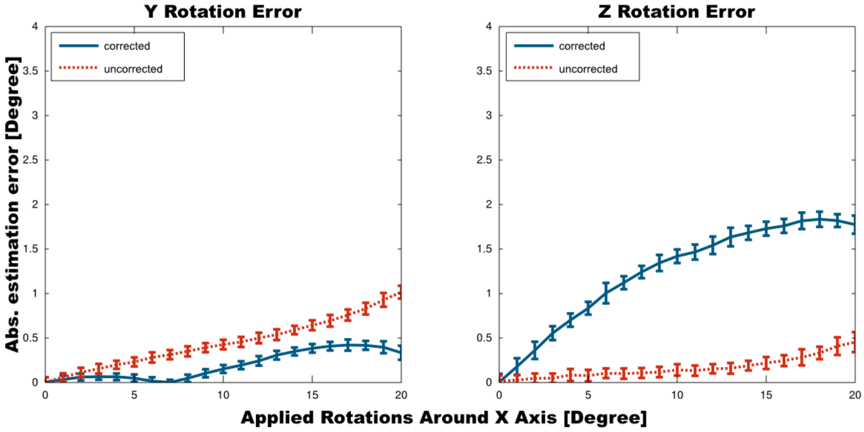

Figure 5.21: Absolute error of the rotation estimates on the off–rotation axes for rotations around x for the uncorrected navigator (red, dotted), and the corrected navigator (blue, solid) with SNR = 300 simulated with decay, chemical shift, and susceptibility effects.

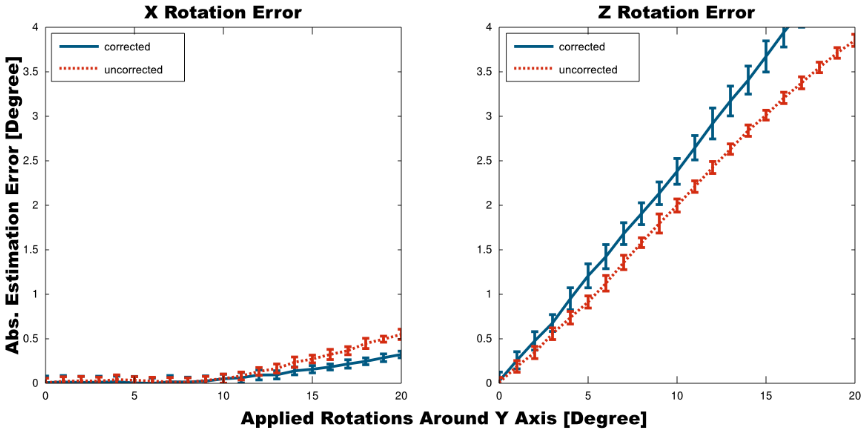

Figure 5.22: Absolute error of the rotation estimates on the off–rotation axes for rotations around y for the uncorrected navigator (red, dotted), and the corrected navigator (blue, solid) with SNR = 300 simulated with decay, chemical shift, and susceptibility effects.

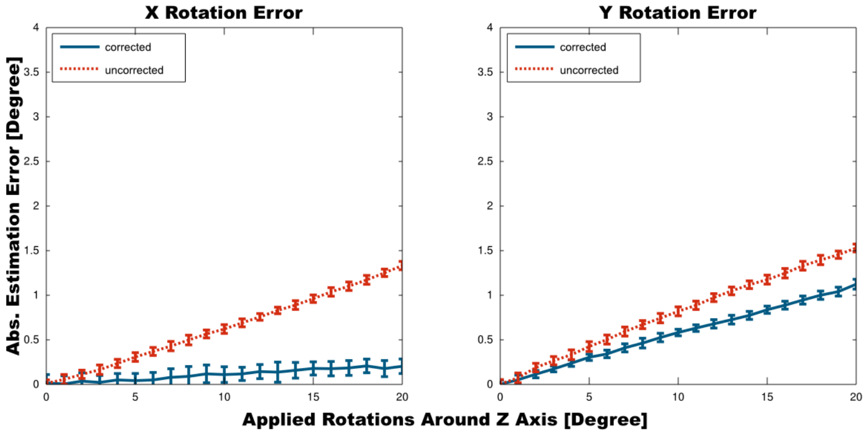

Figure 5.23: Absolute error of the rotation estimates on the off–rotation axes for rotations around z for the uncorrected navigator (red, dotted), and the corrected navigator (blue, solid) with SNR = 300 simulated with decay, chemical shift, and susceptibility effects.

5.5.3 Discussion

The proposed T_2^* auto–correction technique for the Lissajous navigator successfully compensates large amounts of the signal decay throughout the acquisition time in the absence of field inhomogeneities. Our simulations show that the method increases the accuracy of rotation detection by up to 68% relative to the uncorrected navigators.

These results are achieved at a k–space radius where the correction algorithm performed optimally; the results may vary at different k–space radii. However, the results reveal that using the developed T_2^*–correction algorithm does improve the accuracy of rotation estimation in homogeneous fields. The achievable improvement in the magnitude data of the navigator is largest at small k–space radii. Here, reasonable accuracy of the rotation estimation cannot be achieved without the use of the decay correction algorithm.

The k–space radius dependency of the correction algorithm, as shown by the radius optimisation, is likely to be a result of the empirical nature of the model, which is not rooted in a derivation from the signal equation. The simulation results suggest that the model only holds true at small k–space radii. While measuring at the low k–space radius does not give the overall best performance of the rotation estimation, it does open the possibility for further improvements. At lower k–space radii, an increased number of threads can be sampled in the same acquisition time which improves the radial resolution and in turn is likely to increase the rotation estimation further. This will be subject of further investigation. Translation estimation also benefits from the decreased k–space radius because the range of the translation estimate is limited by phase wraps occurring at translations larger than $\frac{0.5}{k_{rad}}$ (see Section 4.3). Thus, a smaller k–space radius, k_{rad}, increases the tracking range over which translational motion can be tracked. However, the correction procedure is very sensitive to B_0 field inhomogeneities. When B_0 modulations caused by susceptibility are included in the simulation, the correction results in a 7% loss of accuracy of the rotation estimation compared to the uncorrected navigator. The B_0 inhomogeneities modulate the decay and it deviates from an exponential pattern. Thus, when this modulation is sufficiently large, the correction scheme is not able to model the decay and correctly compensate for it.

6 MEASUREMENT AND OPTIMISATION OF THE FIDELITY OF THE NAVIGATOR TRAJECTORY

6.1 Trajectory Measurement

The simulated data presented in the previous chapter assumed an ideal navigator trajectory. However, in real world experiments deviations from the ideal trajectory can be caused by a multitude of effects. Among others eddy currents, gradient delays, gradient amplitude non–linearity and gradient hysteresis [53] can affect the navigator trajectory. Thus, it is advisable to measure the k–space trajectory fidelity of the navigator with one of the available k-space trajectory measurement techniques[54, 55, 56].

6.1.1 Method

k–space trajectory measurements of the Lissajous navigator trajectory were performed using the method proposed by Duyn et al. in [55]. This technique was inspired by the method developed by Mason et al. [54], who used a dedicated phantom with an isolated spin population measured at different positions in the scanner to map k–space trajectories. Instead of using a dedicated phantom, Duyn et al. simply used conventional slice selection. Only two measurements are required for each of the physical gradient axes. One is a reference measurement consisting of only the slice encoding process and subsequent readout without gradients. The second measurement consists of the same slice encoding followed by a navigator gradient for the investigated axis. If the slice encoding direction is chosen to be the same direction as the navigator gradient and the slice is positioned off–centre, the phase difference $\Delta\Phi_i(t)$ between those two measurements is linked to the k–space trajectory $k_i(t)$ by

$$\Delta\Phi_i(t) = \int_0^t \gamma G_i(t) \cdot D_i \cdot dt = D_i \cdot k_i(t), \tag{6.1}$$

where γ denotes the gyromagnetic ratio, $G_i(t)$ is the spatial encoding gradient amplitude, i is the encoding direction (the physical x–, y– or z–axis) and D_i is the distance of the slice to the gradient isocentre. Thus, for each axis the actual k–space trajectory can be calculated by dividing the measured phase differences by the off–centre distance of the slice:

$$k_i(t) = \frac{\Delta\Phi_i(t)}{D_i}. \tag{6.2}$$

6.1.2 Measurements

Measurements where performed on a Magnetom Tim Trio (Siemens AG, Medical Solutions, Erlangen, Germany), a 3 Tesla system with a single channel transmit/receive coil manufactured by Aurora Instr. Inc., OH 44202 USA. A spherical phantom of diameter $D_{phantom} = 170mm$ filled with a solution of 1.25g $NiSO_4$ x 6 H_2O per 1000g H_2O was placed in the isocentre of the magnet. For each gradient direction the reference and encoding acquisitions were interleaved and repeated 32 times for signal averaging. Measurements were performed for the three physical gradient axes. The navigator parameters were $n_\phi = 20$, $n_\theta = 21$ and $k_{rad} = 0.8cm^{-1}$, number of sampling points $N_{samp} = 8000$, and a total acquisition time of $t_{acq} = 8ms$. The slice thickness was $2mm$, and the slice position was located $40mm$ off–centre. To reduce relaxation artefacts a repetition time of $TR = 500ms$ was chosen. The measured phase was unwrapped using the "unwrap" command in Matlab prior to calculating the k–space trajectory according to Equation 6.2. Additionally, the output of the gradient amplifier DAC was measured using a Textronic DPO 4104 digital oscilloscope. All calculations were performed using Matlab (The Mathworks Inc., Natick MA, USA).

6.1.3 Results

The ideal k–space trajectory and the trajectory measured with 64 averaged phase measurements are shown in Figure 6.1.

It is apparent from the figure that the measured trajectory deviates significantly from the ideal trajectory. The angular location of

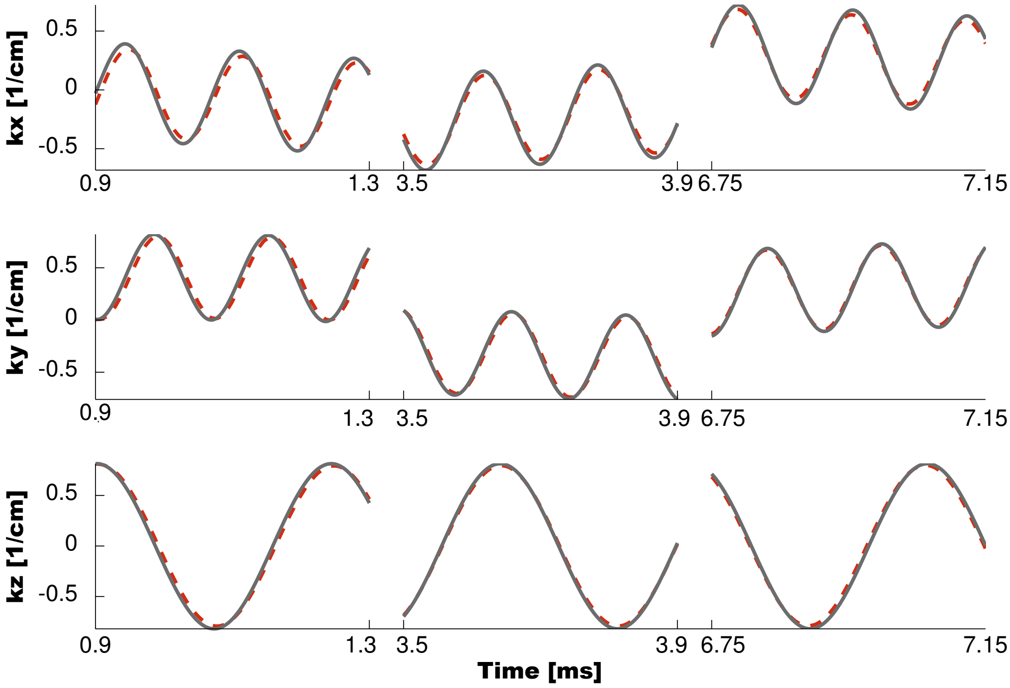

Figure 6.1: The ideal (solid, grey) and measured (dashed, red) navigator trajectory along the kx, ky and kz axis.

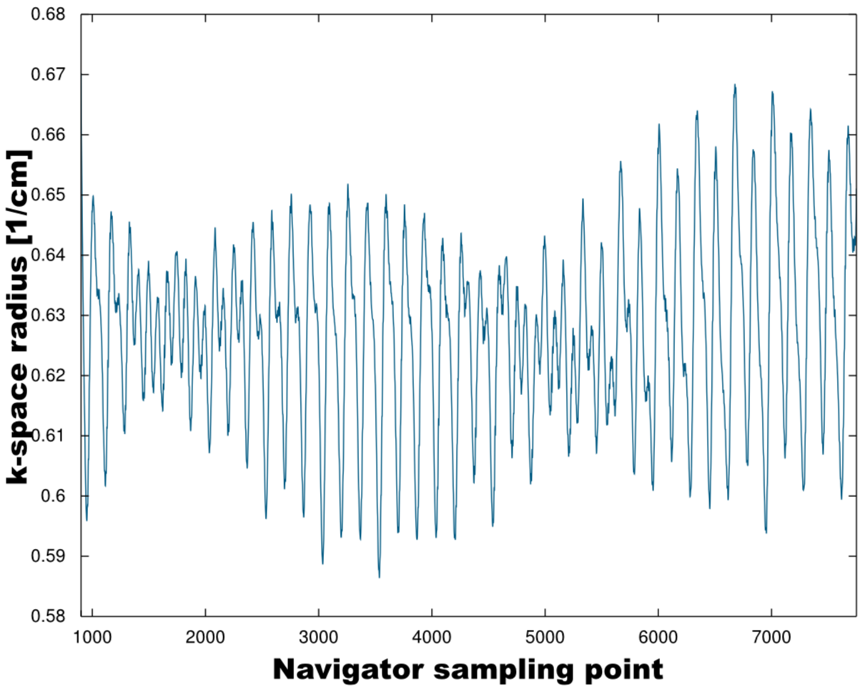

Figure 6.2: Measured k–space trajectory radius as a function of sampling point. Fluctuations in the range of $\pm 6\%$ occur.

the sampling points on the sphere deviates from the ideal points. Moreover, variations of the k–space radius occur during the acquisition. Figure 6.2 shows the measured k–space radius of the Lissajous navigator. Deviations of $\pm 6\%$ from the mean radius are visible.

6.2 Trajectory Correction

For imaging experiments it is not always mandatory to measure exactly on the theoretical trajectory. Images can often be reconstructed by knowing the actual trajectory and including this knowledge into the reconstruction process [57]. In case of the Lissajous navigator, this approach would be feasible if the variation in the k–space trajectory was limited to deviations in the angular coordinates. Due to the amount of sampling points on the surface of the sphere, a small angular deviation from the calculated trajectory would have little influence, as long as the deviation is known, and the actual trajectory is input into the estimation process. Thus, interpolations on the spherical surface would be affected only minimally. Radius variation on the other hand, cannot readily be corrected in post processing. They lead to a modulation of the signal magnitude. Since there are no other sampling points in radial direction which could be used for interpolation, this effect cannot be corrected. Thus, it is necessary to compensate the effects of the gradient infidelities described in Section 6.1. For this purpose the novel iterative gradient correction scheme described in this section was developed.

6.2.1 Method

To develop a correction method which yields the expected results, the measurement process in a current MRI scanner has to be examined in closer detail. The process is shown schematically in Figure 6.3.

The MRI scanner is programmed using an ideal gradient shape. However, the ideal waveform is not the waveform which is finally generated by the gradient amplifiers. Internally, the scanner software first adjusts the ideal gradients to compensate undesired influences such as gradient delays and eddy currents. This adjusted gradient shape is the input function to the gradient amplifiers. Most of these correction methods are proprietary and there is little or no infor-

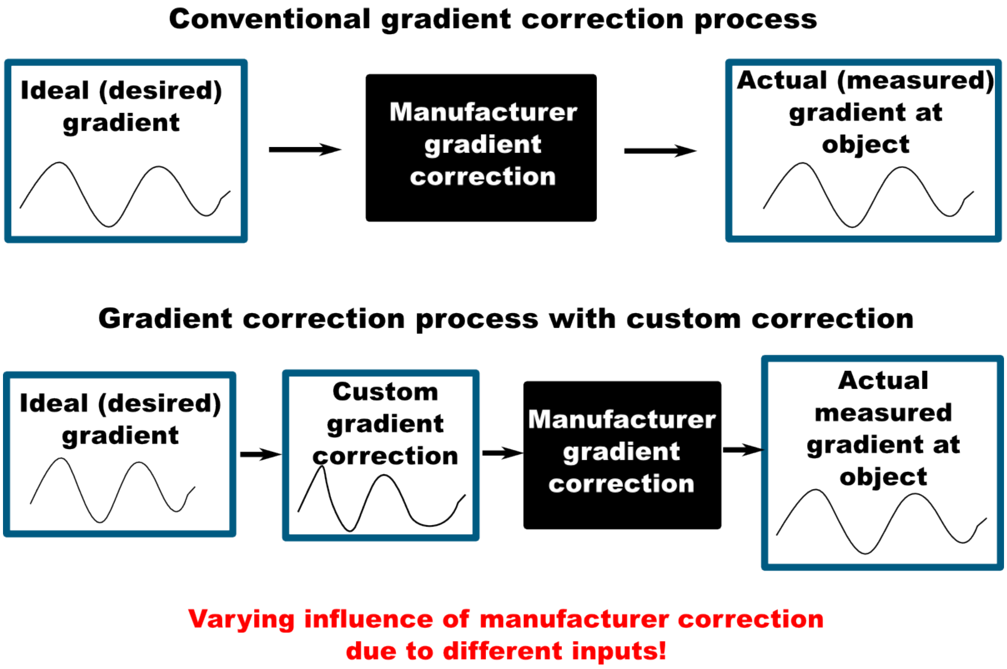
Conventional gradient correction process
Ideal (desired) gradient
Manufacturer gradient correction
Actual (measured) gradient at object
Gradient correction process with custom correction
Ideal (desired) gradient
Custom gradient correction
Manufacturer gradient correction
Actual measured gradient at object
Varying influence of manufacturer correction due to different inputs!

Figure 6.3: System manufacturers of MRI scanners include gradient correction schemes into their systems. The scanner pre–distorts the ideal gradients in the manufacturer's correction algorithms to yield a gradient close to the ideal gradient in the measured object. A custom gradient correction is performed *before* the manufacturer gradient correction delivering a different input to the manufacturer correction. Thus manufacturer and custom correction procedures are not entirely independent.

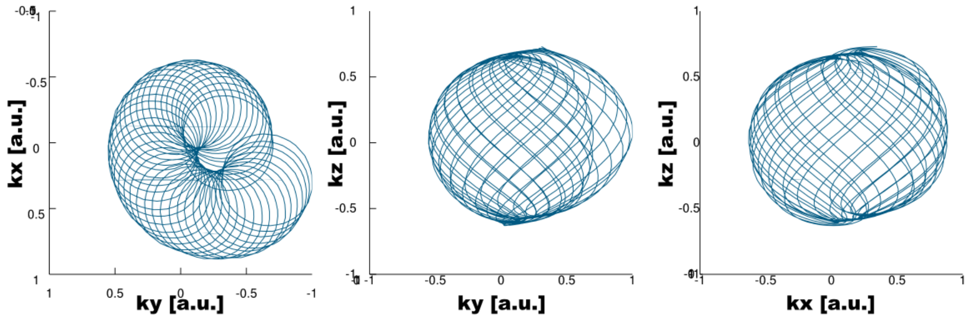

Figure 6.4: Predistorted navigator k-space trajectory reconstructed from the amplifier DAC output of the scanner from three different perspectives. The first order shims (gradient offsets) were subtracted prior to reconstruction. In the absence of scanner pre–emphasis corrections an ideal Lissajous navigator would be shown. The distortions show the extend of corrections applied by the scanner.

mation about them. Due to the system design, a custom gradient correction scheme can only be introduced before the black–box manufacturer correction (see Figure 6.3). However, this has the effect, that the manufacturer calculation receives a different input and potentially performs a different correction than with the ideal gradient shape as input. Since the manufacturer correction significantly alters the k–space trajectory (see Figure 6.4), unexpected performance might occur.

To counteract this effect, while minimising any remaining k–space trajectory infidelities, a novel iterative correction scheme was developed. The algorithm performs the following steps:

1. Measurement of the gradient shapes in the object by excitation with ideal (desired) gradients.
2. Filtering of measured gradients with a Butterworth filter [58]

for noise reduction.

3. Calculation of gradient delays as a function of time over the whole gradient shape.
4. Compensate measured and filtered gradient by the delays calculated in Step 3.
5. Calculate difference between ideal navigator and post processed (filtered & delay compensated) gradient.
6. Add difference to excitation gradient shape used in Step 1 as correction factor.
7. Pre–warp gradient from previous step by the calculated gradient delay factors.
8. Repeat procedure with the pre–warped and amplitude corrected gradient as excitation gradient.

   During the second iteration no delay correction is necessary as this is performed reliably during the first iteration.

A flow–chart of the correction procedure is shown in Figure 6.5.

Trajectory correction measurements were performed on a Magnetom Tim Trio using the same phantom and navigator settings as described in Section 6.1.2. The measured raw data were exported offline and processed using Matlab. The calculated, corrected gradient shapes were used for a second trajectory measurement. These data were used for calculation of the second iteration correction factors.

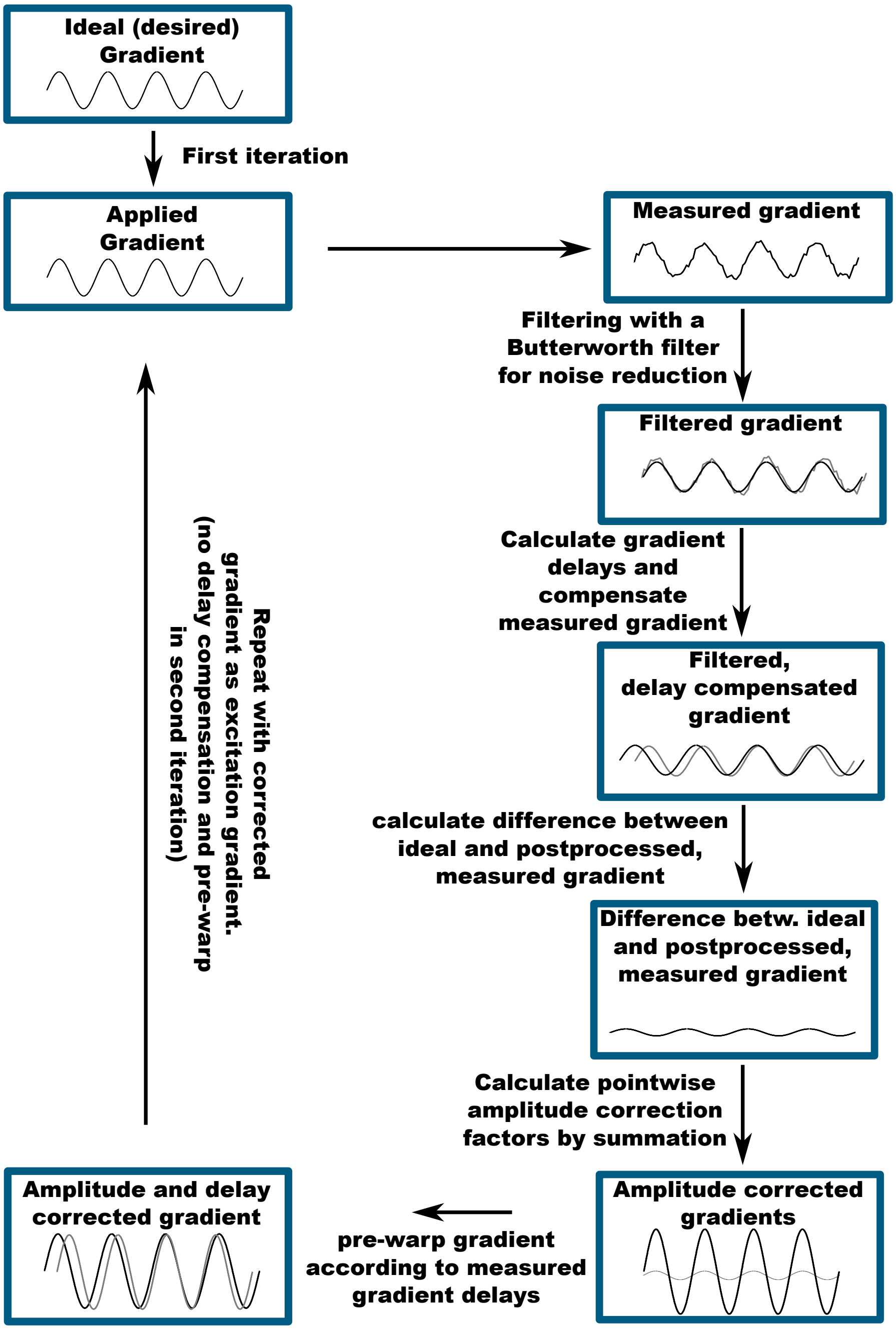
Ideal (desired) Gradient
First iteration
Applied Gradient
Measured gradient
Filtering with a Butterworth filter for noise reduction
Filtered gradient
Calculate gradient delays and compensate measured gradient
Filtered, delay compensated gradient
calculate difference between ideal and postprocessed, measured gradient
Difference betw. ideal and postprocessed, measured gradient
Calculate pointwise amplitude correction factors by summation
Amplitude corrected gradients
pre-warp gradient according to measured gradient delays
Amplitude and delay corrected gradient
Repeat with corrected gradient as excitation gradient. (no delay compensation and pre-warp in second iteration)

Figure 6.5: The iterative gradient correction algorithm measures the gradients in the object when excited with the ideal (desired) gradients. The measured gradients are filtered, and then the gradient delay is calculated as a function of time. The measured gradients are warped with those delay factors. Then the difference to the ideal scheme is calculated. This difference is added on top of excitation gradient as correction factor. Finally, the result is pre–warped to compensate for the measured gradient delays. The process is repeated for a second iteration with the corrected gradient as excitation pattern.

Finally, a third trajectory measurement was undertaken to validate the results of the correction procedure.

6.2.2 Results

Gradient Delays

Figure 6.6 shows the measured gradient delays as a function of time for the uncorrected navigator gradient (left) and for the navigator gradients after the first iteration of the correction procedure (right). The gradient delay is not a constant factor during the complete time of the navigator gradient, but rather a linearly growing delay is observed. The residual gradient delays after the correction process are below $\pm 1 \mu s$ and exhibit little change over the course of the navigator. The slightly larger spread of the measurements of the z–gradient delay is a result of the lower frequency of the navigator gradient on this axis. The delay estimation algorithm performs better with higher frequency gradients.

This surprising result of a linearly–varying gradient delay was confirmed by a second, independent method (data shown in Figure 6.7): during the acquisition of Lissajous navigators, two of the three physical gradients were disabled. This leads to multiple traversals of the k–space centre during each acquisition. Every time the k–space centre is traversed a local signal maximum occurs in the magnitude data. From these acquisitions gradient delays were calculated by calculating the time difference between the local signal maxima and the theoretical time of k–space centre traversal. These measurements confirmed the observed linear variation in gradient delay throughout

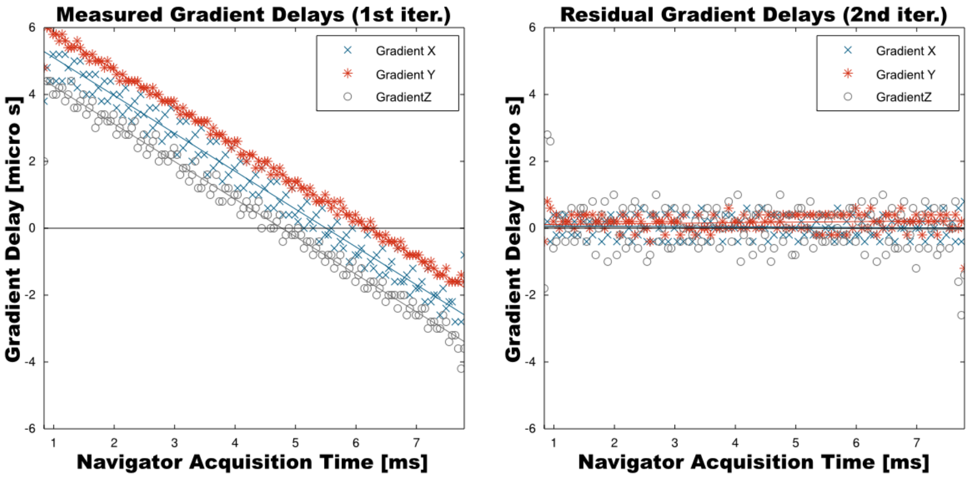

Figure 6.6: Measured gradient delays by trajectory measurement: on the left, the measured gradient delays of the uncorrected navigator gradient are shown for the three logical gradient axes. On the right, the residual gradient delays after the first iteration of the correction process are shown. A significant reduction of the gradient delays is apparent.

the navigator acquisition.

A counterintuitive result is the negative gradient delay (the measured gradient precedes the ideal gradient!) towards the end of the navigator acquisition. A likely explanation for this is the manufacturer's gradient delay correction. Assuming a linearly–varying gradient delay is present and only a constant delay factor is available for correction, how would a reasonable delay correction factor be chosen? Since we are considering imaging the most important part of the raw data is the echo centre. Thus, choosing the delay correction factor such that the delay is zero at the echo centre is an obvious choice. In most imaging acquisition the echo occurs at the centre of the gradient, unless an asymmetric echo is used. Thus, for a $8ms$ navigator gradient one would expect little or no delay around an acquisition time of $4ms$.

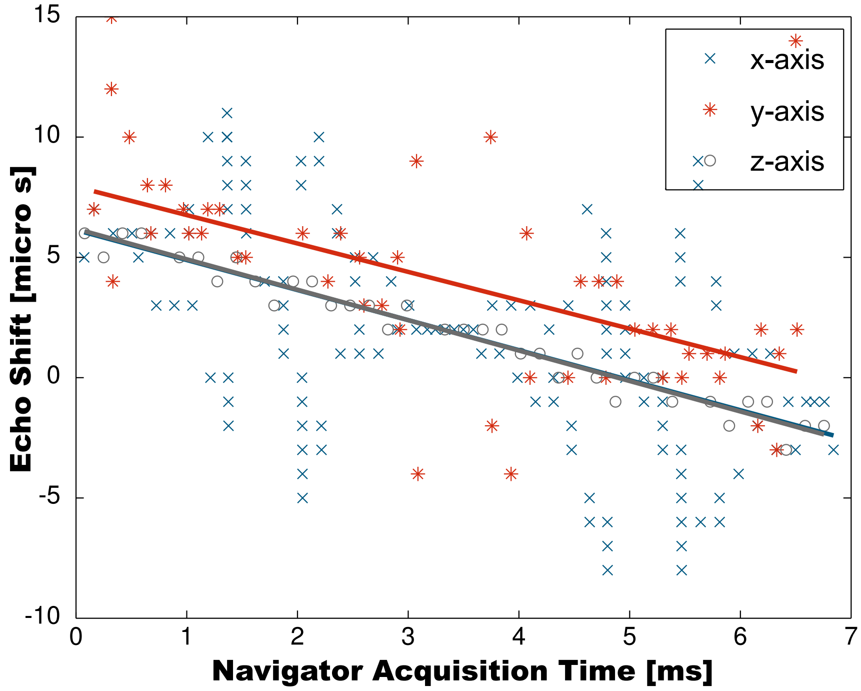

Figure 6.7: Measured gradient delays by echo shift: the measured gradient delays of the uncorrected navigator gradient are shown for the three logical gradient axes along with their regression lines.

Trajectory Fidelity

Figure 6.8 shows the ideal trajectory on the left, the measured uncorrected trajectory in the middle and the corrected trajectory on the right. A zoomed view of the pole–cap is shown in Figure 6.9. The corrected trajectory shows less deviation from the ideal trajectory than the uncorrected one.

Figure 6.10 shows the ideal radius, the uncorrected measured radius and the measured, corrected radius after scaling to an identical mean for better comparison. Figure 6.11 shows a zoomed view of Figure 6.10.

A small modulation of ±0.9% was introduced in the radius of the Lissajous navigator. The effectiveness of the iterative correction method can be seen on the ability to reproduce this modulation. Compared with before correction, the mean absolute error of the radius of the corrected trajectory was reduced by one order of magnitude from 2.1% to 0.2%, while the maximum error was reduced from 7.4% to 1.0%.

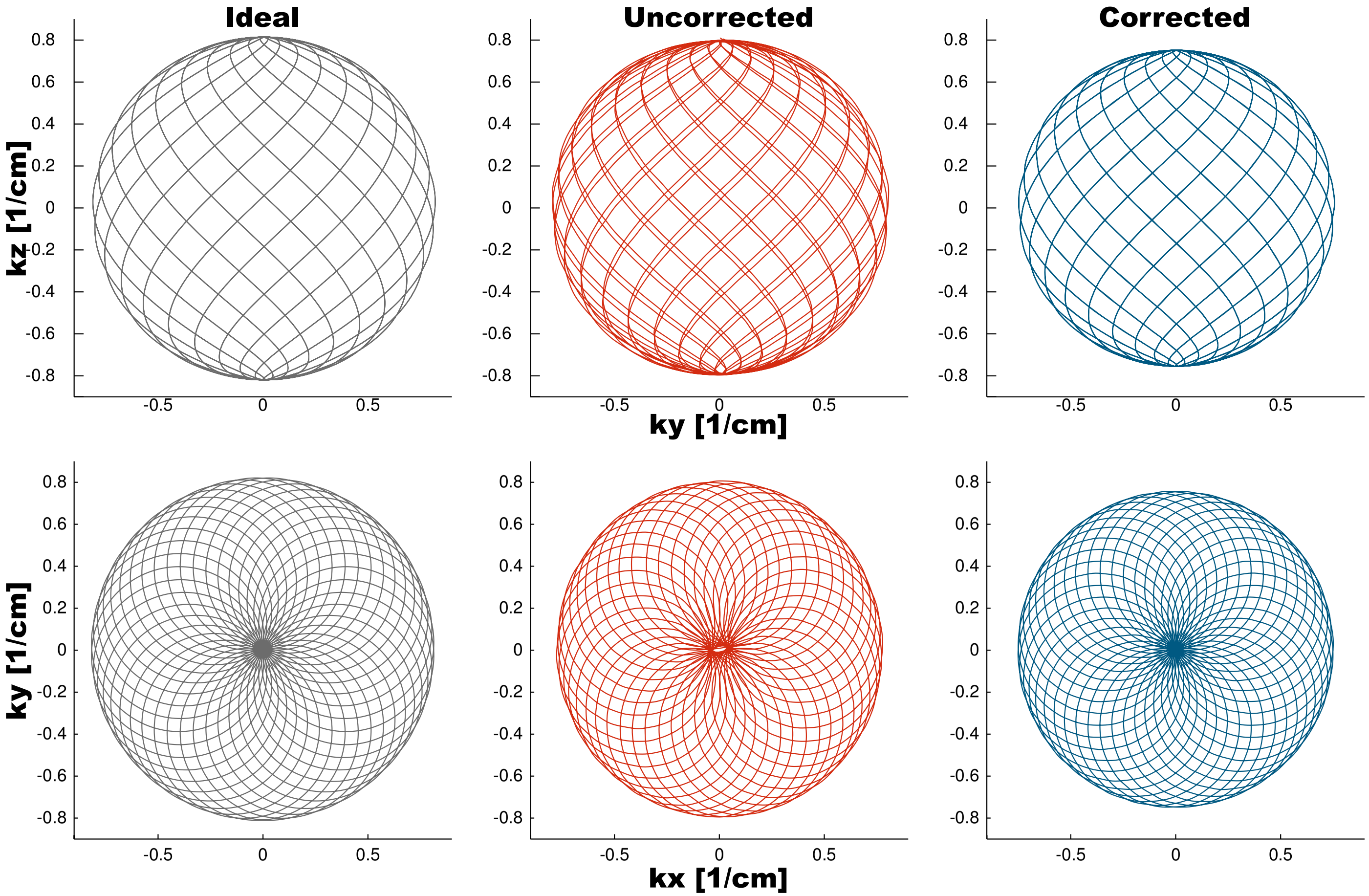

Figure 6.8: Ideal (grey, left), uncorrected (red, middle), and corrected (blue, right) navigator k–space trajectory. The iterative k–space trajectory correction method clearly improves the trajectory fidelity. A zoomed view is shown in Figure 6.9.

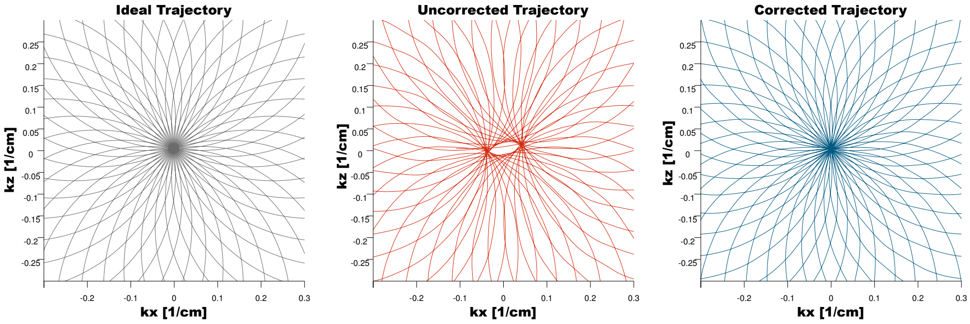

Figure 6.9: Zoomed view of the ideal (grey, left), uncorrected (red, middle), and corrected (blue, right) navigator k–space trajectory. The iterative k–space trajectory correction method clearly improves the trajectory fidelity.

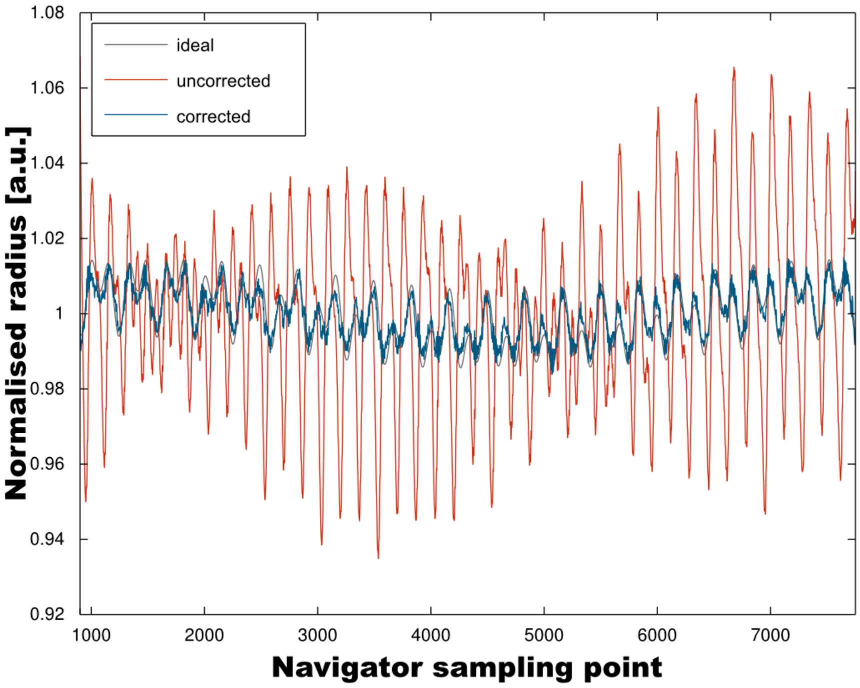

Figure 6.10: k–space radius deviations for the ideal (grey) trajectory, the uncorrected measured (red) trajectory and the corrected (blue) trajectory. All curves were normalised to the identical mean radius for better comparison.

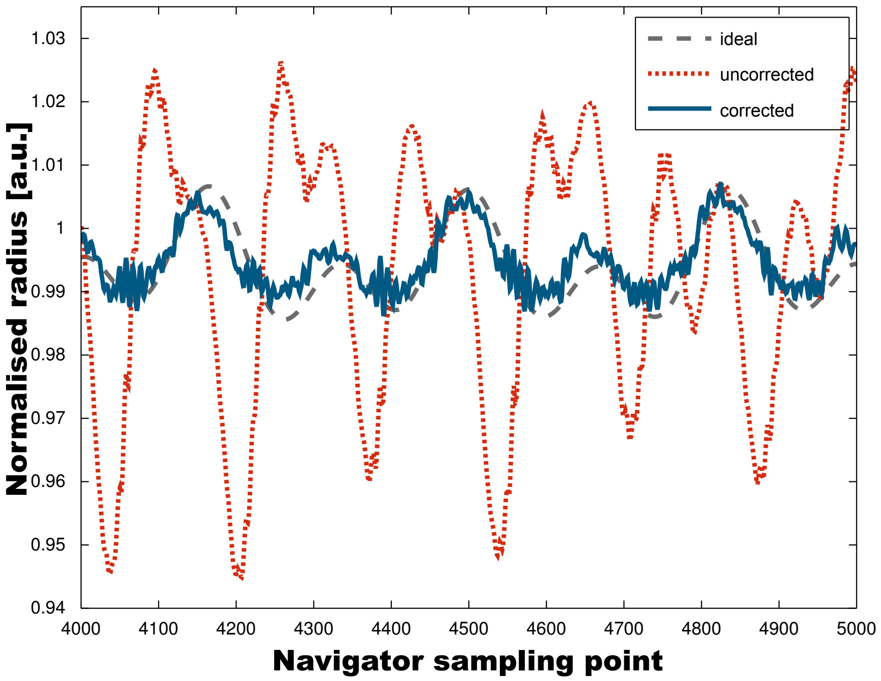

Figure 6.11: k–space radius deviations for the ideal trajectory (grey, dashed), the uncorrected measured trajectory (red, dotted) and the corrected trajectory (blue, solid). Zoomed view of Figure 6.10.

7 Experimental Comparison of the Lissajous Navigator and the Spherical Navigator

The developed Lissajous navigator trajectory was implemented on the Siemens Magnetom platform and compared experimentally to an implementation of the spherical navigator under identical conditions. The procedures and results of this investigation are described in this chapter.

7.1 Navigator Sequence

The navigator acquisition was spliced into a conventional three–dimensional FLASH sequence such that before each k–space line ac-

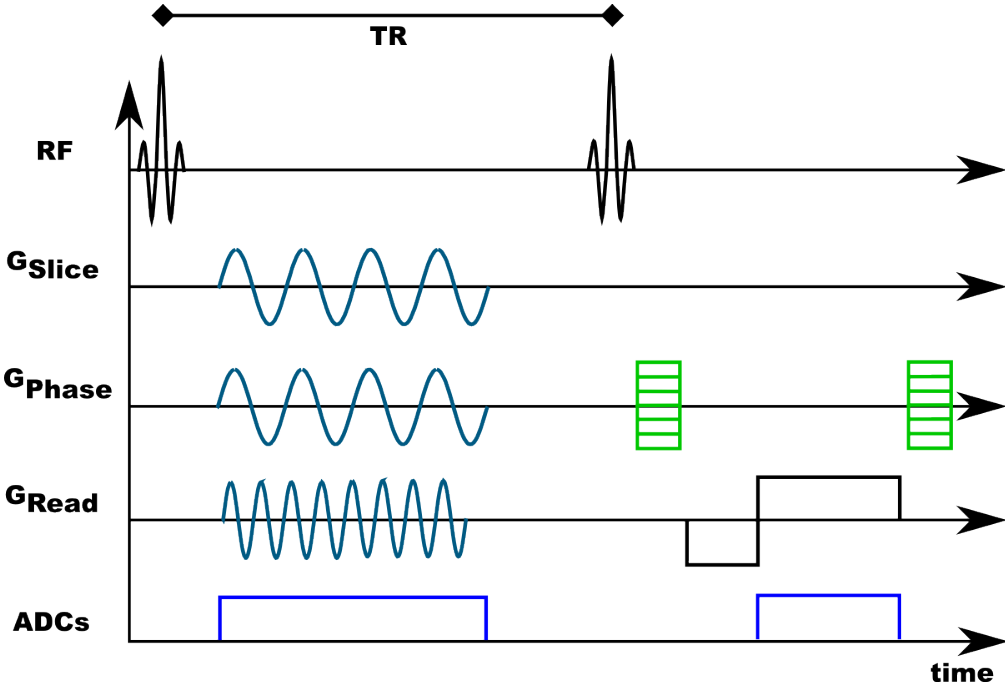

Figure 7.1: Sequence diagram of the modified navigator FLASH sequence. Before the acquisition of each FLASH line, a navigator is measured with a separate RF pulse. Navigator and line acquisition have identical repetition time, TR.

quisition, a navigator was acquired with a separate RF pulse. The sequence diagram of the sequence used is given in Figure 7.1. Both FLASH line readout and navigator acquisition used identical repetition times, TR.

7.2 Virtual Rotation

Establishing a gold standard for rotations in an MRI scanner is problematic. Automated mechanical systems are often incompatible with the high magnetic field strength and are prone to introduce electrical noise in the measurements. Furthermore, a high degree of accuracy on the order of a tenth of a degree is needed, which can be challenging to achieve even when ignoring the problem of magnetic field compatibility.

One approach not relying on external hardware is to introduce virtual rotations. That is, the imaged object is kept steady while the gradient waveforms are rotated. One drawback of this method is that the inhomogeneities of the static magnetic field and the RF excitation field on the rotation estimation are likely to be underestimated. On the other hand, the best possible gold standard for the rotation parameters is obtained: the exact input value. For this reason, virtual rotations were implemented into the sequence described in Section 7.1. The rotation parameters used throughout the measurements presented in this chapter consisted of sinusoidal rotations between -30°and 30°. Rotations were applied around a single physical gradient axis at a time, that is, sequentially for all three axes. Figure 7.2 depicts a plot of the virtual rotation parameters used. For measurements with more than 300 navigators, the rotation pattern was repeated until the end of the measurement.

7.3 Two–Chamber Phantom

All measurements were performed with a two–chamber phantom [59] with both chambers filled with a solution of 3.75g $NiSO_4$ x 6 H_2O + 5g $NaCl$ per 1000g H_2O on a 3 Tesla system. Figure 7.3 depicts a photograph and Figure 7.4 a FLASH image of the phantom.

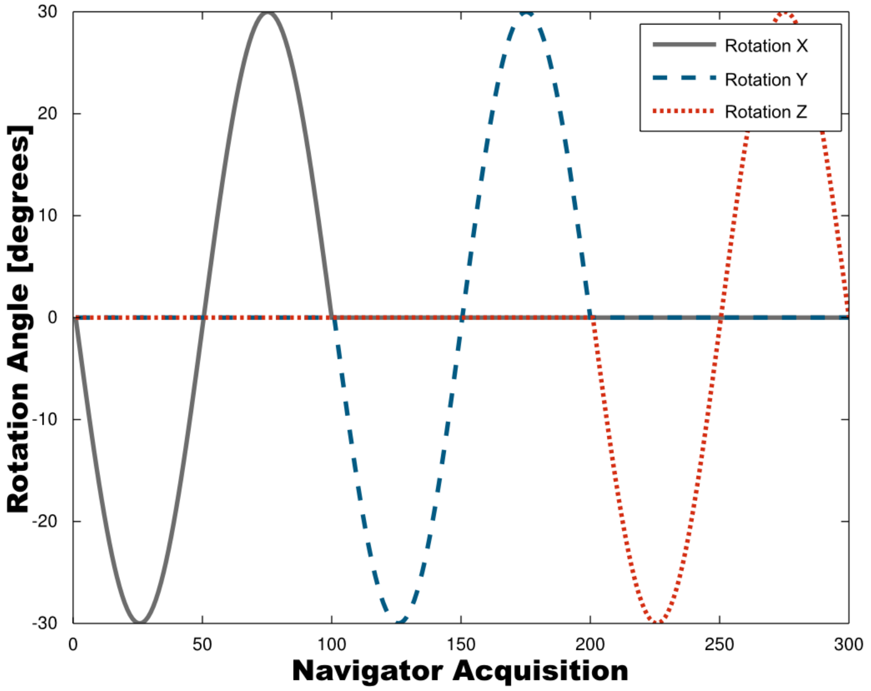

Figure 7.2: Plot of the virtual rotation parameters used in the sequence.

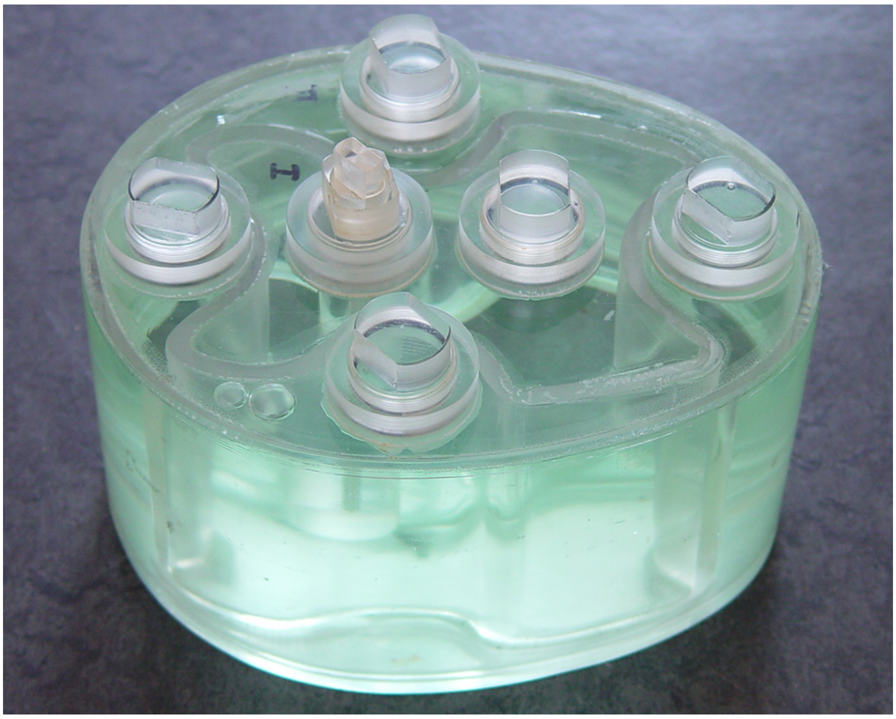

Figure 7.3: Photograph of the two–chamber phantom.

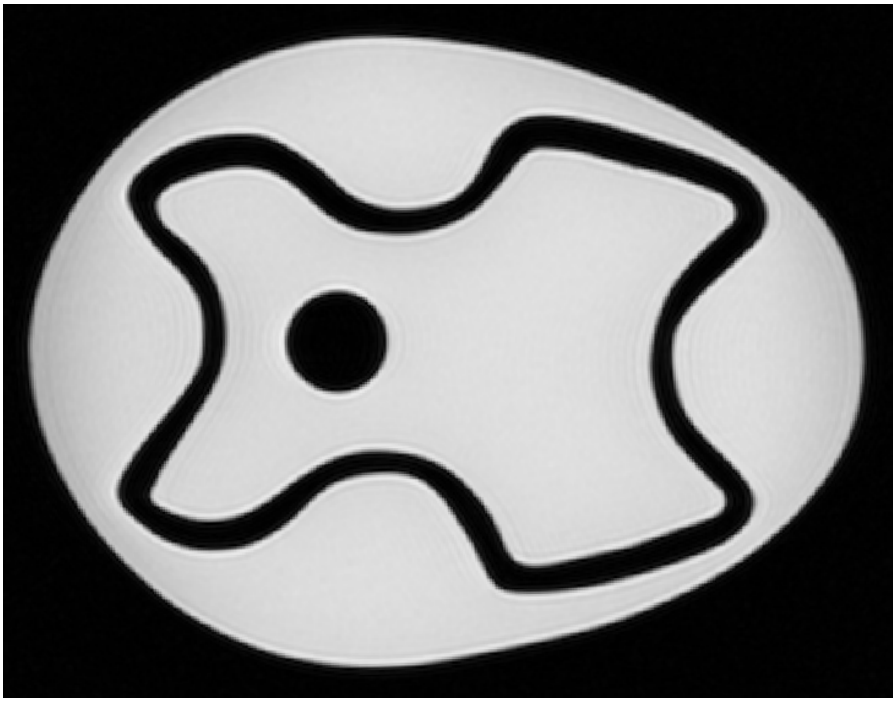

Figure 7.4: Single slice of a FLASH acquisition of the two–chamber phantom.

7.4 Sequence and Navigator Parameters

A matrix size of (64 read x 32 slice x 40 phase) with a field–of–view of (270mm x 160mm x 169 mm) and a slice thickness of $5mm$ were used for all measurements. The navigator duration for all measurements was $8ms$ including the dephasing and rephasing necessary to reach the necessary k–space radius. A total of 8000 samples were acquired for each navigator of which 6850 were located on the spherical surface. Since the virtual rotations change the gradient moments on the physical axes, something that can lead to artefacts from residual magnetisation, all measurements using virtual rotations were acquired using a long repetition time of $TR = 1500ms$.

7.5 Measurements

7.5.1 Radius Optimisation Measurements

To find the optimal radius for rotation estimation, measurements were performed at k–space radii ranging from $0.4\frac{1}{cm}$ to $1.2\frac{1}{cm}$ in steps of $0.13\frac{1}{cm}$. The optimal k–space radius was found by analysing the rotation estimates and by choosing the radius with the lowest mean absolute error of all rotation estimates. Initial measurements revealed that the optimal radius was identical for both the Lissajous and the spherical navigator. Thus, radius optimisation was subsequently performed for a single navigator (usually the non–optimised Lissajous navigator). This radius was applied for all three navigators: spherical, uncorrected Lissajous and corrected Lissajous navigator.

7.5.2 Trajectory Optimisation

For the Lissajous navigator at the optimal k–space radius, a trajectory optimisation was carried out according to the procedure described in Chapter 6.

7.5.3 Navigator Comparison Measurements

At the optimal radius three scans were performed: one with spherical navigator, one with the Lissajous navigator and a third with the Lissajous navigator with an optimised trajectory spliced into the FLASH sequence described in Section 7.1. The three measurements were performed with identical shim settings and object positions for optimal comparability.

7.6 Analysis

The acquired raw data were exported and analysed off–line with the algorithms described in detail in Chapter 4.1. To reduce the computational complexity, only every third data point (a total of 2283) was used for rotation estimation. Every third data point was chosen because as shown in reference [1], two thousand data points are sufficient for rotation estimation. The interpolation process used a width of 6° for the Gaussian kernel.

7.7 Results

The radius optimisation measurements showed the best accuracy of rotation estimation can be achieved with a radius of $k_{rad} = 0.8 \frac{1}{cm}$.

Figures 7.5-7.7 show plots of the measured magnitude signal for the spherical navigator, the Lissajous navigator, and the Lissajous navigator with an optimised trajectory fidelity, respectively. Comparing the non–optimised and the optimised Lissajous navigator, less signal fluctuations are visible in the optimised navigator. The sole difference between the measurements in Figure 7.6 and Figure 7.7 is the application of the trajectory correction algorithm developed here, which was shown to reduce k–space radius fluctuations (Section 6.2). Thus, it is concluded, that the reduced radius variations in the optimised trajectory reduce magnitude signal fluctuations in the Lissajous navigator.

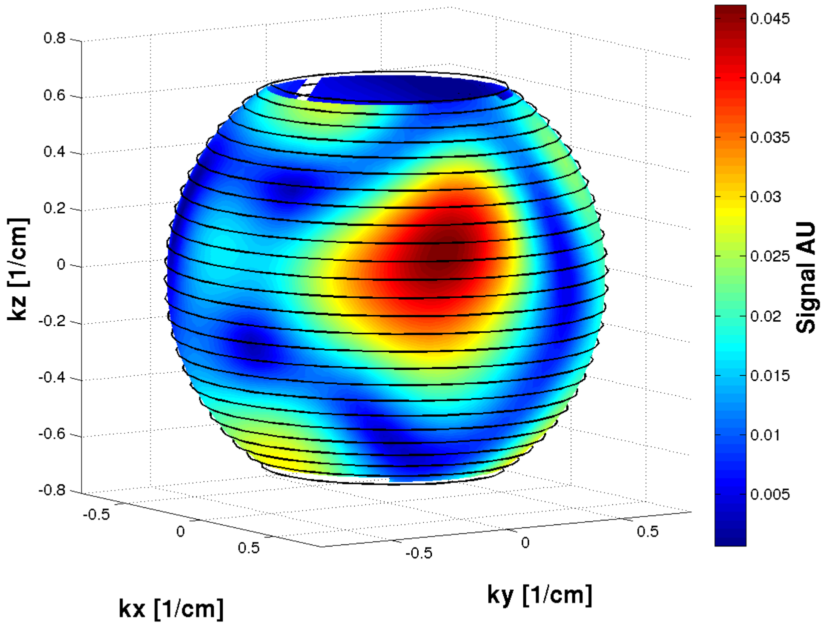

Figure 7.5: Magnitude signal of a spherical navigator acquisition at 3 Tesla with a k–space radius of 0.8 $\frac{1}{cm}$ overlaid by the navigator trajectory in black.

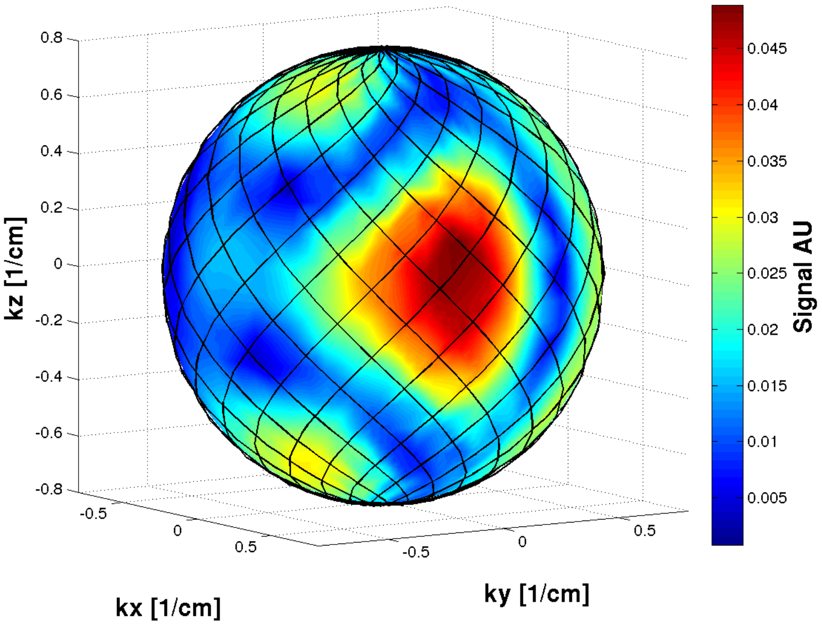

Figure 7.6: Magnitude signal of a Lissajous navigator acquisition at 3 Tesla with a k–space radius of 0.8 $\frac{1}{cm}$ overlaid by the navigator trajectory in black.

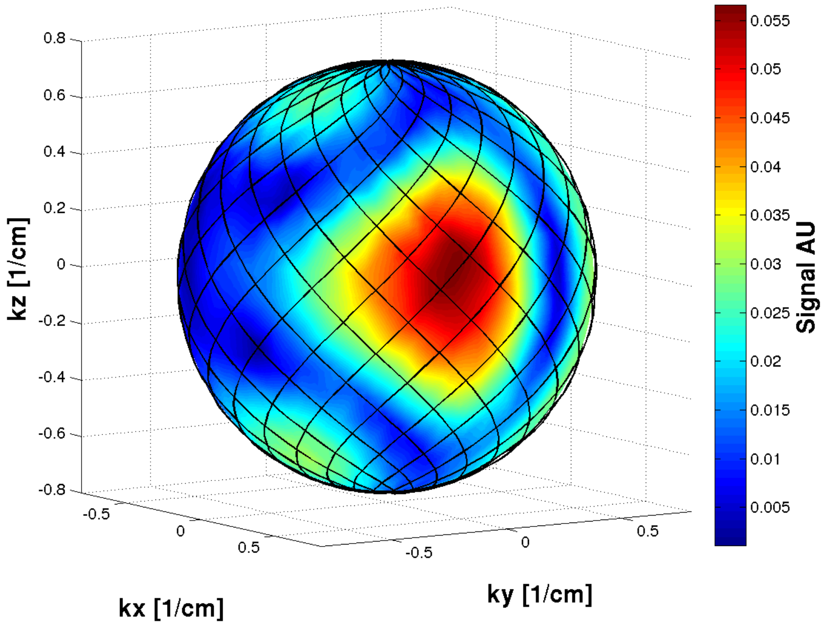

Figure 7.7: Magnitude signal of a Lissajous navigator acquisition with optimised trajectory fidelity at 3 Tesla with a k-space radius of 0.8 $\frac{1}{cm}$ overlaid by the navigator trajectory in black. Compared with Figure 7.6 a smoother signal distribution is visible. This is an effect of the corrected trajectory.

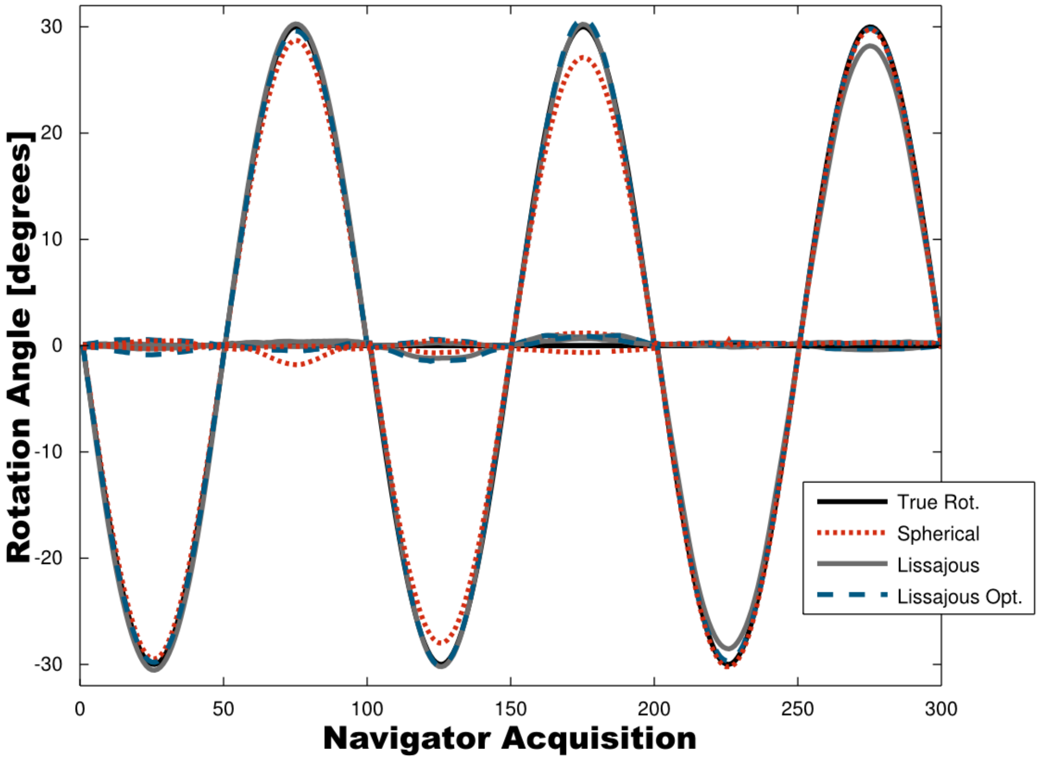

Figure 7.8: Plot of the true rotations (black, solid), rotation estimates for the spherical navigator (red, dotted), Lissajous navigator (grey, solid), and the Lissajous navigator with optimised trajectory fidelity (blue, dashed).

Figure 7.8 depicts a plot of the gold standard rotation parameters and the measured rotation parameters using the spherical navigator, the Lissajous navigator, and the Lissajous navigator using the corrected k–space trajectory.

In Figure 7.9 the error in the rotation estimates on the axis of rotation for rotations around x, y and z (from left to right) is plotted as a function of rotation angle. Figures 7.10-7.12 depict plots of the absolute error of the rotation estimates for the off–rotation axis, for the spherical navigator and the Lissajous navigator with and

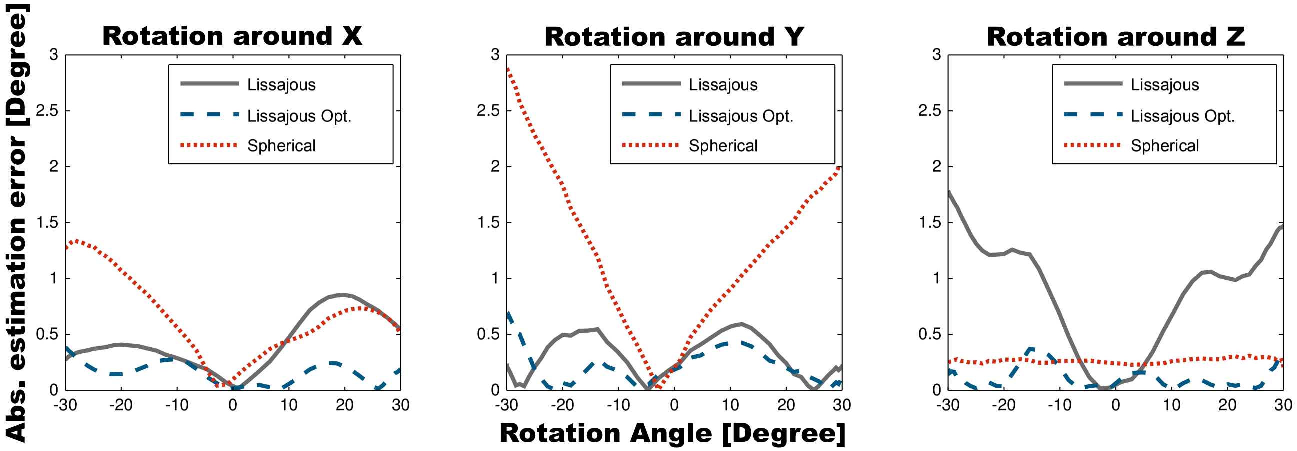

Figure 7.9: Absolute error of the rotation estimates on the axis of rotation for the spherical navigator (red dash–dotted), Lissajous navigator (grey, solid), and the Lissajous navigator with optimised trajectory (blue, dashed), for rotations around the three physical axes.

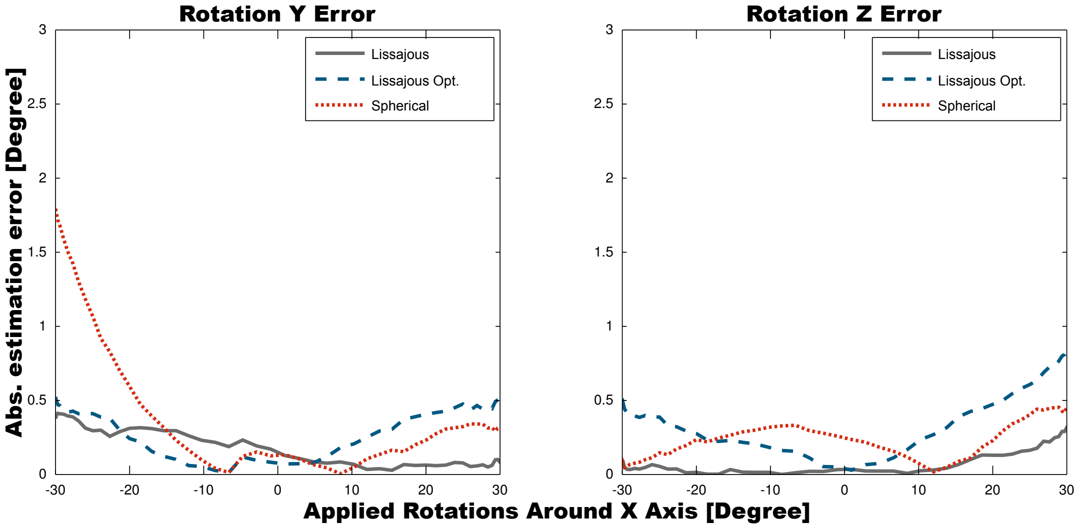

Figure 7.10: Plot of the absolute rotation estimate errors on the off–rotation axes for rotations around x.

without trajectory optimisations. Here, the absolute error equals the estimated rotation angle, as the true rotation around the axis was zero degree.

The mean absolute rotation error for the spherical navigator for all three axis combined was measured to 0.50° for the spherical navigator, 0.38° for the Lissajous navigator, and 0.31° for the trajectory optimised Lissajous navigator. The maximum absolute errors on any axis for the three navigators are 2.9° (spherical), 1.8° (Lissajous), and 1.5° (Lissajous, optimised trajectory fidelity).

7.8 Discussion

The optimal radius reported here is not a given constant for all measurements. Two confounding factors influence the optimal radius.

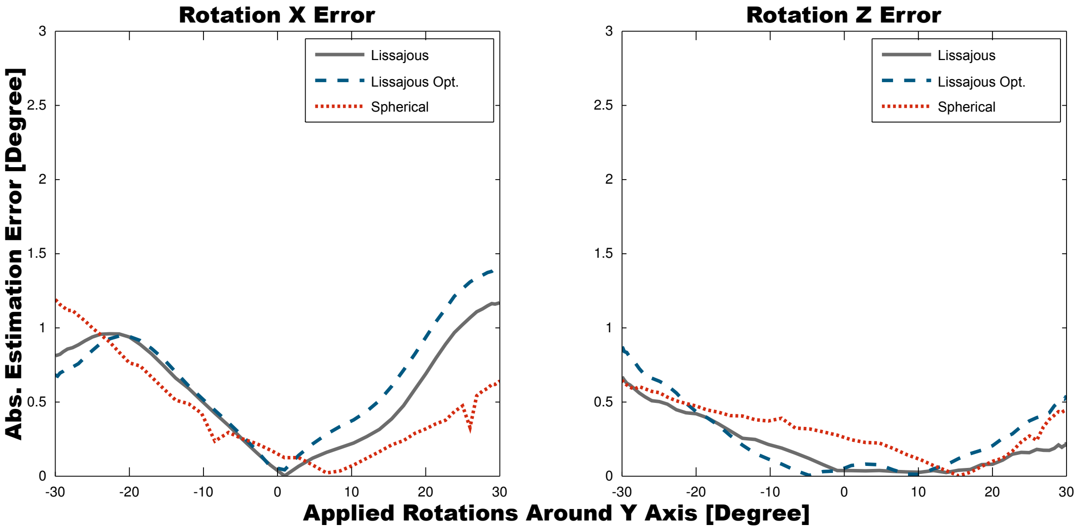

Figure 7.11: Plot of the absolute rotation estimate errors on the off–rotation axes for rotations around y.

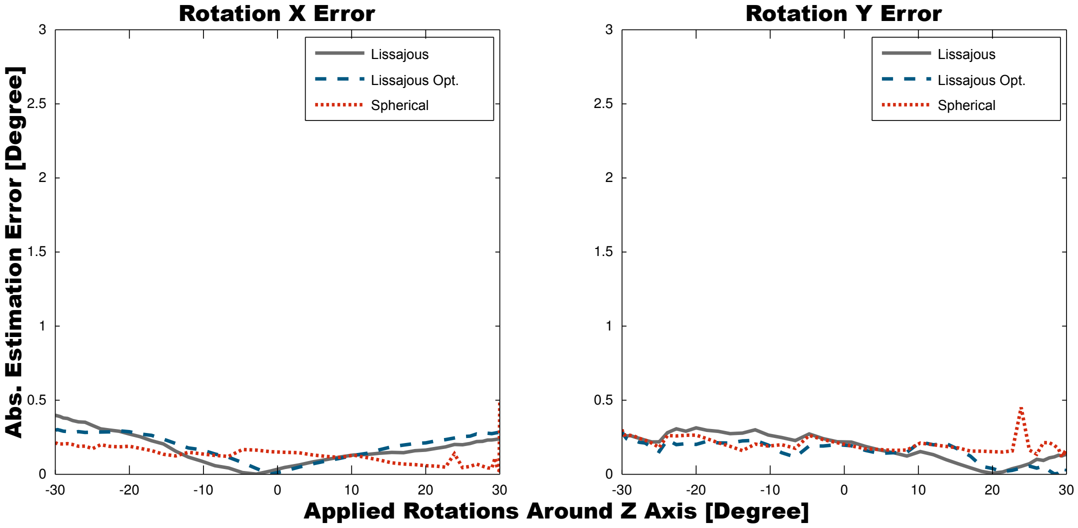

Figure 7.12: Plot of the absolute rotation estimate errors on the off–rotation axes for rotations around z.

The first one is the amount of magnitude features on the spherical surface. Close to the centre of k–space there are only a few broad features on the navigator surface. Towards larger radii, the amount of k-space features increases. Since the pattern matching performs better when more features are present, a large radius is desirable when only taking into account the magnitude features. The second factor is the signal–to–noise ratio . At smaller radii in the centre of k–space the signal–to–noise ratio is much higher than at larger radii. Thus, from a signal–to–noise ratio perspective, a small radius would be desirable. These two divergent effects lead to an optimal radius being determined as a compromise between the amount of magnitude features and the signal–to–noise ratio of the measurement. The optimal radius is also dependent on the imaged object, as its shape influences the k–space feature pattern. However, since all brains and heads share similar macroscopic shapes, we expect an optimisation for one head to be sufficiently accurate for most other heads also. Thus, for *in vivo* applications, the radius will have to be optimised separately.

The anisotropy of the spherical navigator reported in reference [1] can be confirmed. This particular navigator trajectory has a single preferential rotation axis (z), along which the accuracy of rotation detection is high for the complete parameter space. However, rotations around the other two axes (x, y) rapidly lead to a loss of accuracy. The errors grow nearly linear to maximum values of 1.4° and 2.9°. In contrast, the accuracy of the rotation estimation of the Lissajous navigator exhibits a higher degree of isotropy. The results for rotation axis errors are similar for all three axes. The rotation axis error shows a characteristic curve, where the error first increases and then decreases in a sinusoidal fashion at larger rotations angles. A minimum is located at roughly 20° with some deviations depending on the axis. At a rotation angle of approximately $10^\circ - 15^\circ$ the errors in the Lissajous navigator reach their maximum. A detailed explanation of the characteristic shape of the error curve for both the spherical and the Lissajous navigator will be given in the following paragraphs.

The linear increase in the estimation of the error of the spherical navigator can be attributed to the incomplete coverage of the sphere. The more magnitude features rotate out of the sampled area of the navigator, the worse the pattern matching performs. The absence of this linear increase in the measurements of the trajectory–corrected Lissajous navigator is a result of the full sphere coverage.

To explain the characteristic error curve of the Lissajous navigator with its regular local minima and maxima, a detailed look at the Lissajous trajectory is necessary. The thread spacing of the navigator — the angular distance between two consecutive figure eights of the navigator — is 18°. This value is close to the spacing of the minima in the rotation estimation error of approximately 20°. This leads to the conclusion that the error is caused by interplay between the interpolation procedure and the non–uniform sampling of the Lissajous trajectory. When a navigator is rotated relative to the reference navigator by an angle half the distance between the individual "threads" of the navigator (in the direction of the rotation), the most difficult situation for the interpolation procedure is present. In this case, all sampling points that can be used for interpolation have the largest distance (half of the thread spacing) to the interpolation point. Thus, a lower accuracy of the interpolation procedure has to be expected in such a situation, compared to situations where measurement points are located closer to the interpolation point. At larger rotations sampling points of the adjacent navigator thread are closer to the interpolation point. Thus, the error reduces at larger rotations until it reaches a minimum close to a rotation of a whole thread distance.

The off–rotation axis errors of the Lissajous navigator increase in a nearly linear fashion with rotation angle. The maximum off–rotation axis error is 1.8° for the spherical navigator, 1.2° for the Lissajous navigator and 1.4° for the Lissajous navigator with optimised trajectory fidelity.

The off–rotation axis errors of the Lissajous navigator increase in a nearly linear fashion with rotation angle. The maximum off-rotation axis error is 1.8° for the spherical navigator, 1.2° for the Lissajous navigator and 1.4° for the Lissajous navigator with optimised trajectory fidelity. Interestingly, in some cases the optimised Lissajous trajectory performs better than the Lissajous trajectory on the off–rotation axis. This is likely caused by errors due to relaxation effects and errors due to trajectory fidelity cancelling each other in the uncorrected Lissajous navigator. However, the overall accuracy remains improved by using the optimised trajectory.

7.9 Conclusions

In conclusion, a nearly isotropic rotation estimation error was attained with the Lissajous navigator. Additionally, a reduction in the maximum error of 48%, and an overall increased accuracy of 38% was achieved relative to the spherical navigator with identical postprocessing. The significantly higher isotropy of the Lissajous navigator provides a significant advantage for neuro–imaging applications, for example, where rotations can occur around any axis. In particular, paediatric applications will benefit from motion corrected imaging, as imaging children without motion correction capability is a challenging task. Another application where rapid and large movements occur is imaging of patients with Tourette syndrome. Due to the capability of the Lissajous navigator for accurate determination of large movements a considerable increase in image quality is to be expected. Especially for the most challenging groups with large movements, the Lissajous navigator offers a considerable advantage over the spherical navigator.

8 SUMMARY AND PROSPECTS

8.1 Summary

In this work, a novel three–dimensional navigator — the Lissajous navigator — was developed, which the overcomes shortcomings of the spherical navigator [1]. An overall increase in the accuracy of rotation estimation of 38% from 0.5° to 0.3° with a navigator acquisition time of $8ms$ was achieved. In addition, the homogeneity of the accuracy is significantly higher for the Lissajous navigator than for the spherical navigator. The spherical navigator has one preferential rotation axis around which the rotation estimates are good, but two axes of rotation around which the rotation estimates rapidly lose accuracy with increasing rotation angle. In contrast, the accuracy of the Lissajous navigator is nearly isotropic. This is a direct result of the whole–sphere coverage achieved by the Lissajous sampling scheme.

Numerical MRI simulations were carried out to allow a quantitative comparison of the two navigators under identical conditions

(Chapter 5). The simulations predicted a mean increase in the accuracy of rotation estimation of 50% for the Lissajous navigator (0.2°) relative to the spherical navigator (0.5°) and a reduction of the maximum error by 65% (Section 5.2) from 3.0° (spherical) to 1.0° (Lissajous). Additionally, the influence of signal decay, chemical shift and susceptibility on the rotation estimation was investigated separately for the first time (Section 5.3). The simulations revealed a significant influence of signal decay and chemical shift on the rotation estimation. As a consequence, it is recommended to perform navigated motion correction with fat suppression or chemically selective excitation whenever possible. A strong influence of the signal decay prompted the development of a novel T_2^*–decay correction algorithm (Section 5.5), which utilises the crossing–points in the Lissajous trajectory for decay correction without the necessity to acquire additional data. This auto–correction algorithm allowed for an improvement of the accuracy of rotation estimation by 70% from 1.3° uncorrected to 0.4° corrected at a small k–space radius $(0.03\frac{1}{mm})$, but has limited applicability at larger radii. However, the overall best accuracy of rotation estimation is achieved at a k–space radius of $(0.07\frac{1}{mm})$ without decay correction.

The simulation results were validated by phantom measurements at a field strength of 3 Tesla (Chapters 6 & 7). These measurements indicate that poor gradient fidelity significantly worsens the accuracy of the rotation estimation of the navigator. Thus, the k–space trajectory of the Lissajous navigator was measured and a novel k–space correction scheme was developed (Chapter 6). The developed correction scheme reduced the mean deviation of the desired navigator radius by one order of magnitude from 2.0% to 0.2%. Finally, a comparison of the Lissajous and spherical navigator was performed with measured phantom data (Chapter 7). The investigation showed an increased accuracy of 38% for the Lissajous navigator (0.3°) over the spherical navigator (0.5°). Both simulations and measured data qualitatively showed the same structure. The rotation estimates for the Lissajous navigator exhibit the same characteristic shapes.

Thus, in conclusion, the Lissajous navigator delivers higher accuracy of rotation estimation and a higher degree of isotropy than the spherical navigator with no evident drawbacks.

8.2 Prospects

The present work revealed that the Lissajous navigator is capable of tracking motion with high accuracy while staying within the hardware limits. The next developmental step should focus on the implementation of real–time motion estimation and field–of–view adjustments for an active motion correction for MRI. To achieve this rotation estimates with sufficient accuracy have to be calculated in real–time. The task will thus be to bring in line the processing time of the rotation estimation with the required accuracy of the navigator and the repetition time of the navigator in the sequence.

The developed navigator could also be applied to simultaneous MR–PET imaging. Here, the motion data derived by utilising Lissajous navigators will be utilised to correct PET data for motion.

Finally, as the extent of translational motion that is detectable is limited by the k–space radius of the utilised navigator, translation measurements are effectively limited to a range of approximately $\pm 6mm$. To enable larger translational motion estimates, as might be required for uncooperative subjects, one future improvement could target the integration of line navigators for translational motion estimation.

External tracking systems always have the disadvantage of disturbing the examination process in some way. Optical mouthpieces have to be fitted first and might simply be unpractical for some patient groups. Markers attached to the forehead have to be applied and can move independently of the brain due to skin movement. This complicates their use in a clinical environment. Often no more than 15 minutes are available for a clinical examination, not leaving much time for the application of the external tracking system during patient preparation. Also the additional hardware has to be maintained. A motion correction approach based on the Lissajous navigator shares none of these disadvantages with the external tracking systems. No additional hardware is required, no special patient preparation is necessary. The procedure can be run identical to any non–motion corrected examination. The only drawback is a moderate, sequence dependent increase in scantime. Additionally, installed systems can be enabled to perform motion correction with a simple software upgrade when the Lissajous navigator is used. For external tracking systems new hardware has to be installed on each scanner.

The current trend in MRI is to move to high and ultra–high fields to take advantage of the increased signal at higher fields. Here the problems of motion becomes even more apparent. Smaller voxel sizes and larger absolute frequency and phase shifts intensify the image artefacts. Thus, for high field motion correction becomes increasingly important, while higher magnetic fields and the longer bore lengths in high field systems increase the engineering obstacles for external tracking systems. Navigator approaches also face new challenges at high fields. Efficient strategies for counteracting the shortened T_2 relaxation time have to be developed. However, once these have been mastered, they will enable motion–corrected magnetic resonance imaging at ultra–high fields with high patient compliance.

INDEX

B_1 field, 12
T_2^* Decay, 15
T_1 Decay, 13
T_2 Decay, 14
k–space, 35, 37
k-space
  rotation, 39
  translation, 39

Bloch equation, 13, 14, 64

chemical shift, 69
cloverleaf navigator, 44
coil
  gradient, 30
  radio frequency, 28, 32

data processing
  rotation estimation, 53
decay correction, 56, 59

echo time, 23
eddy current, 32, 91, 96

field inhomogeneities, 15
FLASH sequence, 23, 46, 109
Fourier shift theorem, 39
Fourier transform, 36
  continuous, 36
  discrete, 36
  inverse, 36
free induction decay, 9, 15, 17
frequency encoding, 17, 19

gradient, 17
  amplitude non–linearity, 91
  delay, 91, 96, 100, 101
  frequency encoding, 19
  pre–emphasis, 32
  readout, 19
  slice selection, 22

gradient amplifier, 30
gradient coil, 30, 32
gradient echo, 22
gradient field, 17, 30
gridding, 55
gyromagnetic ratio, 10, 37

interpolation, 55, 96, 125
    linear, 57

Jemris, 64

Larmor equation, 10, 18, 20
Larmor frequency, 12, 18
Lissajous figure, 47
Lissajous navigator
    gradients, 49
    trajectory, 49

magnetisation
    equilibrium state, 14
    net, 10, 14, 28
Maxwell pair, 30
MP–RAGE, 25

navigator
    cloverleaf, 42, 44
    Lissajous, 46
    orbital, 42
    pencil beam, 40
    reference, 53
    spherical, 42
nerve stimulation, 33, 34
net magnetisation, 10
noise, 73

orbital navigator, 42

pencil beam navigator, 40
phase coherence, 15, 25
phase encoding, 17, 21
Planck's constant, 10
precession, 10

radio frequency coil, 32
reference navigator, 53
relaxation, 13, 69, 75, 126
    T_2^*, 15, 55
    T_1, 13, 22
    T_2, 14, 22
    artefacts, 80
    longitudinal, 13, 14
RF coil, 32
RF field, 11
rotating frame, 12, 64
rotation estimation, 53, 56, 66, 115, 116, 129

sequence

  - gradient echo, 22
  - MP–RAGE, 25
  - spin echo, 25
- sequence diagram, 23
- signal equation, 15, 64
- signal–to–noise ratio, 73, 124
- slew rate, 32, 44, 50, 65
  - limit, 32
- slice selection, 17, 18
- spatial encoding, 17
- spatial frequency, 35
- specific absorption rate, 33
- spherical distance, 55
- spherical navigator, 42
- spin echo, 25
- spin excitation, 11
- spin polarisation, 9
- spin population difference, 10
- spin–lattice interaction, 14
- spin–spin interaction, 13, 14
- spoiling, 23
- static field magnet, 30
- susceptibility, 69

- trajectory correction, 104, 116, 130
- trajectory measurement, 91, 104
- translation estimation, 60, 65, 66, 89

- virtual rotation, 111

REFERENCES

[1] E. B. Welch, A. Manduca, R. C. Grimm, H. A. Ward, and C. R. Jack, "Spherical navigator echoes for full 3d rigid body motion measurement in mri.," *Magn Reson Med*, vol. 47, pp. 32–41, Jan 2002. (Cited on pages xv, xvii, 5, 6, 42, 43, 44, 45, 54, 60, 64, 65, 116, 124 and 129.)

[2] T. M. Cover and J. A. Thomas, *Elements of Information Theory*. 605 Third Ave, New York, Ny 10158-0012: John Wiley & Sons Inc, second edition ed., July 2006. (Cited on page 4.)

[3] K. J. Friston, S. Williams, R. Howard, R. S. Frackowiak, and R. Turner, "Movement-related effects in fmri time-series.," *Magn Reson Med*, vol. 35, pp. 346–355, Mar 1996. (Cited on pages 4 and 5.)

[4] R. P. Woods, S. R. Cherry, and J. C. Mazziotta, "Rapid automated algorithm for aligning and reslicing pet images.," *J Comput Assist Tomogr*, vol. 16, no. 4, pp. 620–633, 1992. (Cited on page 4.)

[5] R. P. Woods, S. T. Grafton, C. J. Holmes, S. R. Cherry, and J. C. Mazziotta, "Automated image registration: I. general methods

and intrasubject, intramodality validation.," *J Comput Assist Tomogr*, vol. 22, no. 1, pp. 139–152, 1998. (Cited on page 4.)

[6] M. Jenkinson, P. Bannister, M. Brady, and S. Smith, "Improved optimization for the robust and accurate linear registration and motion correction of brain images.," *Neuroimage*, vol. 17, pp. 825–841, Oct 2002. (Cited on page 4.)

[7] J. G. Pipe, "Motion correction with propeller mri: application to head motion and free-breathing cardiac imaging.," *Magn Reson Med*, vol. 42, pp. 963–969, Nov 1999. (Cited on page 4.)

[8] K. P. Forbes, J. G. Pipe, C. R. Bird, and J. E. Heiserman, "Propeller mri: clinical testing of a novel technique for quantification and compensation of head motion.," *J Magn Reson Imaging*, vol. 14, pp. 215–222, Sep 2001. (Cited on page 4.)

[9] S. Thesen, O. Heid, E. Mueller, and L. R. Schad, "Prospective acquisition correction for head motion with image-based tracking for real-time fmri.," *Magn Reson Med*, vol. 44, pp. 457–465, Sep 2000. (Cited on page 4.)

[10] O. Speck, J. Hennig, and M. Zaitsev, "Prospective real-time slice-by-slice motion correction for fmri in freely moving subjects.," *MAGMA*, vol. 19, pp. 55–61, May 2006. (Cited on page 5.)

[11] C. Dold, M. Zaitsev, O. Speck, E. A. Firle, J. Hennig, and G. Sakas, "Advantages and limitations of prospective head motion compensation for mri using an optical motion tracking de-

vice.," *Acad Radiol*, vol. 13, pp. 1093–1103, Sep 2006. (Cited on page 5.)

[12] M. Zaitsev, C. Dold, G. Sakas, J. Hennig, and O. Speck, "Magnetic resonance imaging of freely moving objects: prospective real-time motion correction using an external optical motion tracking system.," *Neuroimage*, vol. 31, pp. 1038–1050, Jul 2006. (Cited on page 5.)

[13] A. J. W. van der Kouwe, T. Benner, and A. M. Dale, "Real-time rigid body motion correction and shimming using cloverleaf navigators.," *Magn Reson Med*, vol. 56, pp. 1019–1032, Nov 2006. (Cited on pages 5, 42, 44 and 46.)

[14] J. Maclaren, O. Speck, D. Stucht, P. Schulze, J. Hennig, and M. Zaitsev, "Navigator accuracy requirements for prospective motion correction.," *Magn Reson Med*, vol. 63, pp. 162–170, Jan 2010. (Cited on page 6.)

[15] L. G. Hanson, "Is quantum mechanics necessary for understanding magnetic resonance?," *Concept Magn. Reson. Part A*, vol. 32A, pp. 329–340, Sep 2008. (Cited on page 11.)

[16] J. Felder, *Design and Optimisation of RF Frontend Components for Unilateral and Mobile MR Tomographs Employing Efficient, Linear Power Amplifiers.* P.O. Box 101818, D-52018 Aachen: Shaker Verlag, 2004. (Cited on page 12.)

[17] F. Bloch, "Nuclear induction," *Phys. Rev.*, vol. 70, pp. 460–474, Oct 1946. (Cited on page 13.)

[18] E. M. Haacke, R. W. Brown, M. R. Thompson, and R. Venkatesan, *Magnetic Resonance Imaging Physical Prinicples and Sequence Design.* 605 Third Avenue, New York, NY 10158-0012, USA: John Wiley & Sons, Inc., 1999. (Cited on page 13.)

[19] SiemensMedical, *Magnete Spins und Resonanzen, Eine Einführung in die Grundlagen der Magnetresonanztomographie.* Erlangen: Siemens AG, 2003. (Cited on pages 18 and 38.)

[20] A. Haase, J. Frahm, D. Matthaei, W. Hanicke, and K. Merboldt, "Flash imaging - rapid nmr imaging using low flip-angle pulses," *J Magn Res*, vol. 67, pp. 258–266, Apr 1986. (Cited on pages 22, 23 and 46.)

[21] M. A. Bernstein, K. F. King, and X. J. Zhou, *Handbook of MRI Pulse Sequences.* 200 Wheeler Road, 6th Floor, Burlington, MA 01803, USA: Elsevier Academic Press, illustrated edition (21. september 2004) ed., Sept 2004. (Cited on page 23.)

[22] E. L. Hahn, "Spin echoes," *Phys. Rev.*, vol. 80, pp. 580–594, Nov 1950. (Cited on page 25.)

[23] J. P. Mugler and J. R. Brookeman, "Three-dimensional magnetization-prepared rapid gradient-echo imaging (3d mp rage).," *Magn Reson Med*, vol. 15, pp. 152–157, Jul 1990. (Cited on page 25.)

[24] R. Deichmann, C. D. Good, O. Josephs, J. Ashburner, and R. Turner, "Optimization of 3-d mp-rage sequences for struc-

tural brain imaging.," *Neuroimage*, vol. 12, pp. 112–127, Jul 2000. (Cited on page 25.)

[25] J. P. Hornak, "The basics of mri." `http://www.cis.rit.edu/htbooks/mri/`, 2011. (Cited on pages 28 and 29.)

[26] R. Turner, "A target field approach to optimal coil design," *Journal of Physics D-Applied Physics*, vol. 19, pp. L147–L151, Aug 14 1986. (Cited on page 30.)

[27] S. S. Hidalgo-Tobon, "Theory of gradient coil design methods for magnetic resonance imaging," *Concept Magnetic Res A*, vol. 36A, pp. 223–242, Jul 2010. (Cited on page 30.)

[28] IEC, "Medical electrical equipment - part 2-33: Particular requirements for the basic safety and essential performance of magnetic resonance equipment for medical diagnosis," 2010. (Cited on page 34.)

[29] T. F. Budinger, "Nuclear magnetic resonance (nmr) in vivo studies: known thresholds for health effects.," *J Comput Assist Tomogr*, vol. 5, pp. 800–811, Dec 1981. (Cited on page 34.)

[30] J. Abart, K. Eberhardt, H. Fischer, W. Huk, E. Richter, F. Schmitt, T. Storch, B. Tomandl, and E. Zeitler, "Peripheral nerve stimulation by time-varying magnetic fields.," *J Comput Assist Tomogr*, vol. 21, no. 4, pp. 532–538, 1997. (Cited on page 34.)

[31] S. Ljunggren, "A simple graphical representation of fourier-

based imaging methods," *Journal of Magnetic Resonance*, vol. 54, no. 2, pp. 338–343, 1983. (Cited on page 35.)

[32] D. B. Twieg, "The k-trajectory formulation of the nmr imaging process with applications in analysis and synthesis of imaging methods.," *Med Phys*, vol. 10, no. 5, pp. 610–621, 1983. (Cited on page 35.)

[33] R. N. Bracewell, *The Fourier Transform and its Applications.* Singapore: McGrap Hill, Inc., second edition, revised ed., 1986. (Cited on pages 36 and 39.)

[34] D. G. Nishimura, *Principles of magnetic resonance imaging.* Stanford Univ., 1996. (Cited on page 37.)

[35] J. Cooley and J. Tukey, "An algorithm for machine calculation of complex fourier series," *Math Comput*, vol. 19, no. 90, pp. 297–301, 1965. (Cited on page 37.)

[36] M. Frigo and S. G. Johnson, "FFTW: an adaptive software architecture for the FFT," in *Proc. 1998 IEEE International Conference on Acoustics, Speech and Signal Processing*, vol. 3, (100662 Los Vaqueros Circle, P.O. Box 3014, Los Alamitos, CA 90720-1264, USA), pp. 1381–1384, IEEE, May 12–15, 1998. (Cited on page 37.)

[37] M. Frigo and S. G. Johnson, "The design and implementation of FFTW3," *Proceedings of the IEEE*, vol. 93, pp. 216–231, Feb. 2005. Special issue on "Program Generation, Optimization, and Platform Adaptation". (Cited on page 37.)

[38] D. M. Higgins, "The what is k-space? tutorial." `http://revisemri.com/tutorials/what_is_k_space`, May 2010. (Cited on page 38.)

[39] D. L. Collins, A. P. Zijdenbos, V. Kollokian, J. G. Sled, N. J. Kabani, C. J. Holmes, and A. C. Evans, "Design and construction of a realistic digital brain phantom.," *IEEE Trans Med Imaging*, vol. 17, pp. 463–468, Jun 1998. (Cited on pages 39, 41 and 65.)

[40] R. L. Ehman and J. P. Felmlee, "Adaptive technique for high-definition mr imaging of moving structures.," *Radiology*, vol. 173, pp. 255–263, Oct 1989. (Cited on page 40.)

[41] C. J. Hardy and H. E. Cline, "Spatial localization in 2 dimensions using nmr designer pulses," *Journal of Magnetic Resonance*, vol. 82, pp. 647–654, May 1989. (Cited on page 40.)

[42] Z. W. Fu, Y. Wang, R. C. Grimm, P. J. Rossman, J. P. Felmlee, S. J. Riederer, and R. L. Ehman, "Orbital navigator echoes for motion measurements in magnetic resonance imaging.," *Magn Reson Med*, vol. 34, pp. 746–753, Nov 1995. (Cited on page 42.)

[43] R. Likes, "Moving gradient zeugmatography," July 1981. (Cited on page 47.)

[44] D. C. Noll, "Multishot rosette trajectories for spectrally selective mr imaging.," *IEEE Trans Med Imaging*, vol. 16, pp. 372–377, Aug 1997. (Cited on page 47.)

[45] H. Feng, H. Gu, D. Silbersweig, E. Stern, and Y. Yang, “Single-shot mr imaging using trapezoidal-gradient-based lissajous trajectories.,” *IEEE Trans Med Imaging*, vol. 22, pp. 925–932, Aug 2003. (Cited on page 47.)

[46] J. C. Lagarias, “Convergence properties of the nelder-mead simplex method in low dimensions,” *SIAM Journal on Optimization*, vol. 9, pp. 112–147, DEC 21 1998. (Cited on pages 53 and 54.)

[47] N. L. im DIN Deutsches Institut fuer Normung e.V., “Din9300 - luft- und raumfahrt; begriffe, größen und formelzeichen und flugmechanik; bewegung des luftfahrzeuges gegenüber der luft; iso 1151-1:1988 modifiziert.” Beuth Verlag GmbH, 1990. (Cited on page 53.)

[48] I. N. Bronstein, K. A. Semendjajew, G. Mussiol, and H. Muehlig, *Taschenbuch der Mathematik*. Thun und Frankfurt am Main, Germany: Verlag Harri Deutsch, 5. ueberarbeitete und erweiterte auflage ed., 2001. (Cited on page 55.)

[49] T. Stöcker, K. Vahedipour, and N. J. Shah, “Hpc simulation of magnetic resonance imaging,” *Advances in Parallel Computing*, vol. 15, no. 1, pp. 155–164, 2008. (Cited on page 64.)

[50] “http://www.jemris.org.” (Cited on page 64.)

[51] T. Stöcker, K. Vahedipour, D. Pflugfelder, and N. J. Shah, “High-performance computing mri simulations.,” *Magn Reson Med*, vol. 64, pp. 186–193, Jul 2010. (Cited on page 64.)

[52] J. P. Marques and R. Bowtell, “Application of a fourier-based method for rapid calculation of field inhomogeneity due to spatial variation of magnetic susceptibility,” *Concepts Magn Reson Part B*, vol. 25B, pp. 65–78, 2005. (Cited on page 64.)

[53] B. J. Nieman, J. Bishop, and R. M. Henkelman, “Gradient hysteresis in mri and nmr experiments.,” *J Magn Reson*, vol. 177, pp. 336–340, Dec 2005. (Cited on page 91.)

[54] G. F. Mason, T. Harshbarger, H. P. Hetherington, Y. Zhang, G. M. Pohost, and D. B. Twieg, “A method to measure arbitrary k-space trajectories for rapid mr imaging.,” *Magn Reson Med*, vol. 38, pp. 492–496, Sep 1997. (Cited on pages 91 and 92.)

[55] J. H. Duyn, Y. Yang, J. A. Frank, and J. W. van der Veen, “Simple correction method for k-space trajectory deviations in mri.,” *J Magn Reson*, vol. 132, pp. 150–153, May 1998. (Cited on pages 91 and 92.)

[56] D. J. Goodyear, M. Shea, S. D. Beyea, N. J. Shah, and B. J. Balcom, “Single point measurements of magnetic field gradient waveform.,” *J Magn Reson*, vol. 163, pp. 1–7, Jul 2003. (Cited on page 91.)

[57] C. Barmet, N. D. Zanche, B. J. Wilm, and K. P. Pruessmann, “A transmit/receive system for magnetic field monitoring of in vivo mri.,” *Magn Reson Med*, vol. 62, pp. 269–276, Jul 2009. (Cited on page 95.)

[58] S. Butterworth, “On the theory of filter amplifiers,” *Experimenal wireless & the wireless engineer*, vol. 7, pp. 536–541, 1930. (Cited on page 98.)

[59] H. Herzog, L. Tellmann, S. Qaim, S. Spellerberg, A. Schmid, and H. Coenen, “Pet quantitation and imaging of the non-pure positronemitting iodine isotope i-124,” *Applied Radiation and Isotopes*, vol. 56, pp. 673–679, May 2002. (Cited on page 111.)